HVOF THERMAL SPRAY VELOCITY, TEMPERATURE, AND STAINLESS STEEL COATING PROPERTIES

Gary S. Settles and Sarah R. Bekofske

Gas Dynamics Laboratory
Mechanical Engineering Dept.
Penn State University
University Park, PA 16802 USA

ABSTRACT

Corrosion-protection coatings of 316 Stainless Steel have been sprayed by the High-Velocity Oxy-Fuel (HVOF) spray process. Control of the average particle temperature and velocity over ranges of 1600-2300 K and 250-450 m/s was demonstrated. By thus changing the in-flight particle parameters, a range of different coating properties was generated. However, not all of these were desirable coatings, the highest particle temperatures producing a high-melted-phase coating with a high oxide content. In contrast, intermediate particle velocities and temperatures produced excellent dense coatings with plastic particle deformation and very low oxide content. Surprisingly, however, coatings with high particle velocity and low particle temperature reversed this trend, producing undesirable coatings which bore a high oxide content. Reasons for this appear to include impact heating and particle bursting, but further research is called for.

INTRODUCTION

Thermal spray technology has recently become important to the materials, manufacturing, and maintenance/repair industries. One such technique is the High-Velocity Oxy-Fuel (HVOF) thermal spray torch, which burns a fuel stream with oxygen at sufficiently high pressure to produce a supersonic jet of hot combustion gases. Particles introduced into this stream are both heated and accelerated to high speeds, whereupon their impact with a solid surface produces,

under proper circumstances, a high-quality coating. Key HVOF applications include wear-resistant coatings, corrosion-resistant coatings, and thermal barrier coatings. Corrosion-resistant coatings such as Hastelloy, Inconel, and Stainless Steel are sprayed on shafts, surgical implants, machine elements, and reactor vessel walls for corrosion protection during manufacture and later for repair purposes. This application is clearly important for the energy-related industries.

The principal goal of the present research is to relate in-flight particle temperature T_p and velocity V_p to resulting coating characteristics by way of coating metallography, both to improve the scientific understanding of the coating process and to provide feedback to modify HVOF process parameters for improved coating quality. Of the wide array of possible coatings, we chose 316 Stainless Steel for its prevalence in corrosion-resistant coating applications and its susceptibility to oxidation. We then undertook to determine whether or not increased V_p and reduced T_p really do produce better coatings, as is widely believed in the industry [1].

EXPERIMENTAL EQUIPMENT AND METHODS

The HVOF equipment used here is a modified commercial TAFA JP-5000 system. The main modification is the replacement of the factory nozzle by a proper supersonic Laval nozzle having four different particle injection ports distributed along its length. Kerosene and Oxygen gas were burned at combustion pressures P_c ranging from 65 psi to 120 psi. Oxygen/Fuel equivalence ratios ϕ were maintained in the range 3.1-4.2.

All particle velocities and temperatures were measured at a standoff distance from the nozzle exit of 40 cm, in the normal position of a substrate while spraying, according to manufacturer specifications. V_p is controlled directly by the HVOF combustion chamber pressure P_c [2, 3]. T_p was controlled by varying the equivalence ratio ϕ in previous work [2], but is here controlled by the unique means of changing particle injection location along the length of the nozzle [3,4]. Since T_p also decreases with increasing P_c for a given particle injection location (apparently due to shorter particle residence time in the nozzle), not all T_p, V_p combinations within the performance envelope of the HVOF torch are achievable. Nonetheless, by this approach a range of different coating properties can be obtained.

316L Stainless Steel powder (TAFA #1236F) was used to produce representative corrosion-resistant coatings. This austenitic Stainless-Steel alloy is well-known for its corrosion protection, tensile strength, and fracture toughness. However, oxidation dramatically degrades 316 Stainless Steel (316SS) coatings, reducing ultimate tensile strength, causing embrittlement, and providing pathways for corrosion to reach the substrate and undermine the coating [5]. The gas-atomized powder used here has a fine dendritic microstructure due to rapid solidification. It has a mean particle size of 34 μm with a standard deviation of 9 μm. 316SS coatings were sprayed onto sandblasted aluminum substrate coupons traversed through the particle stream while the HVOF spray gun remained stationary.

A two-color optical pyrometer was used to measure the temperature of the 316SS spray particles non-intrusively in flight. Two-color pyrometry involves calculating the ratio of thermal radiances measured at two different wavelengths [6], here chosen as 800 and 900 nm for expected particle temperatures in the 1200-2000 K range. The resulting calibration of 316SS particle T_p vs. P_c is shown in Figure 1. An uncertainty of about ± 60 K is determined at T_p =

1700 K for the "average" particle, but the effective uncertainty in T_p for an arbitrary particle is greater than this due to the breadth of the particle size distribution. The design and setup details of our pyrometer are discussed elsewhere [3, 4, 7].

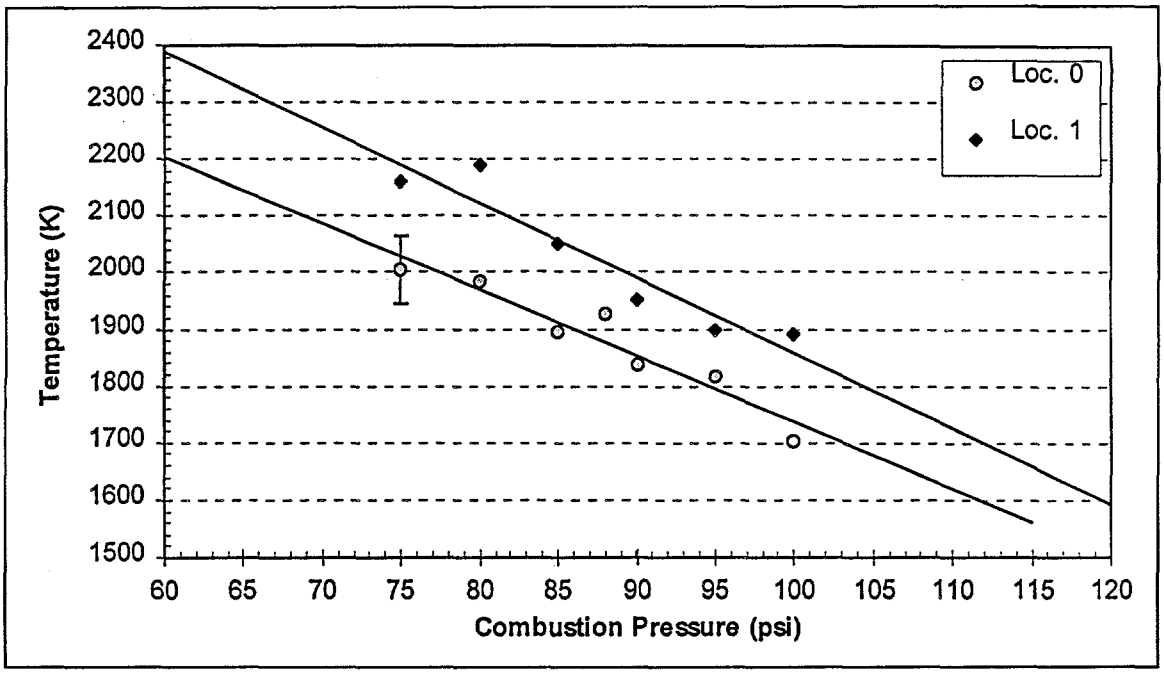

Figure 1 - Calibration of 316SS Particle Temperature T_p vs. P_c for 2 Nozzle Injection Locations

Particle trace velocimetry was used to measure V_p by optically imaging the distance traveled by a glowing particle over a known time interval. An electronic camera was used with a 15 μsec exposure time. Again, for brevity the details of the measurement are omitted here, since they are amply reported elsewhere [3, 4, 7].

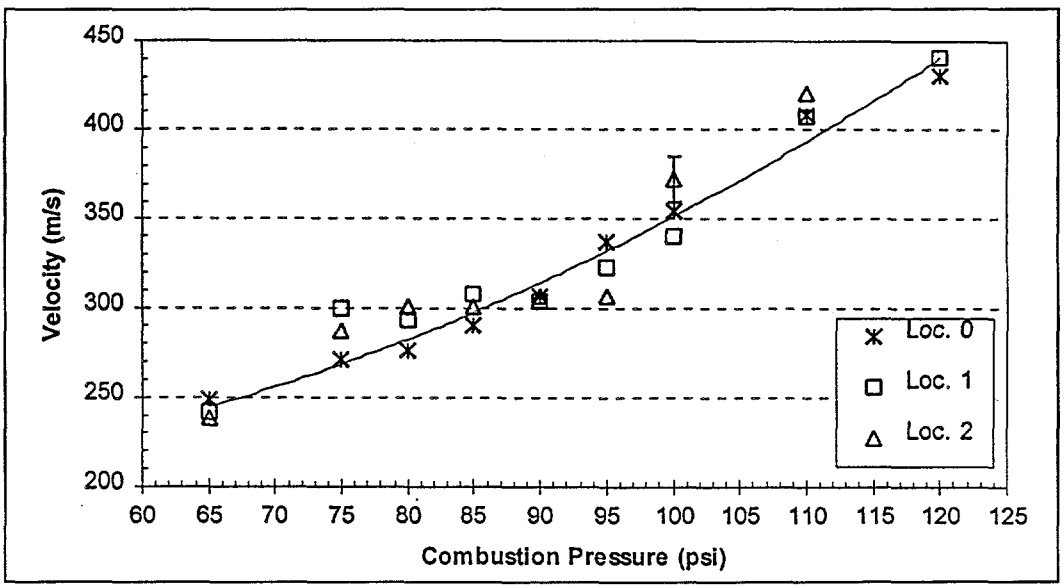

Figure 2 - Calibration of 316SS Particle Velocity V_p vs. P_c for 3 Nozzle Injection Locations

As shown in Figure 2, rising combustion chamber pressure P_c increases V_p due to the effect of increasing dynamic pressure on the drag force exerted upon the particle by the gas flow. Measurement errors can arise if the camera fails to register small particles or colder particles, thus prejudicing the measurement toward the larger and/or hotter particles. Also, the breadth of the particle size distribution dictates that an individual particle may vary ± 100 m/s or more from the V_p of the "average" particle. Also note that the present V_p range is noticeably less than that of Voggenreiter et al. [5] (500-620 m/s) or Swank et al.[2] (500-700 m/s). This is explainable, at least in part, by our shorter-than-standard HVOF nozzle and consequent shorter distance from particle injection to nozzle exit.

RESULTS AND DISCUSSION

The present test matrix of available thermal spray process parameters spans the ranges of $250 \leq Vp \leq 450$ m/s and $1600 \leq Tp \leq 2300$ K. Metallography was performed on coatings from most of the test points in this test matrix. Three typical results are shown in Figure 3 for the cases of coatings near the high-T_p, low-V_p end of the test matrix, at an intermediate temperature and velocity, and near the low-T_p, high-V_p end of the matrix. In all cases the magnification is 200X and an electrolytic oxalic acid etch was used.

The coating of Figure 3a (V_p = 275 m/s, T_p = 2200 K) shows a bright stainless steel phase interspersed with a marbled, gray-to-dark oxide phase. Coating oxidation comes as no surprise at such high T_p , well above T_{melt} (1648-1673 K). Thus coatings in this HVOF parameter range are undesirable due to embrittlement, poor corrosion resistance, Chromium depletion, and porosity.

However, the metallogram of Figure 3b (V_p = 300 m/s, T_p = 1900 K) is indicative of very high-quality coatings in the middle of the test matrix. "Doughy" particles have undergone plastic impact to form this compact, low-porosity coating. There is little evidence of gray oxide phase except for the thin, well-defined splat boundaries. Individual splats having undergone plastic deformation are clearly visible. Within these splats, the fine dendritic microstructure is a remnant of the rapid solidification which the alloy underwent during gas atomization [5]. By comparison, wrought 316SS has a large polygonal grain structure comparable in size to the present spray particles themselves. Voggenreiter et al [8] demonstrate, for Inconel HVOF coatings, that such low-melted-fraction coatings are far superior in strength to high-melted-fraction (high-oxide) coatings. Further, Voggenreiter et al. [5] claim that such coatings show little effect of V_p and no bursting of the sprayed particles with subsequent splatter. Their best Stainless Steel coatings, like ours shown in Figure 3b, have a porosity of only 0.1-0.2%.

The big surprise is Figure 3c (V_p = 450 m/s, T_p = 1500 K). With even lower particle temperatures than the case of Figure 3b, coatings at this end of the test matrix were expected to be the least oxidized and most compact of all. Instead, a pronounced degradation of coating quality is seen, with Stainless Steel particles interspersed with melted alloy phase and marbled, gray-to-dark oxide phase. This result directly contradicts the belief within the thermal spray industry [1] that low-T_p, high-V_p coatings are high-quality coatings. Nonetheless, since all coatings at that end of our test matrix showed characteristics similar to Figure 3c, there can be no doubt of it. It was immediately clear to us that this result needed further investigation in order to understand the discrepancy between results and expectations.

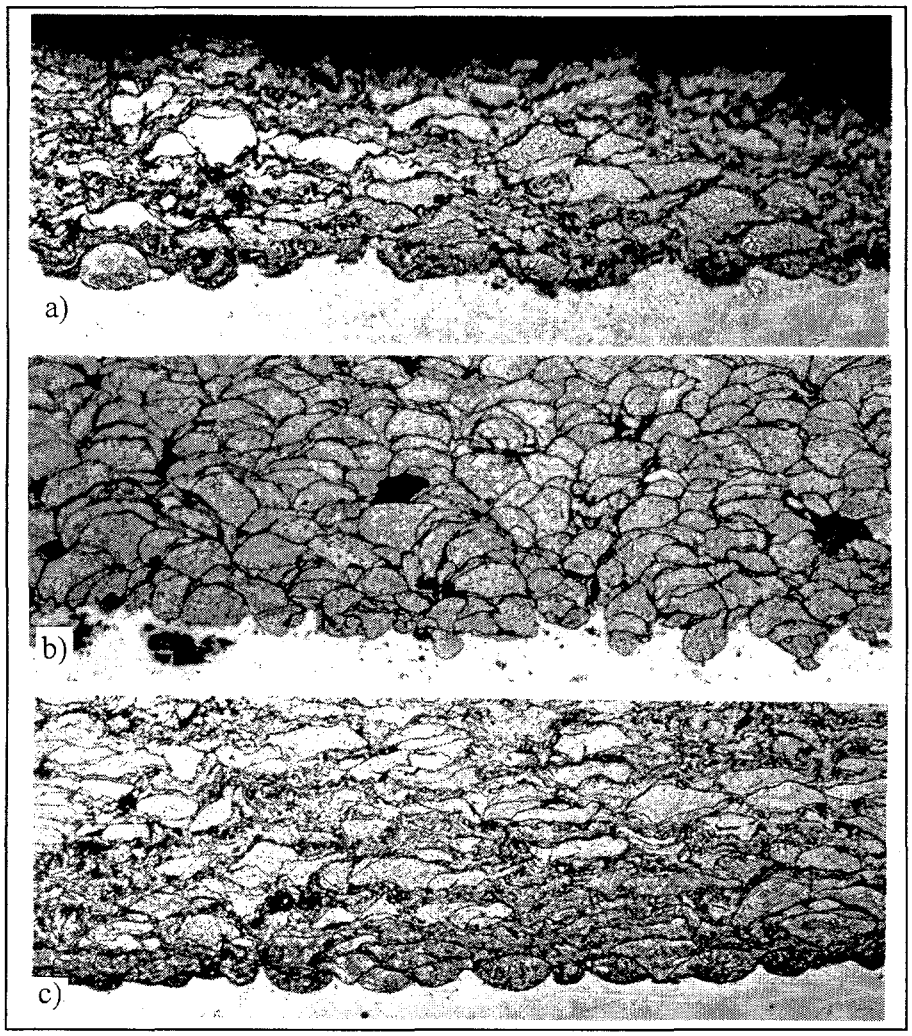

Figure 3 - Example 316SS Metallograms for a) High -T_p, low-V_p Conditions, b) Intermediate Conditions, and c) Low-T_p, High-V_p Conditions of the Present Test Matrix.

Accordingly, representative samples from the test matrix were evaluated for Oxygen content. The results show that coatings from the middle of the test matrix (at intermediate T_p, and V_p) are the least-oxidized coatings of all. Even these contain significantly more Oxygen than the original powder (0.02%), principally in an oxide shell which forms around the particles during flight. Otherwise, coating oxide levels are in the range of 0.5-1.0%. (Note that a fractional percentage of oxides by weight corresponds to a much larger volume percentage.)

Thus the surprising result that serious coating oxidation occurs at high V_p and low T_p is confirmed. This is a novel discovery, not having been noted in previous literature.

We next examined coating oxidation levels as a function of the percentage volume of the melted phase in the metallograms (obtained via image analysis). An essentially-proportional relationship was found, meaning that significant melting of metal particles at *either* end of the present test matrix is directly related to coating oxidation. This is shown in Figure 4, a plot of the percentage volume of the melted phase vs. T_p for most points of the present test matrix. T_{melt} for 316L Stainless Steel is also shown on the T_p axis for comparison.

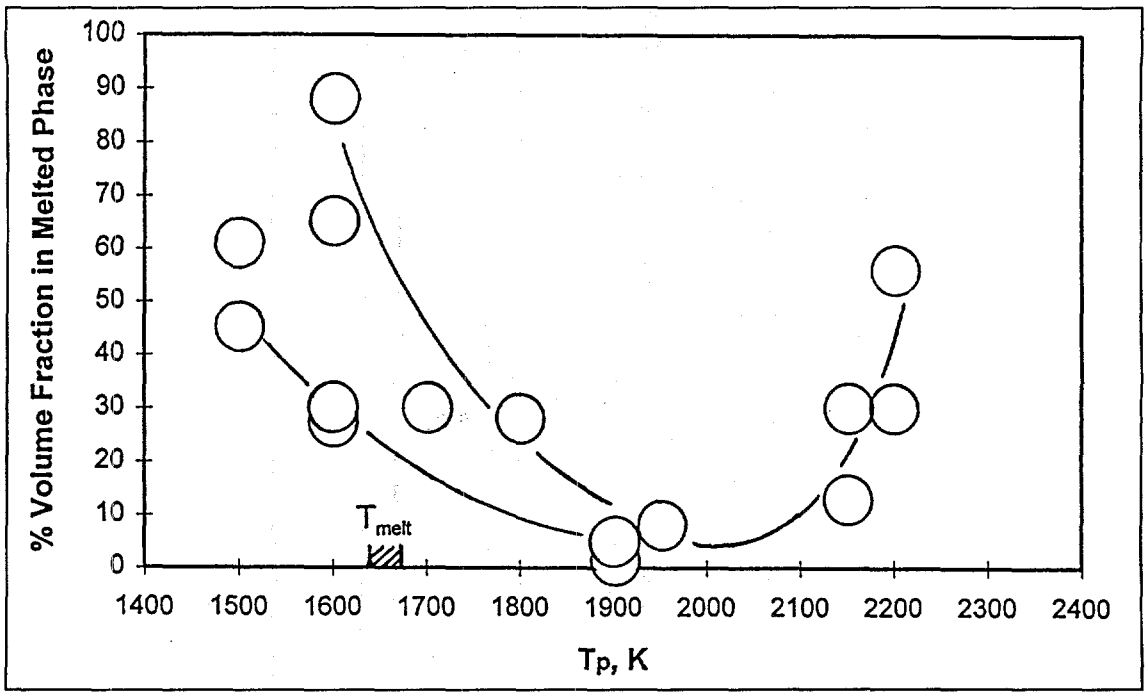

Figure 4 - Percent Volume Fraction of Melted Phase Plotted vs. T_p

The challenge to understand Figures 3 and 4 comes down to two questions: 1) Why is sprayed-particle melting and oxidation so prevalent at the high V_p and low T_p end of the test matrix?, and 2) Why do the "best" low-oxide, low-melted phase coatings occur some 200-300 K above T_{melt} for stainless steel?

One possible answer to the first question involves substrate temperature. No substrate cooling was employed in the present tests, and it is known that the high P_c values necessary to accelerate particles to high V_p tend to raise $T_{substrate}$ when the standoff distance is held fixed. Swank et al. [2] claim coating oxidation is a function of $T_{substrate}$, not either entrained Oxygen or excess combustion Oxygen, but Voggenreiter et al. [5] appear to disagree with this. Present measurements reveal $T_{substrate}$ to be in the range of 500-600 K, which seems much too cold to promote much oxidation. However, despite such low values of $T_{substrate}$, special tests did show at least some influence of $T_{substrate}$ on coating oxide levels when other parameters were held constant. This was not enough, however, to fully explain the curious observations in Figures 3 and 4.

Let us now address the issue of impact heating. The particle kinetic energy, $\frac{1}{2}m_pV_p^2$, is assumed to be converted into thermal energy $m_pc\Delta T_p$ upon impact, where m_p is particle mass and c is the specific heat of the Stainless Steel. This yields $60 \leq \Delta T_p \leq 200$ K for the present test conditions. However, this result is for the "average" particle, and it was noted earlier that the breadth of the particle size distribution dictates that an individual particle may vary ± 100 m/s or more from the V_p of the "average" particle. Taking this fact into account makes ΔT_p due to impact heating feasible up to 300 K or more for the fastest particles. Thus impact heating must be considered as a possible contributor in explaining the observed behavior in Figures 3 and 4.

Another relevant issue is that of high-V_p particle bursting or splatter. Voggenreiter et al. [5] surmised that this phenomenon was responsible for oxidation in some of their coatings, and concluded that the main oxidation occurred in particle interactions with the substrate, not in

flight. Briefly, if V_p is sufficient to burst the oxide shell of the particle upon impact, then (depending on a sufficient level of $T_p + \Delta T_p$), the metallic core of the particle can liquefy and splatter, leading to a large exposed surface area for oxidation and a high volume fraction of the melted phase. This hypothetical mechanism is promoted by particle-shell oxides with T_{melt} higher than that of the stainless steel core, such as Cr_2O_3 (T_{melt} = 2700 K). For sufficiently-high T_p, such particles could have solid surfaces and molten cores in flight. Particle shell bursting then explains the splatter and oxidation which characterizes coating cross-sections at the high-T_p end of out test matrix [3].

Alternatively, at the high-V_p, low-T_p end of our test matrix, particles have spent a minimum residence time in the hot HVOF jet and may be heated non-uniformly, presenting an apparent temperature T_p to the optical pyrometer which is more characteristic of the oxide shell than the cooler particle core. When these particles impact at high V_p, the oxide shell bursts due to the impact energy and $T_p + \Delta T_p$ rapidly liquefies the base metal, potentially causing the splatter and oxidation which characterize coating cross-sections at the low-T_p end of the test matrix.

Why, then, are the "best" coatings found in a T_p range some 200-300 K above T_{melt} for Stainless Steel? Impact heating, an oxide shell hotter than the particle core, and an illusory shift due to the "average particle" concept are all candidates for this explanation. It will take further research to evaluate these issues and discover with certainty the explanation behind the important but somewhat puzzling observations reported here.

OBSERVATIONS AND CONCLUSIONS

For 316 Stainless Steel HVOF-sprayed coatings, control of the average particle temperature and velocity over ranges of 1600-2300 K and 250-450 m/s has been demonstrated. By varying the in-flight particle state via combustion-chamber pressure and particle injection location, a range of different coating properties can be generated. However, not all of these are desirable coatings. Metallography reveals that coatings at the highest particle temperatures are undesirable due to a high melted phase with a high oxide content. Intermediate in-flight particle velocity and temperature (T_p ~1900-2000 K, V_p ~ 275-325 m/s) produce excellent dense coatings with plastic deformation of particles and very low oxide content. In such coatings, the properties of the feedstock powder are directly reflected in the coating itself. These "best" coatings occur for apparent particle temperatures some 200-300 K above the melting temperature of Stainless Steel, possibly due to impact heating, non-uniform in-flight particle heating, a refractory particle oxide shell, and the concept of "average" particle temperature. Surprisingly, coatings with high particle velocity and low particle temperature produce undesirable coatings containing a high melted phase with a high oxide content. Reasons for this appear to include impact heating, impact bursting of the particle oxide shell with subsequent splatter, and possibly the effect of elevated substrate temperature. Further research is called for to clarify these issues. An important lesson learned here for the thermal spray community (at least for the present case of 316 Stainless Steel HVOF coatings) is that coating properties and coating quality are strong functions of particle temperature and pressure which belie previous oversimplified explanations. Simply increasing the particle velocity and reducing the temperature do *not* necessarily lead to improved coating quality. Until a better understanding is forthcoming, the best coatings can be

had only with careful attention to these issues, and with feedback from coating metallography. In particular, the connection between HVOF coatings and those produced by cold gas-dynamic deposition at still lower T_p and higher V_p [9] is not understood, and present work indicates it is likely to be more complex than was earlier imagined.

ACKNOWLEDGEMENT

This work was performed under the auspices of the U. S. Department of Energy, Grant DE-FG02-92ER14302. The assistance of J. D. Miller and L. J. Dodson of the Gas Dynamics Laboratory is gratefully acknowledged.

REFERENCES

1. G. IRONS, "Higher Velocity Thermal Spray Processes Produce Better Aircraft Engine Coatings," SAE Paper 920947, 28th Ann. Aerosp./Airline Plating & Metal Fin. Forum, 1992.

2. W.D. SWANK, J. R. FINCKE, D. C. HAGGARD, G. IRONS, and R. BULLOCK, "HVOF Particle Flow Field Characteristics," *Proc. 7th Natl. Ther. Spray Conf.*, Boston, June 1994.

3. C.M. HACKETT and G.S. SETTLES, "Independent Control of HVOF Particle Velocity and Temperature," in *Thermal Spray: Practical Solutions for Engineering Problems*, ed. C.C. Berndt, ASM International, Materials Park, OH, pp. 665-673, 1996.

4. C.M. HACKETT, "The Gas Dynamics of High-Velocity Oxy-Fuel Thermal Sprays," Ph.D. Thesis, Dept. of Mechanical Engineering, Penn State University, 1996.

5. H. VOGGENREITER, H. HUBER, S. BEYER, and H-J. SPIES, "Influence of Particle Velocity and Molten Phase on the Chemical and Mechanical Properties of HVOF-Sprayed Structural Coatings of Alloy 316L," in *Advances in Thermal Spray Science and Technology*, ed. C.C. Berndt and S. Sampath, ASM International, Materials Park, OH, pp. 303-308, 1995.

6. J.R. FINCKE, C.L. JEFFREY and S.B. ENGLERT, "In-Flight Measurement of Particle Size and Temperature," *Journal of Physics E: Scientific Instruments,* Vol. 21, pp. 367-370, 1988.

7. S.R. BEKOFSKE, "Control of HVOF Thermal Spray Particle Temperature and Velocity," Master of Science Paper in Mechanical Engineering, Penn State University, 1997.

8. H. VOGGENREITER, H. HUBER, H-J. SPIES, and H. BAUM, "HVOF-Sprayed Alloy IN718 - The Influence of Process Parameters on the Microstructure and Mechanical Properties," in *Thermal Spray: A United Forum for Scientific and Technological Advances*, ed. C.C. Berndt, ASM International, Materials Park, OH, pp. 895-900, 1997.

9. A.P. ALKHIMOV, V. F. KOSAREV, and A. N. PAPYRIN, "A Method of 'Cold' Gas-Dynamic Deposition," *Soviet Physics Doklady*, Vol. 35, No. 12, pp. 1047-1049, 1990.

Dispersion-Managed Solitons: A New Paradigm For High-Data Rate Communications

C. R. Menyuk and G. M. Carter

Department of Electrical Engineering, University of Maryland
Baltimore, MD 21228-5398

ABSTRACT

In the last two years a remarkable convergence of view has occurred between the community that advocated the use of non-return-to-zero (NRZ) signals and the community that advocated the use of solitons. It is now universally thought that formats that are intermediate to these two classical approaches will ultimately be adopted for high-data-rate communications. Among these intermediate formats are dispersion-managed solitons which share with NRZ signals the property that they propagate in dispersion maps and undergo large periodic oscillations and share with solitons the property that they are periodically stationary and have a return-to-zero shape. We have shown that these solitons are less susceptible to mutual interactions, undergo less timing jitter due to spontaneous emission noise, and are less disturbed by channel interactions in a wavelength division multiplexed system than are standard solitons. We have achieved a record-breaking propagation of 24,500 km in an uncontrolled channel, and we have demonstrated that it is possible to study both solitons and NRZ in the same recirculating loop.

1. INTRODUCTION

Historically, there were two formats that were considered for use in high-data-rate, long-distance optical fiber communication systems. The first is non-return-to-zero (NRZ) in which one simply spreads the energy from the transmitter, which is just a modulated laser diode, over the entire bit window. At the same time, one uses a dispersion map—alternating sections of positive and negative dispersion with an average that is nearly zero—to greatly reduce the distortion due to optical fiber nonlinearity. There is still a

significant residual distortion, but, because the average dispersion is nearly zero, the energy tends to stay in the bit window that it started in initially.[1] The second format is solitons. In this case, the energy is concentrated in the middle of the bit window so that this signal is necessarily a return-to-zero (RZ) signal. One then uses dispersion to compensate for the nonlinear distortion.[2] However, there is a price to pay for using dispersion to compensate for the nonlinearity. Any amplified spontaneous emission noise that leads to a frequency shift of the soliton also changes its velocity so that the soliton can drift out of its bit window. This effect, often referred to as the Gordon-Haus timing jitter, has a devastating effect on the bit error rate, and, as a consequence, soliton systems have never been used in practice. In principle, one can avoid the negative consequences of timing jitter by using soliton control—either sliding filters or some sort of active modulation.[2] However, these control systems are difficult to implement in systems.

In the last three years intermediate formats have evolved that appear to combine the advantages of both of these approaches and eliminate most of their disadvantages. On the one hand, by introducing dispersion management to soliton systems, we and other groups have discovered that it is possible to greatly reduce the timing jitter due to spontaneous emission noise while maintaining a good signal-to-noise ratio,[3] that the mutual interaction of solitons is reduced so that users may space them closer together,[4] and wavelength division multiplexing performs as well or better than is the case for standard solitons.[5] On the other hand, other workers have found that by using RZ signals in systems that were originally designed to carry NRZ signals it is possible to significantly enhance the system performance.[6]

In Sec. 2 of this article, we will review our own work on dispersion managed solitons and review their advantages. In Sec. 3 of this article, we will discuss our work comparing RZ and NRZ signals in the same system and our new, record-breaking propagation experiments. Section 4 contains the conclusions.

2. DISPERSION MANAGED SOLITONS

Smith, *et al.*[7] pointed out at any early stage of the investigations into dispersion managed solitons that for a given average dispersion, the energy in a single soliton is larger than would be anticipated from the theory of classical solitons by an amount referred to as the *enhancement factor*. In our own studies, we also found this enhancement factor,[4] as shown in Fig. 1, when the strength of the dispersion management increases. This strength is parametrized by a parameter $\gamma = 2\left[(\beta_1-\bar{\beta})L_1-(\beta_2-\bar{\beta})L_2\right]/\tau_0^2$, where β_1 is the dispersion in the first leg of the dispersion map of length L_1, β_2 is the dispersion in the second leg of the dispersion map of length L_2, $\bar{\beta}$ is the average dispersion, and τ_0 is the full width at half maximum. In the case shown in Fig. 1, we set $L_1 = L_2 = L_{\text{map}}/2$, where L_{map} is the total length of the disersion map, although we also verified that the results are insensitive to the choice of the map; they depend only on γ. Effectively, γ gives the ratio of the map length to the local dispersive scale length. When it is one or greater, then the pulse shape will change significantly in one leg of the map. In addition, we found an increase in the stretching factor, the ratio of the maximum to the minimum temporal full width at half maximum during the evolution in one period of the dispersion map. Furthermore, we found an increase in the time-bandwidth product. This increase was accompanied by

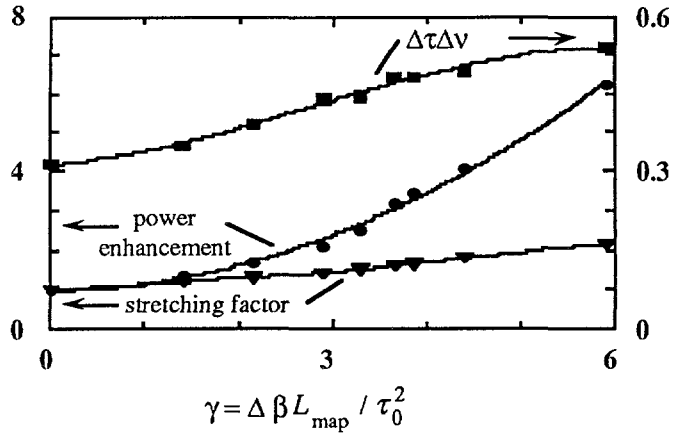

FIGURE 1. Variation of the enhancement factor, the stretching factor, and the time-bandwidth product $\Delta\tau\Delta\nu$ as a function of γ.

a change in the pulse shape at the point of maximum compression. When $\gamma \ll 1$, the shape is a hyperbolic-secant—the classical soliton chape. When $\gamma \simeq 3$, the shape is more Gaussian. Finally, when $\gamma \gtrsim 6$, the shape becomes a flattop.

The increase in the enhancement factor is accompanied by a reduction in the timing jitter as shown in Fig. 2. This result was obtained both theoretically and experimentally and was one of our earliest successful comparisons of the two in our system.[3] From these results, we were able to infer that our filters were too strong. As a consequence we replaced our 1.3 nm bandwidth filters with 2.8 nm bandwidth filters which allowed us to obtain the record-breaking results described in the next section. Additionally, we noticed a discrepancy in our simulations between the predictions of the enhancement factor for the reduction in the timing jitter and what was actually observed in some cases. This result led us to a linearization approach for determining the noise contributions that is both more efficient and more accurate than standard Monte Carlo simulations and may some day replace them.[8]

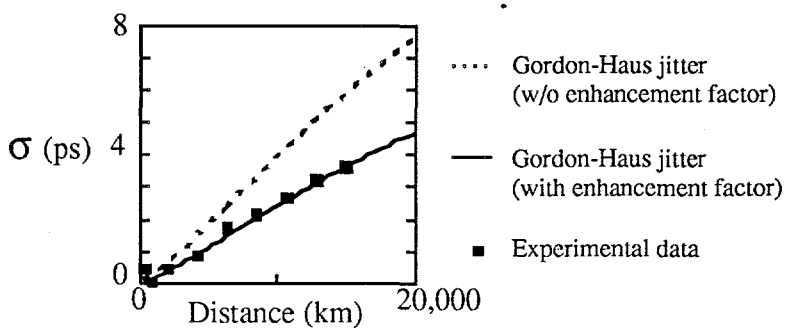

FIGURE 2. Variation of the timing jitter as a function of distance. Comparison of theory and experiment.

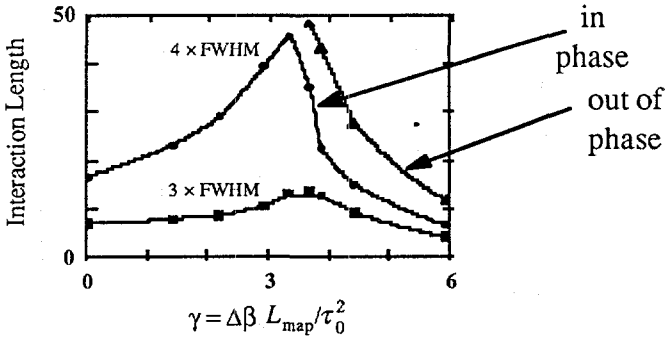

FIGURE 3. Variation of the interaction length as a function of γ.

The increase in the enhancement factor is at first accompanied by a decrease in the strength of the mutual interaction, which in turn leads to an increase in the interaction length as shown in Fig. 3.[4] Thus, the use of dispersion management allows the user to either space the 1-bits closer or to obtain a longer propagation length. However, this result only holds up to $\gamma \simeq 3$. Beyond that point, the interaction length decreases and at $\gamma \simeq 6$ becomes worse than for a standard soliton. This effect is due to a combination of the increased stretching shown in Fig. 1 so that the tails of the solitons interact more and the increased tails even at the point of maximum compression. This effect sets an optimal value for γ which roughly equals 3. An interesting effect that is also observed in Fig. 3 is that the interaction length becomes independent of the phase relation between neighboring solitons when $\gamma \gtrsim 3$. This effect occurs because the large dispersion management destroys the phase relationship between the neighboring solitons. By contrast, standard solitons of opposite signs always repel each other so that the interaction length is infinite. Thus, the optimum γ-value corresponds to the point at which the effects of the dispersion management become equal to the effects of the nonlinearity.

Finally, in Fig. 4, we show a comparison of the timing jitter due to the mutual interaction for an eight channel WDM system with three different dispersion maps,[5] both with and without filtering. In all three cases the average dispersion is the same. In the first case, the dispersion is held constant. As expected this case is by far the worst case. The reason is that as the soliton amplitude changes between amplifiers, the ideal balance between dispersion and nonlinearity is disrupted. Consequently, there is four wave mixing that leads to significant timing jitter. In principle, one can avoid this difficulty by using an exponentially tapered dispersion profile. In the case of an unfiltered system, this tapered system corresponds to a system that obeys the nonlinear Schrödinger equation and is therefore completely integrable. Nonetheless, significant timing jitter results. First, even ideal solitons undergo time shifts when they interact. Second, neighboring solitons in the same channel are sometimes jittered close to each other and they then attract due to the mutual interaction. This effect accounts for the tendency for the average jitter in some of the channels to suddenly jump. Even in a filtered system, the timing jitter in the exponentially tapered system is signficant. Remarkably, we find that the dispersion-managed system actually performs *better* than the exponentially tapered system both in the filtered and unfiltered systems. Since the dispersion-managed system is far easier to construct,

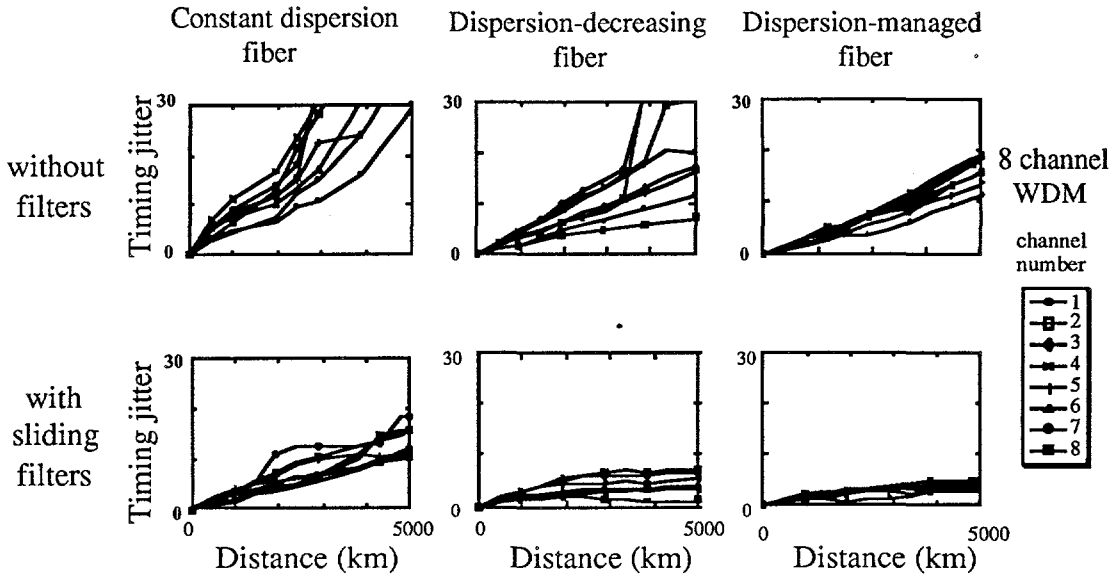

FIGURE 4. Variation of the timing jitter as a function of distance for eight channels in a WDM system. The behavior of systems with constant dispersion, exponentially tapered dispersion, and with strong dispersion management are compared with and without filtering. For the cases shown, the frequency separation of the channel is six times the FWHM channel bandwidth.

there is clearly no advantage at all to using an exponentially tapered system. We note as an aside that the results shown in Fig. 4 apply when the channel spacing is six times the full-width half maximum (FWHM) channel bandwidth. We also made a similar calculation when the channel spacing is twelve times the FWHM channel bandwidth and found that the exponentially tapered system performs slightly better than the dispersion-managed system, but, even in this case, there is no advantage to using an exponentially tapered system because it is so much harder than the dispersion-managed system to construct.

In a practical system, one must always have some amplitude margin, and it is therefore impossible to create the precise circumstances required to obtain periodically stationary pulses except in single-channel systems with sufficiently strong filtering to force the initial pulse shape into an exact dispersion-managed soliton. However, it is apparent that operating with dispersion-managed solitons—or as close as practically possible—has significant advanatages over both classical solitons and classical NRZ signals, as shown in Fig. 5. A dispersion-managed soliton system shares with an NRZ system the advantages that no sliding or other form of control is required for it to work well. This advantage is closely coupled to the advantage that the average dispersion can be held quite low, like in an NRZ system, so that the timing jitter due to spontaneous emission noise is small. At the same time, a dispersion-managed soliton system shares with a classical soliton system the advantages that no final dispersion compensation is required and there is no accumulated distortion. A further advantage that the dispersion-managed soliton system shares with a classical soliton system is that it is relatively simple to model what is happening in the system which in turn makes the system easier to design.

	NRZ	Solitons	DMS/PSP
no sliding / pulse control	✓		✓
no final compensation		✓	✓
no accumulated distortion		✓	✓
no large total dispersion	✓		✓
simple analysis		✓	✓

FIGURE 5. Relative advantages of NRZ signals, standard solitons and dispersion-managed solitons (periodically stationally pulses) are compared. The combination of low dispersion and stationarity implies that dispersion-managed solitons apparently combine the best features of NRZ and standard soliton systems.

3. FORMAT CONVERGENCE

Because one cannot precisely control the amplitude of the signals in a practical WDM system, the distinction between dispersion-managed solitons and return-to-zero (RZ) signals becomes gray in practice. There is a continuum of initial conditions with which RZ signals can successfully propagate which includes signals that are exactly periodically stationary as a special case. Even in a filtered system—and all our experiments thus far have been filtered—there is a long transient that is typically around 10,000 km before the system settles down to periodically stationary behavior. This distance is around the maximum possible length for practical systems! In practice, therefore, we consider the long battle between solitons and NRZ as the format of choice to be over. The winner is an intermediate format that allows the user to combine the advantages of both; the two formats have converged.

We originally constructed the recirculating loop in which we did our soliton experiments in order to be able to compare both soliton and NRZ signals in the same recirculating loop. We succeeded in this goal as shown in Fig. 6. Since our central purpose has been to determine the physical effects that lead to errors in both the soliton and NRZ systems, we developed a unique diagnostic that allows to assess the source of errors. In a bit error rate detector (BERT), the incoming optical energy is integrated over a single bit and turned into an electronic signal. If that signal is above a threshold that is set by the user it is counted as a 1, and if it is below that threshold it is counted as a 0. By changing the threshold and plotting the threshold values at which the error rate is greater than 10^{-6}, we can obtain some insight into the source of the errors. We found in our experiments that the source of errors for the solitons was the growth of spontaneous emission noise in the 0's; we found that the source of errors for the NRZ signals was intersymbol interference in the 1's.[9] It was the success of our experiment with the solitons, showing that timing jitter

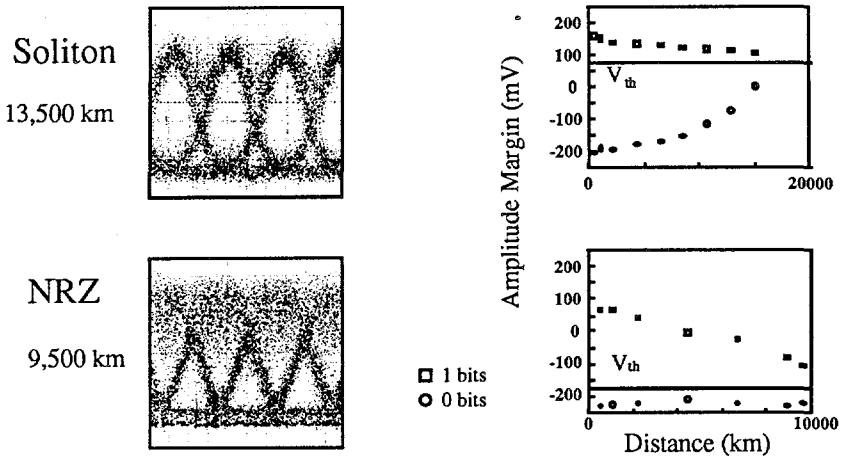

FIGURE 6. Relative advantages of NRZ signals, standard solitons and dispersion-managed solitons (periodically stationally pulses) are compared. The combination of low dispersion and stationarity implies that dispersion-managed solitons apparently combine the best features of NRZ and standard soliton systems.

of the 1's did not limit the system in contrast to standard solitons, that suggested that we should increase the bandwidth of the filters. Increasing the bandwidth of the filters from 1.3 nm to 2.8 nm allowed us to obtain a record-breaking 24,500 km propagation with an error rate of less that 10^{-9} in a system with no sliding filters or active soliton control.[10]

4. DISCUSSION AND CONCLUSIONS

In the last three years a remarkable shift has occurred in the way in which the optical fiber communication community views the possible communication formats. It used to be thought that the soliton and NRZ formats were fundamentally different and that one had to choose between them. Recent work has shown that in fact these two formats are connected by a continuum of possibilities and the best formats lie somewhere in the middle. We have explored dispersion-managed solitons, one element of that continuum, and we have shown that it shares many of the advantages of both classical solitons and NRZ while eliminating their disadvantages. A unique feature of our work has been the careful comparison of theory and experiment with an emphasis on determining the physical origins of the errors in communications systems.

In the future, we will push forward to experiments at 20 Gbits/sec and higher and to WDM systems, but our emphasis throughout will be on determining the physical sources of errors and on a careful comparison of theory and experiment. Since the large telecommunication companies are not doing this, we believe that we have a unique and important contribution to make to the development of future high data rate communication systems.

ACKNOWLEDGMENT

This work was supported by the Department of Energy.

REFERENCES

1. N. S. Bergano, "Undersea Amplified Lightwave Systems Design," *Optical Fiber Telecommunications IIIA*, I. P. Kaminow and T. L. Koch, eds. (Academic, San Diego, 1997), Chap. 10.
2. L. F. Mollenauer, J. P. Gordon, and P. V. Mamyshev, "Solitons in High Bit-Rate, Long-Distance Transmission," *Optical Fiber Telecommunications IIIA*, I. P. Kaminow and T. L. Koch, eds. (Academic, San Diego, 1997), Chap. 12.
3. G. M. Carter, J. M. Jacob, C. R. Menyuk, E. A. Golovchenko, and A. N. Pilipetskii, Opt. Lett. **22**, 513 (1997).
4. T. Yu, E. A. Golovchenko, A. N. Pilipetskii, and C. R. Menyuk, Opt. Lett. **22**, 793 (1996).
5. E. A. Golovchenko, A. N. Pilipetskii, and C. R. Menyuk, Electron. Lett. **33**, 735 (1997); Opt. Lett. **22**, 1156 (1997).
6. See, *e.g.*, N. S. Bergano, *et al.*, *Optical Fiber Communication Conference 1998*, paper PD12-1.
7. N. J. Smith, F. M. Knox, N. J. Doran, K. J. Blow, and I. Bennion, Electron. Lett. **32**, 54 (1996).
8. R.-M. Mu, V. S. Grigoryan, C. R. Menyuk, E. A. Golovchenko, and A. N. Pilipetskii, "Timing Jitter Reduction in a Dispersion-Managed Soliton System," Opt. Lett. (to appear).
9. J. M. Jacob, E. A. Golovchenko, A. N. Pilipetskii, G. M. Carter, and C. R. Menyuk, IEEE Photon. Technol. Lett. **9**, 1412 (1997).
10. J. M. Jacob and G. M. Carter, Electron. Lett. **33**, 1128 (1997).

NONLINEAR DYNAMICS AND PATTERN FORMATION

Jorge Viñals

Supercomputer Computations Research Institute
Florida State University
Tallahassee, FL 32306-4130
and
Department of Chemical Engineering
FAMU-FSU College of Engineering
Tallahassee, FL 32310-6046

ABSTRACT

The objectives of our research are to improve our understanding of the mechanisms underlying the formation of complex spatio-temporal patterns in systems that are driven outside of thermodynamic equilibrium, to characterize the macroscopic properties of such states, and to apply the methodology to situations of interest in fluid physics and engineering. Current research focuses on pattern formation, secondary instabilities and the transition to spatio-temporal chaos in parametrically driven surface waves, and the development of hydrodynamic equations at the mesoscopic level to model short length scale phenomena that fall beyond a conventional hydrodynamic description.

INTRODUCTION

Fluid systems have provided a wealth of information on a variety of nonlinear phenomena that include bifurcation and instability, pattern formation, front propagation, localized and traveling states, intermittency, spatio-temporal chaos, and turbulence. Many fluid systems have become paradigms of one or more of these fundamental phenomena and thus have been studied extensively both theoretically and experimentally. Among the reasons why fluids have received such a widespread attention from the nonlinear dynamics community we note the clear separation between time and length scales that make them especially amenable to theoretical treatment, the relative ease with which accurate experiments can be performed, and, finally, the fact that many of the physical parameters that characterize the properties of the fluid can be measured with sufficient accuracy. As a consequence, the study of fluid instabilities and the ensuing formation of patterns has become one of the major fields of study in nonlinear physics today. Of particular concern to us is the study of large aspect ratio systems, both because they have been a very fertile area of experimentation recently, and because renewed importance has been given to a statistical description of such extended systems.

A great deal of our research effort has been devoted to the study of parametrically driven surface waves (also known as Faraday waves) in the large aspect ratio limit. Faraday waves are an ideal

laboratory in which to explore cooperative behavior in extended, quasi-Hamiltonian systems, and has been the subject of intense study during the past few years. Active modes above threshold are only weakly damped (or not damped at all in the inviscid limit), so that the governing equations are close to being purely Hamiltonian in nature. This is in contrast to other widely studied pattern forming systems in which overdamped motion is dominant. One important by-product of this research activity has been the discovery of stable quasi-periodic patterns (the analog of quasi-crystalline states in solids). We anticipate continued activity in this field in a number of diverse topics such as the nature of the chaotic state, elucidating mean flow effects and spiral patterns, tracer transport by nonlinear waves in periodic, quasi-periodic and disordered patterns, and perhaps in using this system as a door to further explore quantum chaos by exploiting the wave nature of a quantum system vis a vis the Hamiltonian nature of Faraday waves.

We also briefly touch upon a separate area of research that, although focusing on nonlinearity in fluid systems, addresses issues different from those discussed above. It concerns a mesoscopic description of a fluid system to study re-orientation dynamics of a lamellar structure. Such a mesoscopic approach has already been used to study interfacial motion and microstructure evolution in multiphase flows. As developed, the model naturally accommodates topological changes in two-phase interfaces, phenomena that fall beyond classical macroscopic fluid mechanics. We are currently investigating short scale phenomena such as contact line motion and the rheology of lamellar structures in block co-polymers. These latter materials are expected to display interesting properties associated with their strong anisotropy, and also to serve as convenient patterning substrates since their wavelength can be easily adjusted by modifying the length of the polymer chain. Typical lamellar spacings are of the order of 100 Å, and hence a continuum hydrodynamic description is not expected to be valid. A mesoscopic model appropriate for block co-polymers has been developed, and we are currently investigating the re-orientation dynamics of a disordered lamellar structure and its interaction with an externally imposed shear.

FARADAY WAVES

Parametrically driven surface waves (also known as Faraday waves) can be excited on the free surface of a fluid layer that is periodically vibrated in the direction normal to the surface at rest if the amplitude of the driving acceleration is large enough to overcome the dissipative effect of fluid viscosity [1, 2]. Despite the simplicity of the configuration this system displays a large number of features that are characteristic of strong nonlinearity, and has served as a prototype of many nonlinear phenomena that are currently under active investigation. Among them we mention the discovery of stationary quasi-periodic patterns of surface standing waves (the analog of a quasi-crystal in solid state physics) [3, 4], the transition to spatio-temporal chaos [5], the coexistence of chaotic and regular regions in an extended system, and a laboratory for detailed studies of turbulence [6].

Our study focuses on the large aspect ratio limit in which the lateral dimensions of the system are much larger than the wavelength of the wave, and sufficiently close to threshold of the primary instability so that the description can be made at the level of slow modulations of a base pattern of standing waves. We first touch upon the salient features and results of the weakly nonlinear regime above onset, and especially the interplay between two small parameters: the dimensionless distance away from threshold ε, and the viscous damping parameter γ. We then discuss recent progress on pattern selection. It is now known that different wave patterns can be excited depending on the fluid properties and the driving frequency. At high viscous dissipation (a fluid of large viscosity and/or a low driving frequency), the observed wave pattern above threshold consists of parallel

stripes [4]. For lower dissipation, patterns of square symmetry (combinations of two perpendicular plane waves) are observed in the capillary regime of large frequencies [7, 5, 3, 4]. At low frequencies (the mixed gravity-capillary regime), higher symmetry patterns have been observed: hexagonal [8, 9], and eight- and ten-fold patterns [9]. We finally discuss briefly recent results on secondary instabilities and the transition to a spatio-temporal chaotic state.

Standing wave amplitude equations

Consider a semi-infinite fluid layer, unbounded in the $x-y$ direction, extending to $z=-\infty$, and with a planar free surface at $z=0$ when at rest. The fluid is assumed incompressible and Newtonian. Under periodic vibration of the layer in the direction normal to the surface at rest, the equation governing fluid motion (in the co-moving reference frame) is the Navier-Stokes equation with an effective periodic gravitational field. This equation is supplemented by standard boundary conditions describing the kinematics of an infinitely thin fluid surface, and momentum conservation at the surface (allowing for capillarity). The base state is a quiescent fluid with a time dependent pressure. Linearization of the governing equations and boundary conditions around the base state leads to the following equation for each Fourier component $\zeta_k(t)$ of the surface displacement [10],

$$\begin{aligned}\partial_{tt}\zeta_k &+ 4\nu k^2\partial_t\zeta_k + \left(\frac{\sigma k^3}{\rho} + gk + 4\nu^2k^4 + kf\cos\omega t\right)\zeta_k \\ &- 4\nu k^2\sqrt{\frac{\nu k^2}{\pi}}\int_0^t dt'\left(\partial_{t'}\zeta_k(t') + \nu k^2\zeta_k(t')\right)\frac{\exp\left[-\nu k^2(t-t')\right]}{\sqrt{t-t'}} = 0. \qquad (1)\end{aligned}$$

where ν and ρ are the kinematic viscosity and density of the fluid respectively, σ the interfacial tension, g the intensity of the gravitational field and f the amplitude of the periodic driving acceleration of angular frequency ω.

The linear stability of the fluid layer was first addressed in the inviscid limit by Benjamin and Ursell [11]. Equation (1) with $\nu=0$ reduces to the Mathieu equation for $\zeta_k(t)$, the solutions of which are well known. A set of instability regions (or "tongues") appear in a (k,f) diagram that intersect the $f=0$ axis. Solutions within these regions are oscillatory with frequency $\omega_n = \frac{n+1}{2}\omega$, $n=0,1,2,\ldots$ and an exponentially increasing amplitude. The fact that the unstable regions intersect the $f=0$ line indicates that there is no threshold for instability. The limit of small viscous dissipation has been considered by adding a phenomenological damping term to the Mathieu equation (identical to the the second term in the left hand right of Eq. (1)). Damping removes the degeneracy of the inviscid modes and introduces a finite threshold value of f for instability which is a function of n. The lowest threshold corresponds to $n=0$ and hence to subharmonic resonance. The threshold value in this approximation is, $f_0 = \nu k_0\omega_0/2$, where the wave number k_0 is determined by the resonance condition and the linear dispersion relation for inviscid waves $\omega/2 = \omega_0 = gk_0 + \sigma k_0^3/\rho$. At the linear level in the surface variables, the leading order contribution to damping (of order ν) is due to bulk damping of the irrotational flow component. The rotational component contribution appears in the integral kernel of Eq. (1) and its leading order scales as $\nu^{3/2}$.

More recently, an exact albeit implicit expression for the instability threshold for arbitrary viscous dissipation has been given in [12]. We quote here an approximation valid for small viscous dissipation. Define dimensionless variables by using $1/\omega_0$ as the time scale, and $1/k_0$ as the length scale. We also define a reduced wave number $\bar{k} = k/k_0$, a viscous damping coefficient $\gamma = 2\nu k_0^2/\omega_0$, the gravity wave $G = gk_0/\omega_0^2$ and capillary wave $\Sigma = \sigma k_0^3/\rho\omega_0^2$ contributions to the dispersion relation, and the dimensionless amplitude of the driving acceleration $\Delta = fk_0/4\omega_0^2$. $G=1$ corresponds

to a pure gravity wave while $G = 0$ to a pure capillary wave. For $\gamma \ll 1$, we have found

$$\begin{aligned} \bar{k}_{\text{onset}} &= 1 + \tfrac{1}{3-2G}\gamma^{3/2} + \tfrac{-7+2G}{(3-2G)^2}\gamma^2 + \ldots, \\ \Delta_{\text{onset}} &= \gamma - \tfrac{1}{2}\gamma^{3/2} + \tfrac{11-2G}{8(3-2G)}\gamma^{5/2} + \ldots. \end{aligned} \tag{2}$$

The first correction term is proportional to $\gamma^{3/2}$, and arises from the rotational flow component.

The derivation of nonlinear amplitude equations for surface waves is greatly simplified in the case of an ideal (inviscid) fluid. In this case there exists a Hamiltonian formulation in which the canonically conjugate variables are the surface displacement and the velocity potential at the free surface. As a consequence, early analyses of Faraday waves were based on the Hamiltonian description of the inviscid limit, and treated viscous or dissipative effects as a perturbation [13, 14, 15]. An expansion of the ideal fluid equations to third order in the wave amplitude $A_j(T)$, where $T = \varepsilon t$ is a slow time scale, yields,

$$\frac{dA_j}{dT} = -\frac{ikf}{4\omega}A^*_{-j} + i\sum_k \Pi^{(1)}_{jk}|A_k|^2 A_j + i\sum_k \Pi^{(2)}_{jk} A_k A_{-k} A^*_{-j}, \tag{3}$$

where Π are *real* functions of the angle between the j-th and k-th wavevectors. Since the coefficients of the cubic terms are imaginary, these terms do not contribute to wave saturation. This is also a manifestation of a general symmetry principle in Hamiltonian (or reversible) systems that prohibits *real* coefficients of cubic nonlinear terms in standing wave amplitude equations [2]. Several mechanisms have been proposed to account for nonlinear saturation. In the limit of low viscous dissipation, Hamilton's equations have been supplemented with a dissipation function [13, 14, 15], which is computed under the assumption that the dominant contribution to viscous dissipation arises from the irrotational velocity field in the bulk, and not from dissipation near the free surface (where vorticity is produced). This assumption is based on the relative scaling with γ of the irrotational and rotational flow contributions at the linear level discussed above. This procedure leads to imaginary components in the coefficients of the cubic terms of Eq. (3), and therefore to wave saturation. The precise functional form of the coefficients obtained by this method is still somewhat controversial [15, 16].

More recently, we have argued that rotational flow contributes at order γ to the coefficients of the cubic order terms in the amplitude equation, and hence cannot be neglected compared to the irrotational contribution, even in the limit of small γ [17]. In other words, a nonlinear theory must be based on a viscous formulation from the start no matter how small viscous dissipation is (the limit $\gamma \to 0$ is singular). Second, we have shown that the dominant mechanism of wave saturation involves dissipation through linearly stable second order waves. Their damping coefficient is γ, and their amplitude proportional to $1/\gamma$. It can be shown that their contribution to the coefficients of the cubic order in the amplitude equation becomes dominant at small γ. For a driving amplitude f above the threshold f_0, define $\varepsilon = (f - f_0)/f_0$. The flow is expanded as $\mathbf{u} = \varepsilon^{1/2}\mathbf{u_0} + \varepsilon\mathbf{u_1} + \varepsilon^{3/2}\mathbf{u_2} + \cdots$ Near threshold, i.e., for $\varepsilon \ll 1$, the slow time scale is $T = \varepsilon t$. At order $\varepsilon^{1/2}$ one recovers the linear problem. The solution at this order is written as a linear combination of waves with wave vectors $\mathbf{k}_m$ of magnitude k_{onset} but along different directions on the x–y plane,

$$\zeta_0 = \sum_m \cos(\mathbf{k}_m \cdot \mathbf{x}) B_m(T) \sum_{j=1,3,5,\cdots} e^{ji\omega t/2} e_j + \text{c.c.},$$

where $B_m(T)$ are *real* wave amplitudes, functions only of the slow time scale T, and the e_j are amplitudes given by the linear solution. At order $\varepsilon^{3/2}$ a solvability condition appears that leads to

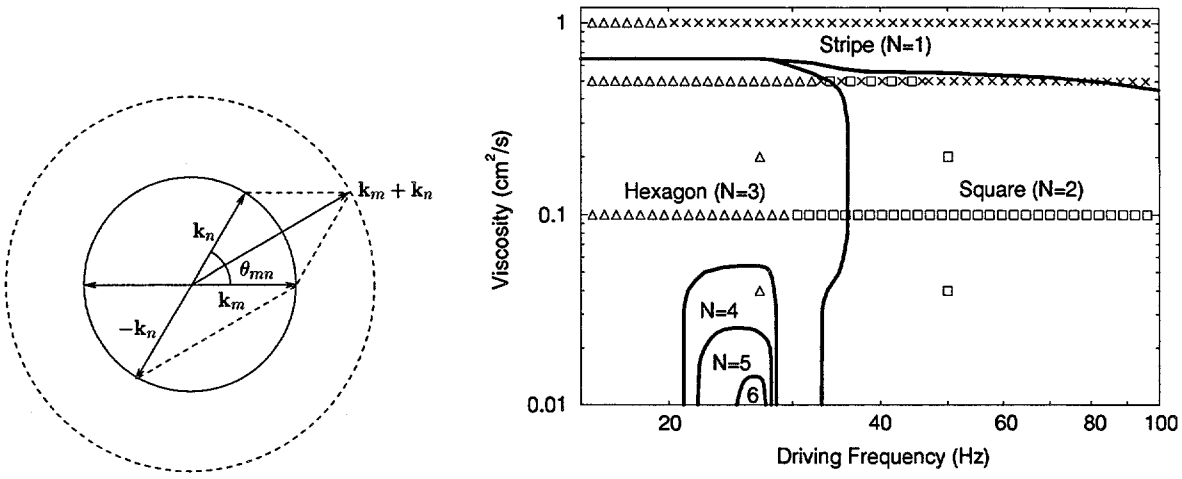

Figure 1: Left: Schematic representation of a triad resonant interaction: two linearly unstable modes $\mathbf{k}_m$ and $\mathbf{k}_n$ interact to produce a linearly stable mode. This mode interacts with $-\mathbf{k}_n$ leading to a resonance with $\mathbf{k}_m$. Right: Selected patterns as a function of fluid viscosity and driving frequency. The symbols are the experimental results of [8]. $\times$, stripe patterns; $\square$, square patterns; and, $\triangle$, hexagonal patterns. Alternating $\times$ and $\square$ indicate regions in which stationary mixed stripe and square patterns were observed.

a standing wave amplitude equation for a particular unstable mode B_1,

$$\frac{dB_1}{dT} = \alpha B_1 - g_0 B_1^3 - \sum_{m \neq 1} g(\theta_{m1}) B_m^2 B_1, \tag{4}$$

with θ_{m1} the angle between $\mathbf{k}_m$ and $\mathbf{k}_1$. The coefficient α is the linear growing or decaying rate of this wave, and can be obtained from the linear analysis. The coefficient $g(\theta)$ describes the nonlinear interaction between different linearly unstable modes, and provides for the saturation of the wave amplitude. Figure 1 shows two linearly unstable modes with wave vectors $\mathbf{k}_m$ and $\mathbf{k}_n$ ($|\mathbf{k}_m| = |\mathbf{k}_n| = k_{\text{onset}}$). They interact to produce a wave at $\mathbf{k}_m + \mathbf{k}_n$ with an amplitude proportional to $B_m B_n$. This mode corresponds to a first order solution. Now $\mathbf{k}_m + \mathbf{k}_n$ couples back to the original wave at $-\mathbf{k}_n$ to give a contribution $B_n^2 B_m$ to dB_m/dT. Since the mode $\mathbf{k}_m + \mathbf{k}_n$ is damped (only waves with wave numbers near k_{onset} are unstable), this is a dissipative term and contributes to nonlinear saturation of the wave. Furthermore, triad resonance occurs when the frequency of the mode $\mathbf{k}_m + \mathbf{k}_n$ equals the driving frequency (the modes $\mathbf{k}_m$ and $\mathbf{k}_n$ oscillate at half the driving frequency). Energy is now directly transferred into this mode which can have a very large amplitude at low damping. This coupling provides a dissipation channel for the mode $\mathbf{k}_n$, so that dissipation is enhanced by triad resonance and results in a large value of $g(\theta_{mn})$ in the vicinity of the resonant angle. The resonant angle can be estimated from the inviscid dispersion relation, written in dimensionless form, $\bar{\omega}^2 = G\bar{k} + \Sigma\bar{k}^3$, with $\bar{k} = 1$, and $\bar{\omega}^2 = G + \Sigma = 1$ for the linearly unstable mode. A stable mode will be in resonance when $\bar{\omega} = 2$, and the resonant wave number $\bar{k}_r = |\bar{\mathbf{k}}_m + \bar{\mathbf{k}}_n|$ satisfies $\bar{k}_r\,(G + \Sigma\bar{k}_r^2) = 4$. If θ_r is the resonant angle between $\mathbf{k}_m$ and $\mathbf{k}_n$, $\bar{k}_r = \sqrt{2(1+\cos\theta_r)}$, the resonance condition becomes

$$\sqrt{2(1+\cos\theta_r)}[G + 2(1+\cos\theta_r)\Sigma] = 4. \tag{5}$$

Because $G + \Sigma = 1$, this condition can only be satisfied when $\Sigma > 1/3$. For finite damping, the resonance condition is modified. More generally, three wave resonant interactions are permitted when the dispersion relation of the wave satisfies $\partial^2 w/\partial k^2 \geq 0$, as is the case in the capillary regime. For gravity waves $\partial^2\omega/\partial k^2 < 0$, and only four wave resonant interactions are possible. Triad resonance is expected to be significant only at low damping because of the damped nature of the stable wave. In fact, we have shown that a sequence of quasi-periodic patterns of increasingly higher symmetry is expected when the triad resonant angle approaches zero (around $\Sigma = 1/3$) and with decreasing γ [12].

Since the standing wave amplitude equation (4) can be written in gradient form, the selected pattern near threshold immediately follows by minimization of the associated Lyapunov function [2]. The experimentally observed regular patterns above onset consist of N standing waves, with uniform amplitudes and wave vectors $\mathbf{k}_m, m = 1 \ldots N$. Our results are summarized in Fig. (1). In this figure we also show a set of recent experiments involving fluids of different viscosity by Kudrolli and Gollub [8]. The figure shows the symmetry of the predicted patterns as a function of the viscosity of the fluid and of the driving frequency (with the appropriate experimental parameters $\rho = 0.95\text{g/cm}^3$ and $\sigma = 20.6\text{dyn/cm}$), together with the experimentally observed patterns. They are stripes at high viscosity, hexagons at low viscosity and frequency, and squares at low viscosity and high frequency. Two significant discrepancies concern the experimental observation of a hexagonal pattern at $\nu = 1\text{cm}^2/\text{s}$ and low frequency, and also at $\nu = 0.04\text{cm}^2/\text{s}$ and $f = 27\text{Hz}$. It is possible that the shallowness of the fluid layer (0.3 cm, smaller than the wavelength of the waves 1-3 cm) can account for these difference. The low viscosity and large aspect ratio range has also been studied experimentally in [9]. When the driving frequency is decreased from 45Hz, a transition from a $N = 2$ square pattern to a $N = 3$ hexagonal pattern was observed at approximately 35Hz, and to a quasi-periodic $N = 4$ eight-fold pattern at approximately 29Hz. Our predictions for these transitions are 35.4 Hz and 28.7 Hz respectively.

Transition to spatio-temporal chaos

In order to study secondary instabilities of the base pattern and the transition to spatio-temporal chaos, we have developed an order parameter model that preserves the original rotational invariance of the fluid equations [18]. With this model, we have found roll-like and square patterns near onset of the parametric instability, and various secondary instabilities (Eckhaus, zig-zag, transverse amplitude modulation). The Eckhaus stability boundary is found to be reentrant as a function of ε, and to cross the transverse amplitude modulation boundary at a finite value of ε. This fact provides a mechanism for the finite threshold observed experimentally for the appearance of the transverse amplitude modulation [5, 7]. Numerical solutions of the model are in agreement with this bifurcation diagram, and also reveal the existence of a transition to spatio-temporal chaotic states. This transition is seen to occur because of the interplay between the stability regions corresponding to the Eckhaus instability and the transverse amplitude modulation. For a sufficiently large value of ε, the amplitude of the transverse modulation becomes time dependent, its dynamics becoming increasingly complex as ε increases, ultimately leading to chaos. Power spectra of temporal fluctuations in the chaotic state are broadband, decaying as a power law of frequency with an exponent approximately equal to four.

FLUID DYNAMICS OF LAMELLAR STRUCTURES

Moving boundary problems are encountered in a variety of fields such as phase change, solidification studies, or multi-phase flows. In them, the relevant variables satisfy partial differential equations in one or more bulk regions subject to boundary conditions specified at moving interfaces. The position and motion of these interfaces has to be determined simultaneously with the solution inside the bulk. Analytic solutions are rare, and computational approaches are very demanding because of the need to track the location of the moving boundaries. A complementary methodology involves a mesoscopic description of the system in which any boundary of separation (infinitely thin and without structure in the classical macroscopic approach) is effectively replaced by a transition region of small but finite width by defining a suitable order parameter [19]. All magnitudes are then continuous throughout the entire system, with some of them changing rapidly over length scales of the order of the width of the transition regions. The main advantage of the method is that both domain interiors and interfacial regions are treated on an equal footing, and hence a single set of governing equations is solved throughout the system. The location of the interfaces appears naturally as part of the solution: the regions in which the order parameter changes between the values corresponding to each phase. Shortcomings of this method include the need to resolve the transition region (thus limiting the range of length scales that can be studied in practice numerically), and the need to explicitly model the physical behavior of the system at the mesoscopic scale. The latter is beyond the scope of classical thermodynamic treatments, and has to be dealt with phenomenologically, with the requirement that the mesoscopic model has to reduce to the known macroscopic model in the limit of vanishingly small interfacial thickness. This is in itself an active area of research, with established results only for the simplest models. Computationally, the approach has yielded a number of successes in the areas of phase change (Ginzburg-Landau or Cahn-Hilliard equations), and solidification (phase field models). In both cases, the models that have been used are purely dissipative. When studying multi-phase flow, however, reversible contributions (non-dissipative) are important and have to be explicitly included.

We are currently using this methodology to study shear alignment of block co-polymers near the isotropic-lamellar transition. Below the transition point, the material forms a locally periodic composition pattern (the so-called micro-phases) with characteristic wavelength of the order of 100 Å. The effect of an imposed periodic shear on the resulting textured domain structure is being analyzed in order to determine the mechanisms controlling re-orientation dynamics, the motion of topological defects, and the evolution towards a macroscopically ordered system.

ACKNOWLEDGMENTS

This research has been supported by the U.S. Department of Energy, contract No. DE-FG05-95ER14566, and also in part by the Supercomputer Computations Research Institute, which is partially funded by the U.S. Department of Energy, contract No. DE-FC05-85ER25000.

REFERENCES

[1] J. Miles and D. Henderson, "Parametrically forced surface waves", *Annu. Rev. Fluid Mech.* **22**, 143 (1990).

[2] M. Cross and P. Hohenberg, "Pattern formation outside of equilibrium", *Rev. Mod. Phys.* **65**, 851 (1993).

[3] B. CHRISTIANSEN, P. ALSTRØM, AND M. LEVINSEN, "Ordered capillary-wave states: quasicrystals, hexagons and radial waves", *Phys. Rev. Lett.* **68**, 2157 (1992).

[4] W. EDWARDS AND S. FAUVE, "Patterns and quasi-patterns in the Faraday experiment", *J. Fluid Mech.* **278**, 123 (1994).

[5] N. TUFILLARO, R. RAMSHANKAR, AND J. GOLLUB, "Order-Disorder Transition in Capillary Ripples", *Phys. Rev. Lett.* **62**, 422 (1989).

[6] W. WRIGHT, R. BUDAKIAN, AND S. PUTTERMAN, "Diffusing light photography of fully developed isotropic ripple turbulence", *Phys. Rev. Lett.* **76**, 4528 (1996).

[7] A. EZERSKII, M. RABINOVICH, V. REUTOV, AND I. STAROBINETS, "Spatiotemporal chaos in the parametric excitation of a capillary ripple", *Zh. Eksp. Teor. Fiz.* **91**, 2070 (1986), [Sov. Phys. JETP **64**, 1228 (1986)].

[8] A. KUDROLLI AND J. GOLLUB, "Patterns and Spatiotemporal Chaos in Parametrically Forced Surface Waves: A Systematic Survey at Large Aspect Ratio", *Physica D* **97**, 133 (1996).

[9] D. BINKS AND W. VAN DE WATER, "Nonlinear pattern formation of Faraday waves", *Phys. Rev. Lett.* **78**, 4043 (1997).

[10] NAM HONG U, "A new approach to parametric excitation of stattionary surface waves in a viscous liquid", *Bulletin of the Russian Academy of Sciences - Physics/Supplement* **57**, 131 (1993).

[11] T. BENJAMIN AND F. URSELL, "The stability of the plane surface of a liquid in vertical periodic motion", *Proc. R. Soc. London Ser. A* **225**, 505 (1954).

[12] P. CHEN AND J. VIÑALS, "Pattern Relection in Faraday Waves", *Phys. Rev. Lett.* **79**, 2670 (1997).

[13] J. MILES, "Nonlinear Faraday resonance", *J. Fluid Mech.* **146**, 285 (1984).

[14] S. MILNER, "Square patterns and secondary instabilities in driven capillary waves", *J. Fluid Mech.* **225**, 81 (1991).

[15] J. MILES, "On Faraday waves", *J. Fluid Mech.* **248**, 671 (1993).

[16] P. HANSEN AND P. ALSTRØM, "Perturbation theory of parametrically driven capillary waves at low viscosity", *J. Fluid Mech.* **351**, 301 (1997).

[17] W. ZHANG AND J. VIÑALS, "Pattern formation in weakly damped Faraday waves", *J. Fluid Mech.* **336**, 301 (1997).

[18] W. ZHANG AND J. VIÑALS, "Secondary Instabilities and Spatiotemporal Chaos in Parametric Surface Waves", *Phys. Rev. Lett.* **74**, 690 (1995).

[19] D. JASNOW AND J. VIÑALS, "Coarse-grained description of thermo-capillary flow", *Phys. Fluids* **8**, 660 (1996).

USING NONLINEAR "BLACK-BOX" TECHNIQUES FOR CONTROL TRAJECTORY PLANNING AND CHANNEL EQUALIZATION

Lev S. Tsimring[1], Nikolai F. Rulkov[1], and H.D.I.Abarbanel[1,2]

([1]) Institute for Nonlinear Science
([2])Department of Physics and Scripps Institution of Oceanography

University of California, San Diego
La Jolla, California 92093-0402

ABSTRACT

The results of research on developing nonlinear modeling techniques for control and channel equalization are presented. The techniques are based on probing the structure of unknown "black-box" nonlinear system by external driving and building inverse nonlinear models directly from data.

INTRODUCTION

Traditionally, for ease of operation and analysis, technological systems (manufacturing systems, power plants, communication systems, etc.) have been designed to behave in as linear a manner as possible. Increasingly tight specifications, environmental considerations and economic pressures are pushing the operational windows into regions where assumptions of linearity tend to break down. Standard linear techniques for system identification and control do not work for nonlinear systems, and new approaches to the problem are needed. In this paper we present our results on developing tools tools for building nonlinear models for low-dimensional systems based on experimental data (in particular, input/output time series) and developing control techniques exploiting these models.

In the last decade, significant progress was achieved in the control field. Complex multivariable control schemes are now routinely applied in a number of industrial sectors. It must be noted however that most of these control schemes are essentially linear techniques based on the assumption that the process in hand is itself linear. These techniques are bound to fail in the operational regimes in which the system behaves *nonlinearly*. Control theorists started to recognize this challenge[1]. Extensions of model predictive control have been proposed to deal with nonlinear systems, either using local linear approximations [2], or by solving complex dynamic nonlinear optimization problems on-line [3].

On the other hand, in the nonlinear dynamics community a great interest in controlling low-dimensional chaotic system was initiated by the pioneering work by Ott, Grebogi, and Yorke (OGY)[4]. In this line of work, a local model of system dynamics near the desired periodic orbit is learned from the scalar output of the autonomous system and then used to adjust the value of an (arbitrary) control parameter to bring the system to the stable manifold of the desired orbit. The model operates in the embedding phase space which is reconstructed using well-established numerical methods[5]. It is crucial to the control of nonlinear systems exhibiting chaos that the control methods be employed in the multivariate reconstructed phase space.

OGY method works by linearizing the dynamical equations in a small state space neighborhood of the target trajectory and controlling only when the system state enters that neighborhood. This method requires knowledge of the stable and unstable manifolds of the target trajectory, and this must be learned from the data or from a good model of the dynamical system. Similarly, in the occasional proportional feedback (OPF) method [6, 7, 8], a simple linear feedback controller is used in a small neighborhood of the target trajectory, with the same argument that the system will eventually enter this neighborhood, where control is easy.

Another class of chaotic control schemes attempts to drive a system such that an arbitrary goal trajectory is tracked. To this end, open-loop ("entrainment") control schemes have been suggested [9, 10, 11, 12, 13, 14]. Originally, entrainment control was utilized on known dynamical systems where the controlled inputs directly affect each state variable of the system[9]. Later this method was generalized for reconstructed dynamical systems[11] and an arbitrary combination of inputs. However, once again it was assumed that the inputs are able to entirely specify the state of the dynamical system[12]. Clearly, the number of controlled inputs cannot be less than the state dimension of the underlying dynamical system when using this control scheme. Additionally, the stability of this open-loop control scheme cannot be guaranteed unless certain conditions are fulfilled. In particular, goal trajectories must be contained within "convergent" regions[10, 12] of the state-space.

In the present paper, we expand and modify the entrainment control approach in the following ways. First, it is assumed that the state-space system to be controlled is single input/single output and the equations describing the state-space dynamics are unknown. It is assumed there is only a single input to the system, "full-state control" will not be possible. By choosing the proper input trajectory, the output of the system should track a desired output trajectory. Finally, as the system to be controlled is assumed to be unknown, the proper input will be found using only an input/output time-series from the system. This approach is particularly useful for chaotic systems, where it can be difficult to determine a state-space model which accurately describes the global behavior of the system using standard methods of identification.

Since our method utilizes time-series data from the system to compute the proper controlled input, we call this approach data-based control trajectory planning. In order to accomplish this task, input/output identification data which characterizes the dynamics of the *driven* nonlinear system are needed. The identification data consist of a time-series collected from the driven system with random variations in the driving input. The set of goal trajectories which can be tracked by this control scheme should consist of the set of all trajectories which are possible for the driven system, which is larger than the set of trajectories of the autonomous system.

We have also applied these ideas in areas of signal processing and communications. Indeed, the most crucial part of a communication system is the channel. Nonlinear and dispersive distortions as well as additive noise and attenuation limit the channel capacity. Usually, transmitter and receiver are carefully designed as to minimize the effect of noise and distortion on signal prop-

agation. Nevertheless, since it is impossible to avoid distortions completely, methods for signal recovery are being developed. Here we demonstrate how to learn the nonlinear properties of the channel on the basis of sample input-output data, build an inverse model, and use it to recover the transmitted (and corrupted) information.

INVERSE NONLINEAR MODELING

For linear systems, a well established theory of *optimal inverse modeling* has been developed (see, e.g. [15]). This theory tells us how to reconstruct an input signal from a given output signal. This is a process of inverse modeling, or *deconvolution.* If $x(t)$ is an input, $y(t)$ is an output of the system which has impulse response $f(t)$, then the inverse model with impulse response $g(t)$ is designed in order to make its output signal $x'(t)$ as close to $x(t)$ as possible. It is easy to see that going into Fourier space and taking simply

$$G(\omega) = \frac{1}{F(\omega)} \tag{1}$$

provides the desired deconvolution for a linear channel (F and G are Fourier images of f and g, respectively). However, it is well known that in general it is impossible to build a stable causal system which realizes this operation, although good approximate deconvolution may still be possible [15].

For nonlinear systems the situation is more complicated because they cannot be described by a unique impulse response function. Only a full set of nonlinear differential equations (or maps in the case of discrete time series) can provide complete information:

$$\begin{aligned} \frac{d\mathbf{u}}{dt} &= F(\mathbf{u}(t), x(t)), \\ y(t) &= h(\mathbf{u}(t)). \end{aligned} \tag{2}$$

Here $\mathbf{u}$ denotes a d-dimensional vector of variables describing the system dynamics, and $y(t)$ is an output. Note that even if we are given this information, it is not at all clear how to "invert" the system to get the optimal deconvolution of the original signal, namely, to build an inverse system

$$\begin{aligned} \frac{d\mathbf{v}}{dt} &= G(\mathbf{v}(t), y(t)), \\ x'(t) &= p(\mathbf{v}(t)). \end{aligned} \tag{3}$$

The basic idea of building an inverse nonlinear model is the following. Suppose we do not know the equations describing the nonlinear system, instead we do have a sample input signal $x_s(t)$ and the corresponding output $y_s(t)$. That is, we have observed an input $x_s(t)$ and an output $y_s(t)$ of the system of interest. The sample signal should be long and complex enough to drive the system throughout its state space. If we deal with a finite-dimensional system, as (2), then using this pair of signals one can build a model for this input-output system in the form [16]

$$y(t) = P(y(t-T), y(t-2T), ..., y(t-mT), x(t), x(t-T), ..., x(t-(l-1)T)), \tag{4}$$

where T is an appropriate time delay and P is a differentiable function.

Our goal here is in a sense inverse: we are looking for a model expressing the input signal through a sequence of outputs:

$$x(t) = Q(y(t), y(t-T), y(t-2T), ..., y(t-mT)), \tag{5}$$

or, more generally,

$$x(t) = Q(y(t+lT), ..., y(t+T), y(t), y(t-T), y(t-2T), ..., y(t-mT)), \tag{6}$$

No general rigorous results are known concerning the possibility of constructing this type of model (for some particular cases see [17]). Clearly, depending on the type of input signal and the type of system this may or may not be possible. We argue, however, that in a number of physically important cases a reasonably good approximate reconstruction of the type (6) is indeed possible (see below Section 4).

SYSTEM IDENTIFICATION, MODELING AND CONTROL

Suppose the system driven by external signal $x(t)$ is given by Eq.(4) For the purpose of open-loop trajectory planning, the input sequence $x(t)$ should be determined as a function of a desired output sequence $y(t)$. Using the implicit function theorem, eq. (4) can be locally inverted as

$$x(t) = Q[y(t+T), y(t), y(t-T), y(t-2T), ..., y(t-(l-1)T), x(t-T), ..., x(t-(m-1)T)] \tag{7}$$

Given the y terms (the values of the goal trajectory), this equation represents an m-dimensional non-autonomous mapping for the desired control x. Just as in case of modeling the output dynamics (4), this inverse map can be recovered from the data by using local polynomial models in the space of delayed versions of y and u. Once this map is determined locally, it can be used to calculate the "one-step ahead" control move $x(t)$ that will give the desired reference output $y(t+T)$.

Two problems may be encountered utilizing this local inversion process. First, it is possible that the control needed to produce the desired output is not contained in the data set. In this case, further identification with an input signal which has either a larger magnitude range or a wider frequency range may be needed. Second, the mapping Q from (7) is not guaranteed to be unique. For non-unique inverse mappings only the data corresponding to one branch of the inverse map can be used for inverse modeling purposes. If the data from both branches are used for building a model, the model will "average" the data from the two branches and the resulting computed future control move u will lie somewhere between the two branches. In this case, the computed control move will not produce the desired action.

Since the trajectory to be controlled may not be stable, it is possible that the computed open-loop control of the system may not stabilize the system. This is because it is difficult to exactly cancel the instability present in the trajectory of the open-loop system. In this case, additional closed-loop feedback control is needed to stabilize the system about the desired trajectory. Also, it is possible that the "inverse" mapping which produces the open-loop control law may be unstable itself. This leads us to believe that the dynamic system contains some locally nonminimum phase behavior, and the system may exhibit problems very similar to internal instability problems which can be found in linear systems when inverse controllers are used [19].

Additional complications arise when the periodic orbit to be tracked does not belong to the set of orbits of unperturbed system. In this case, one cannot simply wait until the system comes

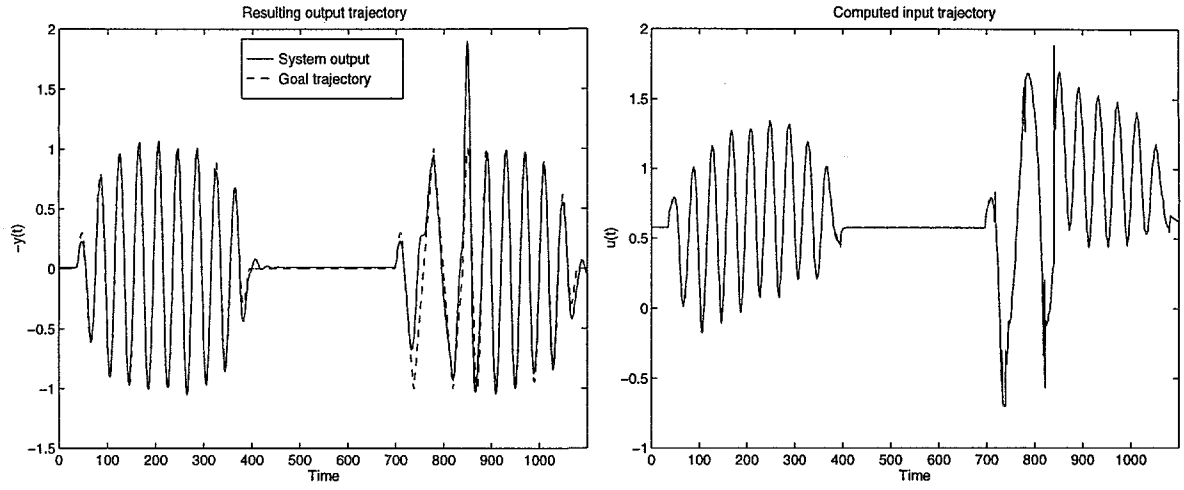

Figure 1: a.The computed input from the trajectory planning algorithm; b.A comparison of the goal trajectory and the output of the circuit when the computed input from the trajectory planning algorithm is applied.

close to the orbit of interest to initiate control, as is done in OGY method[4]. Rather one could start control at an arbitrary time and hope that the system will eventually converge to the desired orbit, or control the system such that the unperturbed system is tracked slowly towards the goal trajectory from arbitrary initial conditions.

The overall control technique consists of: (i) finding a controlled input sequence which makes the desired output a trajectory of the driven system (data based trajectory planning); (ii) analyzing the stability of the dynamical system subject to the computed input; (iii) if necessary, applying a feedback technique to stabilize the orbit of interest and/or a tracking system to drive the system from arbitrary initial conditions to the desired trajectory. We tested this method both in numerical simulations with Lorenz system and in experiments with electronic circuits. Fig. 1a shows the planned and actual voltage produced by a chaotic electronic circuit when calculated control sequence (Figure 1b) was applied to it. This example shows that trajectory planning method can accurately track signals which are non-periodic. The input signal is computed without any mathematical or identified description of the system dynamics. In addition, the output trajectory is not an existing trajectory of the chaotic attractor. This clearly demonstrates the difference between this method and other methods of chaos control based on stabilization of periodic orbits of a nonlinear system. For complete details of the algorithm and the experimental results, see [18].

SIGNAL RESTORATION VIA INVERSE NONLINEAR MODELING

Signal distortion in transmission lines and communication channels is a common problem for data communication. While propagating through a channel, the signal is distorted for a number of reasons. Most common are [20] additive or multiplicative noise, imperfections in the frequency response of the channel (dispersion), interference with other signals, multipath propagation, and nonlinearity. The last feature is especially important for us in the context of the present proposal, since we may now view the signal transmission through a communication channel as an external

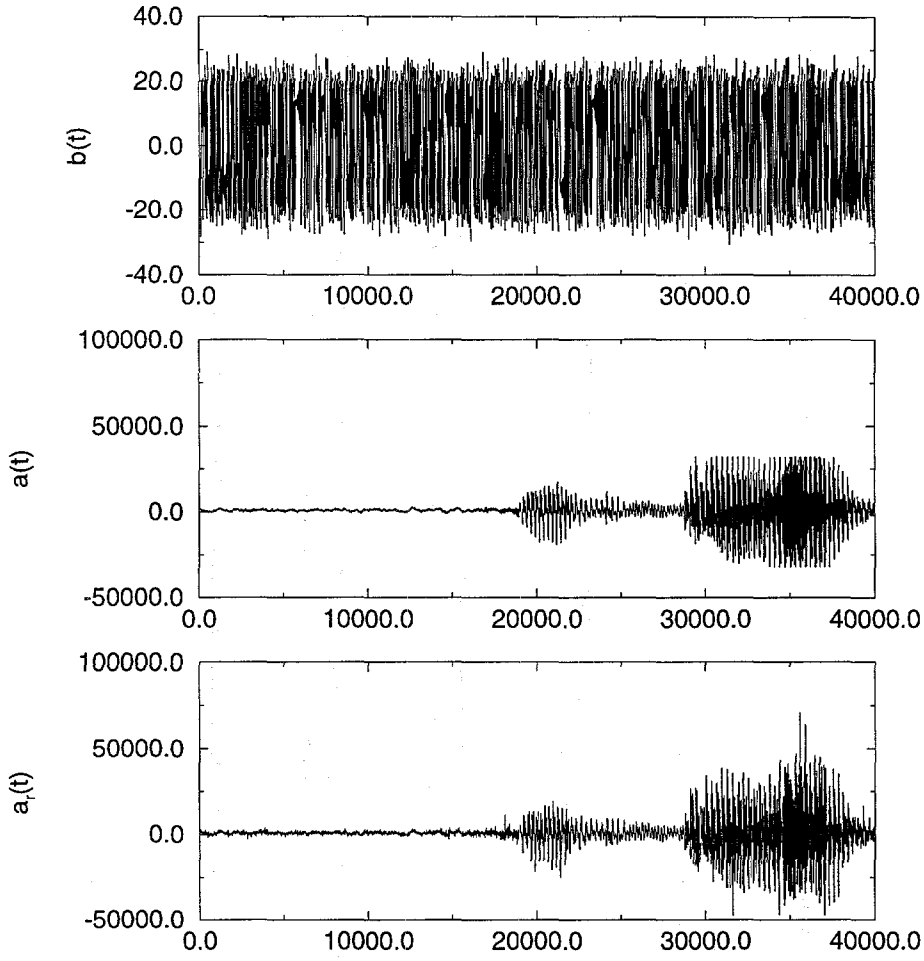

Figure 2: Human speech passed through the Lorenz system and recovered using inverse filtering. Time series of output signal (a), input signal (b), and reconstructed signal (c)

forcing of some unknown dynamical system. It turns out that a channel seen as a dynamical system with its own dynamics can add new components to the transmitted signal and therefore distort it significantly. Much effort has been made to reduce signal degradation, or if some degradation appears unavoidable, to design the transmitter/receiver as to increase robustness of the signal to distortion and to recover much of the transmitted signal. These efforts by and large ignored nonlinearity in channels in spite of the fact that there are no real linear channels at all and a linear channel is more or less a good idealization. In Section 2 we outlined how one can develop an inverse model for a process given sequences of both the input and output data. Exactly the same approach can be employed for signal processing. Using test samples of the input and output signals, one can build an inverse model and use it for the recovery of nonlinear and dispersive distortions. In the following we illustrate the potential of this method by the recovery of speech distorted beyond any recognition after passing through the chaotic Lorenz system.

We illustrate here this approach by application of the inversion technique to the signal recovery in a numerically simulated driven Lorenz system,

$$\begin{aligned} \dot{x} &= \sigma(y-x), \\ \dot{y} &= -xz + rx - y + s(t), \\ \dot{z} &= xy - bz. \end{aligned} \tag{8}$$

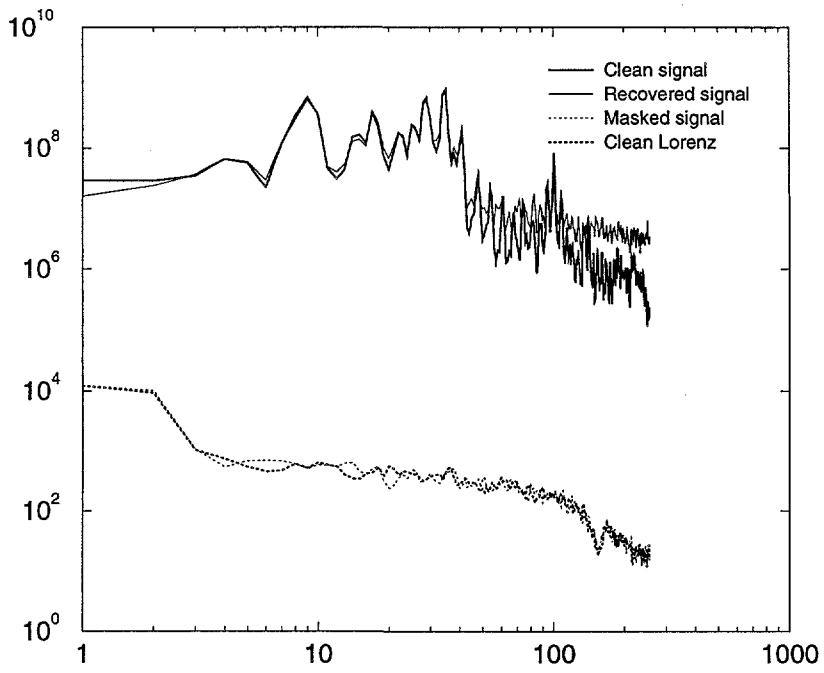

Figure 3: Power spectra of input signal, output signal, reconstructed input signal and clean signal from Lorenz system

where $r = 45.62$, $b = 4$, $\sigma = 16.0$. Here $s(t)$ plays a role of input signal, and $x(t)$ is an output signal passed through a nonlinear channel. As a learning signal we used a 3 sec segment of human speech (three words) sampled at 8kHz, i.e. about 30,000 points long. The output signal $x(t)$ is completely chaotic with no recognizable visual or audible trace of the input signal at all. Then we used as a test input a different piece of speech (even of a different person and a different language) and tried to retrieve it back from the chaotic output. We used an embedding dimension $d = 9$ and a time delay $T = 5$. In Figures 2a,b,c small pieces of output, input and recovered input test signals are shown, respectively. As one can see, a reasonably good recovery takes place, which is confirmed by a direct audio-test. Some high-frequency noise is added in(see Fig.3), however one can filter it out in a standard way. Another conclusion which one can draw from this example is related to the security of chaotic communication schemes. It shows that in some cases one can undo the masking of the signal by much stronger chaotic signal not only when the chaotic system and the particular way of mixing signal with chaos are known to the interceptor, but even without any such knowledge by using "black-box" techniques described here. This example demonstrates that simple-minded mixing of signal with chaos is susceptible to the so called "known plaintext attack"[21] when a particular message and its encrypted form are both known to the eavesdropper.

ACKNOWLEDGEMENT

This research was supported in part by the U.S. Department of Energy, grant #DE-FG03-95ER14516.

References

[1] A. ISIDORI, *Nonlinear Control Systems*, Springer-Verlag, Berlin, 3rd ed., 1995.

[2] C.E. GARCÍA, Quadratic Dynamic matrix Control of Nonlinear Processes. An Application to a Batch Reactor Process, AIChE Annual Mtg., 1984; S. de Oliveira and M. Morari, IFAC Symposium on Robust Control, Brasil, 1994.

[3] L. BIEGLER and J. RAWLINGS, Proc. of CPC-IV, South Padre Island, Texas, 1991, 543-571.

[4] E. OTT, C. GREBOGI and J.A. YORKE, Phys. Rev. Lett. **64**, 1196 (1990).

[5] H.D.I. ABARBANEL, R. BROWN, J.J. SIDOROWICH, and L.S. TSIMRING. Rev.Mod.Phys., **64**, 1331 (1993).

[6] E.R. HUNT, Phys. Rev. Lett. **67**, 1953 (1991).

[7] R. ROY, *et al*, Phys. Rev. Lett., **68**, 1259 (1992).

[8] C.A. MURPHY and M. P. KENNEDY. Proc. NDES'95, 225 (1995).

[9] A. HÜBLER, *Helv. Phys. Acta*, **62**, 343 (1989).

[10] E.A. JACKSON, *Phys. Lett. A*, **151**, 478 (1990).

[11] J.L. BREEDEN, *Phys. Lett. A*, **190**, 264 (1994).

[12] R. METTIN, A. HÜBLER, and A.SCHEELINE, *Phys. Rev. E*, **51**, 4065 (1995).

[13] M.-C. HO, J.-L. CHERN, and D.-P. WANG, *Phys. Lett. A*, **194**, 159 (1994).

[14] C.-C. CHEN, *Phys. Lett. A*, **213**, 148 (1995).

[15] P.M. CLARKSON. *Optimal and Adaptive Signal Processing*, Boca Raton: CRC Press, 1993.

[16] M. CASDAGLI and S. EUBANK (eds.), *Nonlinear Modeling and Forecasting*, Santa Fe Institute Proceedings, Addison-Wesley, 1992.

[17] H. TONG,*Nonlinear Time Series Analysis: A Dynamical Systems Approach*, Oxford University Press, 1990.

[18] C. RHODES, M. MORARI, L.S. TSIMRING, and N.F. RULKOV, Phys. Rev. E , **56**, 2398 (1997).

[19] M. MORARI and E. ZAFIRIOU, *Robust Process Control*, Prentice-Hall Inc., 1989.

[20] W.P. DAVENPORT, *Modern Data Communication*, New York: Hayden Book Co., 1971.

[21] A.J. MENEZES, P.C. van OORSCHOT, S.A. VANSTONE. *Handbook of applied cryptography*, Boca Raton : CRC Press, 1997.

SPATIO-TEMPORAL PATTERNS IN OSCILLATING MEDIA

Mikhail I. Rabinovich and Lev S. Tsimring

Institute for Nonlinear Science
University of California, San Diego
Mail Code 0402
La Jolla, California 92093-0402

ABSTRACT

Spatio-temporal dynamics of patterns in oscillating media are investigated analytically, numerically, and experimentally. We observed and explained theoretically vorticity generation in vertically vibrating layer of fluid (Faraday experiment) and in soap films. In the former case vorticity is generated near the walls and leads to stable spiral rotation in large-viscosity fluids. In the second case, vorticity is generated in the bulk of film as a result of nonlinear interaction of different wave modes in the film. We also constructed a theoretical model for pattern formation in vertically vibrated granular layer which explaines recent experiments by Umbanhowar et al.

INTRODUCTION

The theory and practice of spatio-temporal patterns in nonequilibrium media that apparently reached its pinnacle in the end of eighties, is becoming now, ten years later, again the focus of concentrated efforts of physicists, biologists and engineers. There are at least two explanations for this revival of attention to pattern formation dynamics. The first has to do with important engineering problems involving media with complex microstructure, such as granular materials, soap films and others. The second deals with the unique abilities of nonlinear nonequilibrium media and their discrete analogs to register, memorize and process the information contained in spatio-temporal patterns. Recent neurophysiological experiments demonstrated a certain universality of spatio-temporal representation of information by neural ensembles of different levels, including cortex. These studies reveal the need for developing a general approach to the analysis of spatio-temporal patterns in nonequilibrium media with complex microstructure composed of elements exhibiting nontrivial temporal dynamic. Thus, such seemingly different problems as occurrence of patterns in granular media subjected to an oscillating gravitational field and existence of stable or metastable spots of synchronization against a background of chaotic activity in a neural layer, have similar dynamic origins. These phenomena may be studied in the framework

of close models and their features can be elucidated by parallelizing the progress and experience for the companion problem.

Even homogeneous nonequilibrium media demonstrate a larger variety of "coherent structures" than previously anticipated. These are spatio-temporal patterns that are either themselves localized or that consist of domains of regular patterns connected by localized defects or interfaces. The level of coherence may be different for each system as observed in experiments, ranging from perfect structures like crystalline and quasicrystalline patterns, lattices with incommensurate periodic modulation, superlattices and to disordered patterns that have nevertheless a regular averaged spatial organization. These different "levels of order" are the result of different degrees of synchronization between the modes that form these coherent structures.

In this paper we are reviewing our last results about nonlinear dynamics of pattern formation in oscillating media. We discuss the experiments and the theory of the birth of rotating multiarmed spirals when nothing breaks the rotational symmetry in the Faraday experiment with capillary waves; we constructed a theoretical model explaining recently observed complex dynamics of vibrated layers of granular material; and investigated the coherent structures and spatio-temporal chaos in soap film undergoing periodic transverse oscillations.

FORMATION OF ROTATING SPIRALS IN THE FARADAY EXPERIMENT

Many different instabilities and nonlinear mechanisms may be responsible for formation of stable spiral patterns in nonequilibrium media[1]. In most cases, however, spiral structures have a very significant common feature. Namely, a singularity or singularities in the spiral core. Such a singularity may be either a natural medium inhomogeneity or a topological singularity of the field itself. Our consideration was restricted to isotropic media (fields) without inhomogeneities. Spirals in such media are waves.

We found multiarmed spiral waves in a Faraday experiment performed in a thin layer of viscous liquid placed in a vessel subjected to the oscillating gravity field normal to the quiescent free surface of the liquid. These objects are standing capillary waves with spiral-like fronts slowly rotating around the core. Examples of spiral structures and their formation from a target pattern *via* defect dynamics are given in Figs.1. Spirals having different topologic charges born as a result of the motion of defect towards the center of cylindrical pattern were observed. Our experiments[2] indicated that the existence of capillary spirals is sustained by the mean flow generated near the walls of the cell by rapidly damped viscous surface waves.

A theoretical description of these spiral waves was devised using a model equation for the complex order parameter ψ that takes into account the principal features of parametrically excited structures[2]:

$$\frac{\partial \psi}{\partial t} = \gamma \psi^* - \nu \psi - (1 + i\alpha)|\psi|^2 \psi + i\kappa(\nabla^2 + 1)\psi - (\mathbf{u} \cdot \nabla)\psi \qquad (1)$$

Here ψ is a complex amplitude of surface oscillations at the parametric frequency ω_0 (which is a half of the driving frequency), γ is a forcing magnitude, κ is the dispersion parameter, and $\mathbf{u}$ is the velocity of the mean flow. Linear terms in this equation can be derived from the dispersion relation for capillary waves under parametric excitation, expanded near $\omega = \omega_0$, $q = 1$. The nonlinear term cannot be derived rigorously, and has been added *ad hoc* to account for the stabilization of the parametric instability. Imaginary part of the nonlinear coefficient α describes nonlinear frequency shift (see also [3]).

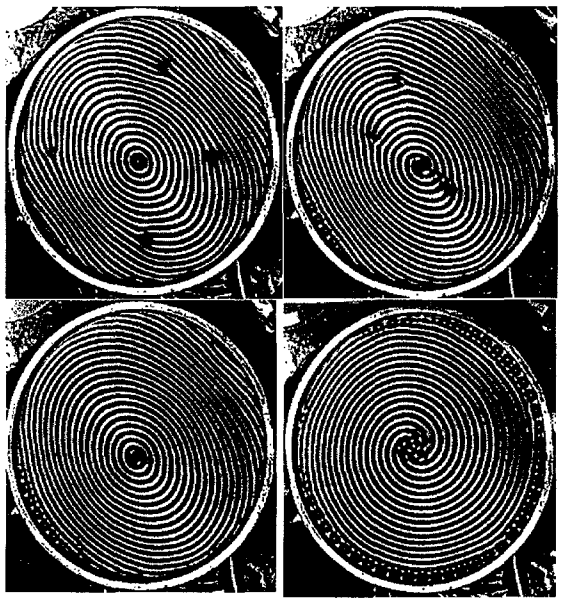

Figure 1: Series of snapshots of Faraday ripples in laboratory experiment[2]: *a* - a target with four dislocations (two positive and two negative) *b* - one dislocation is attracted to the target core, spiral is formed; *c* - all dislocations have been attracted to the center and annihilated, perfect target re-appeared; *a, b* and *c* are separated by 2.0 sec; *d* - asymptotic state of another experiment where a three-armed spiral was formed and rotated for a long time (one period of a standing wave corresponds to two white and two dark stripes on the photos due to time averaging).

The last term in the r.h.s. of Eq.(1) describes order parameter advection by the mean flow. Such mean flow was observed in experiments [2] near the walls of the cavity. This flow is caused by the momentum transfer from dissipating capillary waves at the driving frequency which are generated by oscillating side walls. This flow is directed off the walls near the surface and due to incompressibility returns back to the walls near the bottom Velocity $\mathbf{u}$ in (1) should be understood as an the average velocity over layer thickness weighted with the vertical structure of waves. Since surface waves decay towards the bottom, near-surface flow affects them stronger than near-bottom return flow and the net $\mathbf{u}$ is oriented towards the center of the cavity.

Equation (1) with periodic boundary conditions was studied numerically using pseudo-spectral split-step method with 256×256 collocation points, domain size $d = 200$ and integration time step 0.05. To simulate waves in circular cavity, we ramped linear dissipation outside the circle of radius $r_0 = 86$, i.e. $\nu = \nu_0, r < r_0$ and $\nu = \nu_0(1 + k\,(r - r_0)), r > r_0$, where k varied between 0.5 and 1.0. We assumed that the flow had radial direction and was azimuthally symmetric, $\mathbf{u} = u(r)\hat{\mathbf{r}}$. We used the following profile for flow velocity, $u(r) = u_0 \exp[\xi(r - r_0)]$. For $\gamma > \nu$ trivial state $\psi = 0$ is unstable with respect to perturbations with wavenumbers near 1. Numerical simulations show that at the nonlinear stage, these perturbations give rise to various cellular patterns, including plane waves, targets and spirals. Without mean flow term ($u_0 = 0$), these patterns remain stationary even when nonlinear coefficient in (1) is complex. Nonlinear frequency shift $\propto \alpha$ only leads to deviation of the selected wavenumber from $q = 1$. [In systems with ordinary (non-parametric) pattern-forming instabilities non-potential effects usually lead to wave propagation.] However, when the near-wall flow is introduced in (1), standing waves comprising targets and spirals begin to drift slowly toward the center. The multiarmed spirals are born due

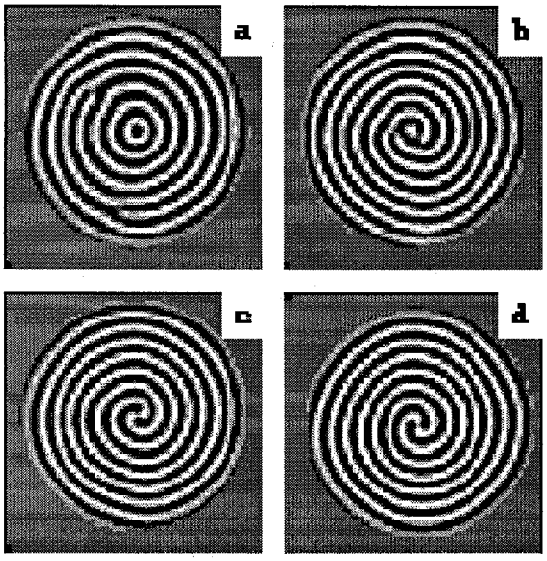

Figure 2: Snapshots of multiarmed spiral formation in numerical simulation of Eq.(1). Parameters of simulations: $\gamma = 1.0, \nu = 0.5, \alpha = 0.0, \kappa = 1.0, k_0 = 1, \xi = 0.1$. In *a*, $\xi = 0.1$, in *b*, $u_0 = 1.0$. A target with two dislocations on periphery was taken as initial condition. *a* - $t = 10$, *b* - $t = 100$;*c* - $t = 200$; *d* - $t = 300$. Spiral rotation is obvious from comparison of *c* and *d*.

to dislocation motion towards the core of the structure. The topologic charge of the spiral is equal to the sum of topologic charges of dislocations. Several snapshots illustrating the motion of dislocations are presented in Fig 2. Comparison of Figs. 1 and 2 confirms that the suggested model gives a qualitatively correct description of the phenomenon of multiarmed spiral waves of capillary ripples.

ORIGIN OF LOCALIZED PATTERNS IN VIBRATED GRANULAR LAYER

Pattern formation in a vertically vibrated layer of granular particles recently attracted much interest among physicists [4, 5, 6, 7, 8, 9, 10, 11, 12, 13, 14, 15]. We proposed a phenomenological model that describe the pattern dynamic in such oscillating media. The model consists of an equation for the order parameter ψ coupled to a conservation law for the average mass of granular material per unit area (or a local averaged thickness of the layer):

$$\partial_t \psi = \gamma \psi^* - (1 - i\omega)\psi + (1 + ib)\nabla^2 \psi - |\psi|^2 \psi - \rho\psi \quad (2)$$

$$\partial_t \rho = \alpha \nabla \cdot (\rho \nabla |\psi|^2) + \beta \nabla^2 \rho \quad (3)$$

Eq.(2) without the last term is a popular model for the parametric instability in vertically oscillating liquid layer (cf. (refmodel)). The order parameter $\psi(x, y, t)$ characterizes the complex amplitude of particle oscillations ξ at the frequency of parametric resonance $\omega = \Omega/2$. Linear terms in Eq.(2) can be derived from the dispersion relation for parametrically driven granular waves. The term $\gamma\psi^*$ provides parametric driving and leads to the excitation of standing waves. The term $|\psi|^2\psi$ accounts for the nonlinear saturation of oscillations provided in granular materials

by inelastic collisions. The last term in Eq.(2) accounts for the coupling of the order parameter to the local average density ρ. As observed experimentally [4, 5], the threshold value of the vibration amplitude γ for parametric instability scales with the mean layer thickness[4] owing to an increase of internal dissipation with increasing layer thickness.

Eq.(3) describes the conservation of the granular material where ρ is a mass of granular material per unit square averaged over the vibration period. Two different physical mechanisms contribute to the horizontal mass flux. The first term in (3) reflects the average particle drift due to the amplitude gradient of high-frequency oscillations. On average, particles try to "escape" from regions of large fluctuations, an effect analogous to the formation of so called Chladni figures. The second term describes diffusive relaxation of the inhomogeneous mass distribution.

This model exhibits a variety of stable cellular patterns including standing rolls and squares as well as localized excitations (*oscillons* and *worms*) (see Fig.3), similar to recent experimental observations [4, 5]. The underlying reason for occurrence and stability of localized oscillons in this model experiment according this model is the subcritical bifurcation of the trivial state at large α/β. The mechanism of the subcritical bifurcation is the following. The dissipation rate of the subharmonic oscillations depends on the local thickness of the layer. However, the latter is controlled by the amplitude of oscillation itself. Due to this feedback, the granular particles are expelled from the regions of large amplitude oscillations and therefore reducing the dissipation there.

We also studied the dynamics of hexagons and interfaces using our order-parameter model[9]. For high-frequency vibrations the model can be reduced to a single complex parametric Ginzburg-Landau equation. Nevertheless, this model is able to reproduce both hexagons and interfaces, as well as the transition from smooth to decorated interfaces. Furthermore, in a certain region of the parameters we were able to reduce our description to a single Swift-Hohenberg equation (SHE). Surprising result of our study is that there is a transition from smooth to unstable interfaces already within a standard Swift-Hohenberg equation at large values of the control parameter. The interface instability leads eventually to labyrinthine pattern with a preferred wavenumber. We developed the description of the labyrinths in the SHE in terms of nonlocal contour dynamics.

COHERENT STRUCTURES AND SPATIOTEMPORAL CHAOS IN SOAP FILM

The interaction of vortical and wave patterns having different spatial and temporal scales is one of the most interesting and long-standing problems in hydrodynamics. Our research is concerned with the generation of vortices in a thin horizontal soap film by transverse oscillations of that film. We performed an experimental investigation of the dynamics of structures in films stretched over circular or square boundaries undergoing periodic transverse oscillations at frequencies in the range 20-200 Hz[16, 17]. Concomitant with modes of transverse flexural oscillations, two-dimensional vortices are excited in the plane of the film. When the film was relatively thick, the flexural mode patterns sometimes oscillated chaotically as a whole in the azimuthal direction. Vortices often appear in counter-rotating pairs around the perimeter of the cell, but also emerge spontaneously in the interior. The vortices may be either large, of the order of the cavity size (see Fig.4), or small, localized at a wavelength or half-wavelength of the membrane modes (Fig.5). In the experiments a stable generation of up to ten pairs of counter-rotating vortices were observed in finite regions of forcing amplitude-frequency parameter space. We also observed spatiotemporal chaos in the soap film (see Fig.4) : at a late stage of film thinning the small-scale vortices moved irregularly through the interior a cell.

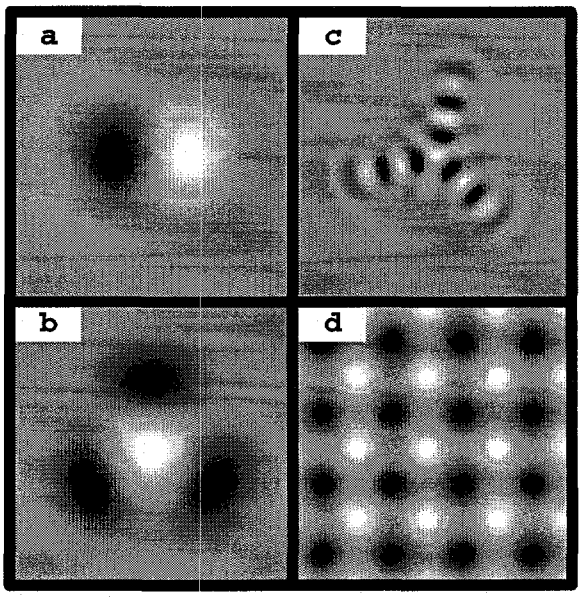

Figure 3: Gray-coded images of Reψ (black corresponds to maximum, white to minimum) from simulations of Eqs. (2-3), (a) bound state of oppositely-phased oscillons, $\alpha = \omega = 1, b = 2, \eta = 2.78, \mu = 0.527, \gamma = 1.8$, size $L = 40$; (b) Triangular bound state, same parameters; (c) worm-like structure produced by a single oscillon in the center, $\alpha = 1$, $\omega = b = 2$, $\gamma = 2.245, \eta = 4.38, \mu = 0.525$, $L = 100$; (d) square lattice, $\omega = \alpha = 1$, $\gamma = 1.84$, $\mu = 0.52$, $\eta = 2.72$, $L = 100$.

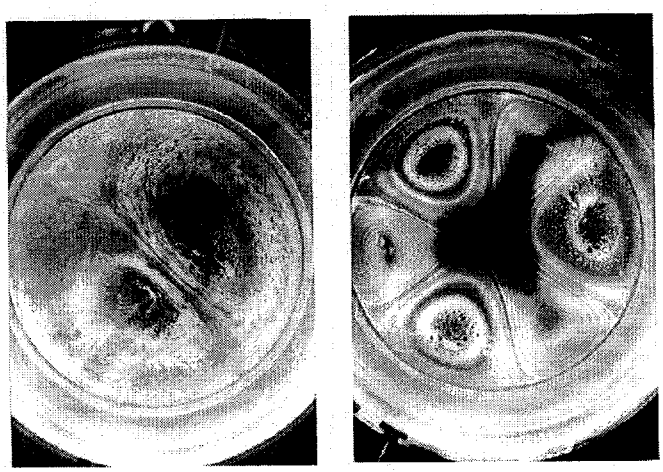

Figure 4: Large-scale counter-rotating vortex pair in the round cell at $f = 127$ Hz and $g/g' = 13.1$ at a late stage of film thinning (a); circular cell interference fringes showing vortex motion in an old film at $f = 40.4$ Hz and $g/g' = 17.1$ (b)

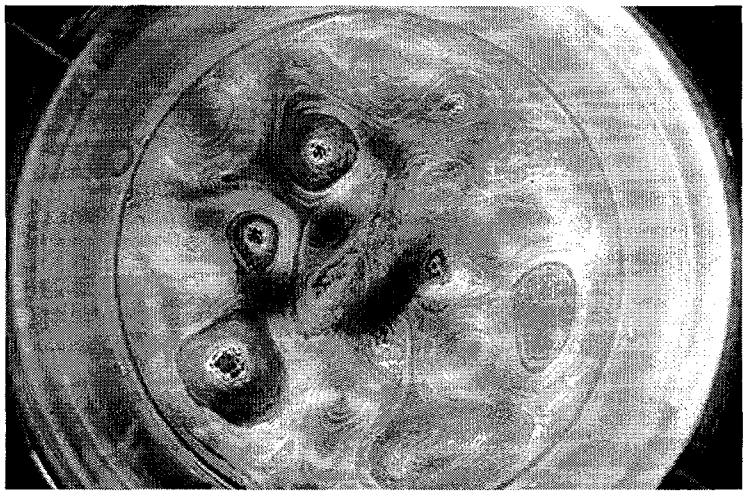

Figure 5: Snapshot of spatiotemporal chaos in the round cell at f=84 Hz, g/g'=12.9 at a late stage of film thinning

To explain the effects observed in the experiments we took into account the following tree types of waves that exist in a thin liquid film, (a) the antisymmetric hydrodynamic mode; (b) the symmetric hydrodynamic mode; and (c) the Marangoni wave mode. When flexural waves are excited, on sufficiently thin films interference patterns are observed. The symmetry of an averaged interference pattern depends on the squared amplitude of the wave field. Patterns with an even degree of symmetry were often observed, but there also exist patterns invariant to a rotation of $2\pi/3$ radian as in Fig.4,b. It is likely that a mixture of modes is necessary to produce this type of a symmetry.

We also suggested a theoretical model based on the wave-boundary interaction of excited Marangoni waves[17] that reveals a mechanism of vorticity generation in vibrating soap films. This model shows that vorticity is generated throughout the entire liquid volume by viscous diffusion, and qualitatively reproduces many steady vortex patterns observed in our experiments.

ACKNOWLEDGEMENT

This research was supported in part by the U.S. Department of Energy, grant #DE-FG03-96ER14592.

References

[1] M. CROSS and P.C. HOHENBERG, Rev. Mod. Phys., **65**, 851 (1993).

[2] S.V. KIYASHKO, L.N. KORZINOV, M.I. RABINOVICH, and L.S. TSIMRING, Phys. Rev. E, **54**, 5037 (1996).

[3] W. ZHANG and J. VIÑALS, Phys. Rev. Lett., **74**, 690 (1995).

[4] F. MELO, P. UMBANHOWAR and H.L. SWINNEY, Phys. Rev. Lett. **72**, 172 (1994); *ibid* **75**, 3838 (1995).

[5] P. UMBANHOWAR, F. MELO and H.L. SWINNEY, Nature, **382**, 793 (1996).

[6] T. H. METCALF, J. B. KNIGHT, H. M. JAEGER, Physica A **236**, 202 (1997).

[7] L.S.TSIMRING and I.ARANSON, Phys. Rev. Letters, **79**, 213 (1997).

[8] I. ARANSON and L. TSIMRING, Physica A, **249**, 103 (1998).

[9] I.ARANSON, L.S.TSIMRING, and V.VINOKUR, submitted to Phys. Rev. Letters.

[10] C. BIZON et. al, Phys. Rev. Letters, **80**, 57 (1998)

[11] S. C. VENKATARAMANI and E. OTT, preprint, 1998.

[12] D. ROTHMAN, Phys. Review E, **57** (1998).

[13] E. CERDA, F. MELO, and S. RICA, Phys. Rev. Letters, **79**, 4570 (1997).

[14] T. SHINBROT, Nature **389**, 574 (1997).

[15] J. EGGERS and H. RIECKE, patt-sol/9801004.

[16] P.D.WEIDMAN, V.O.AFENCHENKO, A.B.EZERSKY, S.V.KIYASHKO, and M.I.RABINOVICH, Phys.Fluids, **9**,S2 (1997).

[17] V.O.AFENCHENKO, A.B.EZERSKY, S.V.KIYASHKO, M.I.RABINOVICH and P.D.WEIDMAN, Phys.Fluids, **10** 390 (1998).

Synchronizing High-Dimensional Chaotic Optical Ring Dynamics

Henry D. I. Abarbanel* and Matthew B. Kennel†

Institute for Nonlinear Science, University of California, San Diego, La Jolla, California 92093-0402

(Received 18 September 1997)

We study chaotic ring laser systems as possible elements in a communications system. To be useful it must be possible to synchronize the transmitter and receiver lasers. We show that chaotic ring lasers can be synchronized using direct light injection from one laser into the optical cavity of the second. This synchronization occurs even when both lasers are quite high dimensional and each possesses many positive Lyapunov exponents. When the lasers are synchronized, the transmitted light can be modulated with information bearing signals and the message accurately recovered at the receiver. [S0031-9007(98)05715-9]

PACS numbers: 89.70.+c, 05.45.+b, 42.55.–f

The use of erbium doped ring lasers in communications devices [1] led us to inquire whether such lasers could serve as the basis for optical communications while operating in a chaotic regime. Our work focuses on a simplified prototype of the actual erbium ring laser. The delay differential equations of our model arise by integrating the partial differential equations for the electric field in the ring, so the source of high-dimensional dynamics is identified physically. We ask whether such optical systems can synchronize and support modulation and demodulation of information bearing messages. Applications aside, we demonstrate synchronization of high-dimensional dynamical systems with many positive Lyapunov exponents. Our ring lasers operate in a regime where the dimension ≥ 20, using physically natural coupling to synchronize. The only high-dimensional systems previously known to synchronize were constructed of cascaded low-dimensional subsystems which successively synchronize [2].

There have been earlier discussions of synchronization of chaotic lasers [3], also previous modeling of erbium ring lasers using delay differential equations [4]. Reference [5] discusses communicating using chaotic lasers, but the method is quite different from ours. Our method is not restricted to small amplitude messages, and in [5] output from the transmitter is modulated. We modulate the message signal into the transmitter dynamics then stability properties of the receiver assures accurate message recovery. Recent results from VanWiggeren and Roy [6] experimentally confirm many of the effects discussed here. This includes high-dimensional dynamics and the ability to modulate and demodulate messages using the methods suggested here.

To augment the numerical evidence for synchronization, we analyze the system's largest conditional Lyapunov exponent (CLE) [7]. This linear criterion is useful and powerful as long as unstable sets are not close to the synchronization manifold. The boundary determined by direct simulation is near that predicted by the exponents. Also, the lasers synchronize for a broad range of coupling parameters, improving the chance of success for a practical realization.

The literature discusses using chaotic communications for secure or encrypted signaling. We do not address this issue. There is a distinction between such communication as a means of using channel capacity and any additional potential for security. Wide-band signaling in optical systems is interesting, independent of whether the methods are cryptographically secure. Some strategies for secure communications based on low-dimensional dynamics appear susceptible to algorithmic time-series attacks [8]. Short also argues that systems with many positive Lyapunov exponents, such as our ring laser, might resist these schemes. We have not investigated our method cryptographically.

We study a "laser" which has no polarization (important in the erbium system), no imperfect passive medium, such as an optical fiber, making up the ring, and simplified atomic physics of the active medium. Power comes from externally injected light at a frequency ω_I, possibly offset from the optical frequency ω_0 of the lasing line, and through pumping of population inversion. The basic model was introduced by Ikeda some years ago [9], thus we call the system the Ikeda Ring Laser (IRL).

Our model IRL consists of four mirrors with finite reflectivity arranged at the corners of a square. (See Fig. 1). Light with electric field $E_I e^{i(\omega_I - \omega_0)t}$ (in the coordinate system rotating at ω_0) enters the ring via the upper left mirror and passes through an idealized two-level atomic system. On departing the active medium, the light reflects off four mirrors with net reflectivity B and reenters the active medium. The external injection and external pump add power, and $B < 1$ attenuates it. After a straightforward derivation we arrive at a discrete time map for the complex electric field amplitude $\zeta(t)$ at a fixed spatial location coupled to a differential equation for the spatially averaged population inversion $w(t)$:

$$\zeta(t + \tau_R) = E_I e^{i(\omega_I - \omega_0)t} + B e^{i\kappa} \zeta(t) e^{(\beta + i\alpha)w(t)}$$

$$\frac{dw(t)}{dt} = Q - 2\gamma\{w(t) + 1 + |\zeta(t)|^2 (e^{Gw(t)} - 1)/G\},$$

with τ_R the propagation time around the ring. β and α are nonlinear gain coefficients and γ the atomic decay

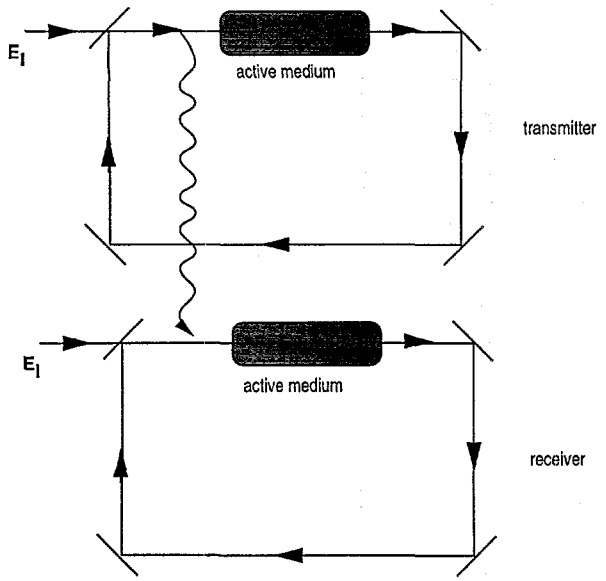

FIG. 1. Schematic of unidirectionally coupled Ikeda ring laser systems.

rate related to transitions between lasing photons and an external loss bath, G is another gain-related parameter. κ is the phase acquired by a plane wave traversing the ring. Measuring time in units of τ_R we see that only the dimensionless quantity $\gamma\tau_R$ is important in the dynamics. Physically we cannot vary γ, but we can change τ_R by varying the length of the cavity. Our time scale chooses $\tau_R = 1$. Physically accessible time scale variations are expressed as changes in γ.

This is a delay differential system. Such systems may exhibit both low-dimensional and very high-dimensional behavior: complexity generally increases with the delay time. We integrated with a simple fixed time step, δt being chosen so that $\gamma\delta t = 10^{-3}$. The value for $w(t)$ is advanced one δt using a standard fifth order Adams predictor-corrector scheme, as dw/dt explicitly depends only on $w(t)$ and $|\zeta(t)|^2$. At t the value for $\zeta(t+1)$ is computed from the map and saved for future use.

We chose parameter values corresponding to the standard "Ikeda map," often used as an example of a two degrees of freedom chaotic system [10]. We recover the Ikeda map in the limit $\gamma \to \infty$, $G \to 0$, $\omega_I = \omega_0$, and $dw/dt = 0$,

$$\zeta(t+1) = E_I e^{i(\omega_I - \omega_0)t} + Be^{i\kappa} e^{(-\beta - i\alpha)/(1+|\zeta(t)|^2)}\zeta(t).$$

Identifying our parameters with canonical values [10] yields $E_I = 1$, $B = 0.9$, $\kappa = 0.4$, $\beta = 0, \alpha = 6$, and $\omega_I = \omega_0$. From a related experiment [4] we estimate $G = 0.01$, and chose $\gamma = 1$ and $Q = 0$ for the calculations reported here. When $\omega_I \neq \omega_0$, the dynamical structure can be more complex than we report here, and similarly when $Q > 0$. We will report on these situations in a larger report of this work. In the matters of synchronization and modulation for information transmission, though, there is no change from the behavior reported in this short note. We have investigated a wide range of values of γ, and for γ larger than order 0.5, the dynamics are chaotic, and the essential features are the same as reported here for $\gamma = 1$. The time-asymptotic dynamics has sufficiently high dimension that the standard time-series analysis tools used for low-dimensional chaos, such as correlation dimension, false nearest neighbors, etc. [10], fail to give useful results. Specifically, false nearest neighbors calculations did not show low dimensionality with any embedding dimension up to 12, beyond which we fail to have confidence in the algorithm.

We can, however, evaluate the entire spectrum of Lyapunov exponents directly from the equations and use them to estimate the dimension [11]. Specifically, we find the exponents of the predictor-corrector integration algorithm. This is a map taking the state vector $\mathbf{S}(j)$ of the system to the state one time step δt later: $\mathbf{S}(j) \longrightarrow \mathbf{S}(j+1) = M[\mathbf{S}(j)]$. $\mathbf{S}(j)$ is large: $2N + 5$ components for a time interval of $N = \tau_R/(\delta t)$ parts. $2N$ are from the saved values of ζ, one for $w(t)$, and four for recent derivatives of w used in the integration. We find the Jacobian $DM(\mathbf{S}[j])$ of the map along the trajectory of the system simultaneously generated by the integration algorithm. The Jacobian is too large to represent efficiently as an explicit matrix in the computation, but its sparseness allows us to write a subroutine to multiply an arbitrary vector by $DM(\mathbf{S}[j])$, and thus, any matrix, by operating on columns independently.

The Lyapunov exponents are evaluated by a variant of the standard recursive QR algorithm [10]. Given an initial random orthogonal matrix $\mathbf{Q}[0]$ with $2N + 5$ rows and N_L columns (where $N_L \leq 2N + 5$ is the number of Lyapunov exponents to evaluate): successively multiply by $DM(\mathbf{S}[1]), DM(\mathbf{S}[2]), \ldots, DM(\mathbf{S}[k])$ up to a normalization interval k, perform the explicit QR decomposition, resulting in $\mathbf{Q}[1]$ and $\mathbf{R}[1]$. The LAPACK subroutine library offers standard routines to perform the QR decomposition for nonsquare matrices, needed since typically $N_L \ll 2N + 5$. Accumulate the sum of the logarithm of the N_L diagonal elements of $\mathbf{R}$, and repeat starting with $\mathbf{Q}[1]$. In the asymptotic time limit, the averaged logarithm of $\mathbf{R}$'s diagonal converges to the N_L largest Lyapunov exponents. This requires QR decompositions of a large full-rank matrix, but it is not required frequently. The calculation time is dominated by the evaluation of $DM(\mathbf{S}[k])$. The overall algorithm is a numerically superior version of the Gram-Schmidt orthogonalization used by Farmer [12]. From the exponents λ_i, we choose K such that $\sum_{i=1}^{K} \lambda_i > 0$ and $\sum_{i=1}^{K+1} \lambda_i < 0$, and form the Lyapunov dimension [11] $D_L = K + \sum_{i=1}^{K} \lambda_i/|\lambda_{K+1}|$. The main free parameter governing the dimension is γ: for $\gamma \geq 0.5$, D_L increases nearly linearly with γ. At $\gamma = 1$, the Lyapunov dimension is about 22.

We investigate the synchronization of two $\gamma = 1$ IRLs. The coupling is unidirectional: the unaltered output of

a transmitter feeds into a receiver; this is depicted in Fig. 1. After investigating a variety of coupling schemes we settled on the following:

$$\zeta_1(t+1) = f[\zeta_1(t), w_1(t)],$$
$$dw_1(t)/dt = g[w_1(t), |\zeta_1(t)|^2],$$
$$\zeta_{\mathrm{Comb}}(t) = (1-c)\zeta_2(t) + c\zeta_1(t),$$
$$\zeta_2(t+1) = f[\zeta_{\mathrm{Comb}}(t), w_2(t)],$$
$$dw_2(t)/dt = g[w_2(t), |\zeta_{\mathrm{Comb}}(t)|^2].$$

The free running transmitter has state variables $\zeta_1(t)$ and $w_1(t)$. Into the receiver we inject the transmitted electric field $\zeta_1(t)$, scaled by c, along with a fraction $(1-c)$ of $\zeta_2(t)$. When $\zeta_1(t) = \zeta_2(t)$ the equations are precisely the same. Ordinary synchronization is thus possible, and generalized synchronization [13] is not required. It is not physically possible to couple the population inversion dynamics, so no information about $w_1(t)$ is transmitted to the receiver. When c was larger than ≈ 0.3, synchronization was observed for a wide range of parameter values.

We computed the mean time to achieve synchronization over an ensemble of initial conditions. Two IRLs were run with $c = 0$ for a sufficiently long time for each to reach asymptotic behavior. The coupling was then turned on. We evaluated the time t_s past which $|\zeta_2(t) - \zeta(t)|$ remained less than some small value for all t up to some large T. If the systems do not synchronize, the average of t_s over the ensemble, $\langle t_s \rangle$, would be T. Synchronization is exhibited by $\langle t_s \rangle \ll T$. Simultaneously, we computed the CLEs of $[\zeta_2(t), w_2(t)]$, evaluated along the synchronization manifold, $\zeta_2(t) = \zeta_1(t), w_2(t) = w_1(t)$, with $\zeta_1(t)$ and $w_1(t)$ treated as given in the evaluation of the Jacobian. The results of our computations are shown in Fig. 2(a).

In Fig. 2(b) we plot the largest CLE and the average time to synchronization as a function of c. A largest CLE below zero is necessary, but not sufficient, to guarantee synchronization [14]. In our system, the difference between them was small: the largest CLE becoming negative is a good predictor of the boundary of synchronization. Though not shown, $w_1(t)$ and $w_2(t)$ also fully synchronized: $|w_1(t) - w_2(t)|$ converged to zero.

With $c = 1$ the receiver is an "open loop" demodulator of any signal modulated onto $\zeta_1(t)$. In this special case, we may prove that $|w_1(t) - w_2(t)|$ approaches zero faster than $e^{-2\gamma t}$, and when this occurs, $\zeta_1(t) \longrightarrow \zeta_2(t)$ too. Write the equations for two coupled IRLs with $c = 1$,

$$\zeta_1(t+1) = f[\zeta_1(t) + m(t), w_1(t)],$$
$$dw_1(t)/dt = g[w_1(t), |\zeta_1(t) + m(t)|^2],$$
$$\zeta_2(t+1) = f[\zeta_1(t) + m(t), w_2(t)],$$
$$dw_2(t)/dt = g[w_2(t), |\zeta_1(t) + m(t)|^2],$$

where $m(t)$ is added to the electric field amplitude of the first laser. The output $\zeta_1(t)$ is nonlinearly dependent on

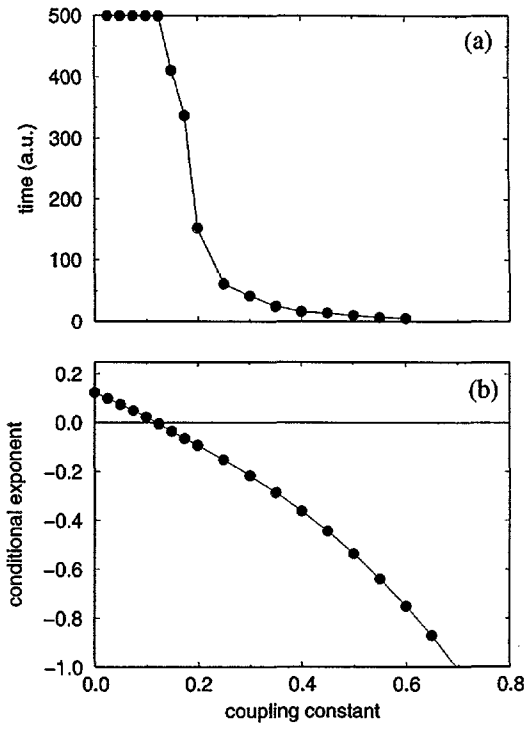

FIG. 2. (a) Mean time to synchronization and (b) largest CLE for $\gamma = 1.0$. The average time to synchronization starts to sharply decrease from the maximum run time (which implies no synchronization) at approximately the same coupling where the largest CLE becomes negative.

$m(t)$. Subtract the differential equations,

$$\frac{d[w_1 - w_2]}{dt} = -2\gamma\{w_1 - w_2 + |\zeta_1 + m|^2 e^{Gw_2}(e^{G[w_1 - w_2]} - 1)/G\}.$$

Since $e^A - 1 \geq A$ and $e^A \geq 0$ for real A,

$$\frac{d[w_1 - w_2]}{dt} \leq -2\gamma[w_1 - w_2]\{1 + |\zeta_1 + m|^2 e^{Gw_2}\},$$

showing that $|w_1(t) - w_2(t)| \to 0$ faster than $e^{-2\gamma t}$. We found numerically that the size of the electric field is large enough that even when γ is quite small, as in the erbium case, the product $\gamma|\zeta_1(t) + m(t)|^2$ remains order unity or larger. This means that the communications method suggested by us will be robust against noise contamination which bumps the system off the synchronization manifold. Similar reasoning shows the maps for $\zeta_1(t)$ and $\zeta_2(t)$ also converge: $|\zeta_1(t) - \zeta_2(t)| \to 0$. This synchronization is independent of the external pumping and the pumping rate Q, so the application of this result to the equations for the erbium ring laser is direct.

The second laser receives $\zeta_1(t) + m(t)$ and produces $\zeta_2(t) = \zeta_1(t)$ in its optical cavity. This allows us to recover $m(t)$ from the difference between ζ_2 and the transmitted signal. The basic idea works for any invertible

combination of ζ_1 and $m(t)$. In a real connection between lasers the properties of the optical fiber channel must be considered, but here we have taken it as a perfectly transmitting, lossless, dispersion free medium. We implemented this idea using a sample of speech from one of the authors. In Fig. 3 we show the message (upper panel), the actual transmitted $\mathrm{Re}[\zeta_1(t)]$ (central panel), and the recovered message (lower panel) for both perfect parameter matching (solid line) and a 1% difference in γ between transmitter and receiver (dashed line). Even with parameter mismatch, fidelity is good. We have observed successful recovery of messages using significantly smaller c using the obvious generalization of the modulation method to closed loops, starting with $c \geq 0.3$. Also using binary messages of ± 1 and a suitable digital decision rule, we have found bit error rates $\leq 10^{-5}$ even with mismatches in γ of as much as 50%.

In summary, we have developed a theoretical model for an "Ikeda ring laser" which is an unpolarized representation of the essential dynamics in an erbium-doped fiber ring laser. We have successfully synchronized two such systems described by delay-differential equations, even in the deeply chaotic regime, using an experimentally accessible coupling scheme. This work is a prelude to investigating high bandwidth information transmission utilizing chaos in coupled ring-laser systems. It also confirms that synchronization and information transmission using high-dimensional optical chaos is mathematically feasible. Finally, we note again that VanWiggeren and Roy [6] have experimentally verified the essentials of our methods for synchronization of and communication with chaotic ring lasers.

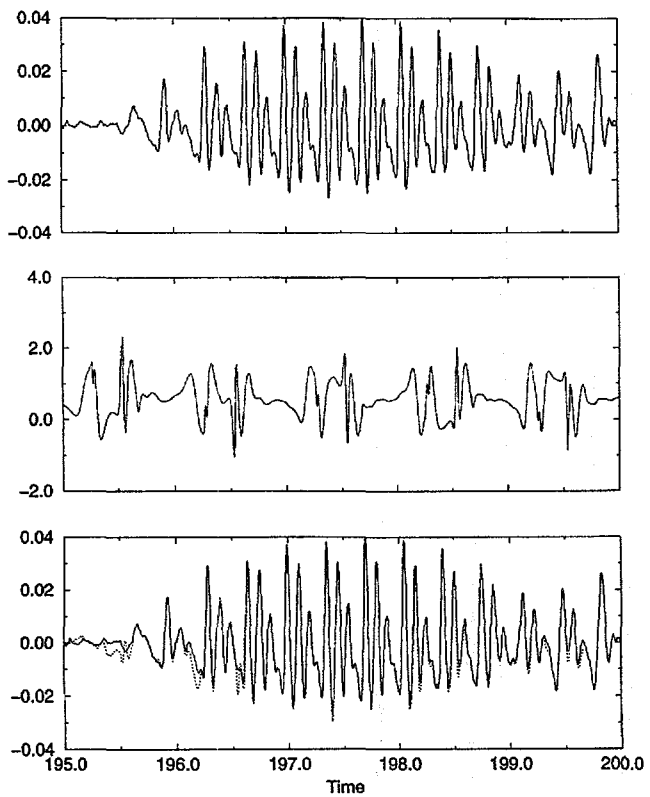

FIG. 3. A segment of speech (upper), $\mathrm{Re}[\zeta(t)]$ as modulated by the message and sent from transmitter to receiver (middle), the recovered message (lower). In the lower panels the solid line is for exact parameter match between transmitter and receiver; the dashed line results when γ in the receiver is 1% larger than γ in the transmitter.

This work was part of a joint UCSD/Georgia Tech/Cornell effort, and we are grateful to Steve Strogatz and Raj Roy and others in that program for detailed discussion of the issues here. This work was supported by the U.S. Department of Energy and the National Science Foundation.

*Department of Physics and Marine Physical Laboratory, Scripps Institution of Oceanography.
Electronic address: hdia@hamilton.ucsd.edu
†Electronic address: kennel@lyapunov.ucsd.edu

[1] R.J. Mears, L. Reekie, I.M. Jauncey, and D.N. Payne, Electron. Lett. **23**, 1026–1027 (1987); H. Takara, S. Kawanishi, M. Saruwatari, and K. Noguchi, Electron. Lett. **28**, 2095–2096 (1992); Th. Pfeiffer and G. Veith, Electron. Lett. **29**, 1849–1850 (1993).

[2] U. Parlitz and L. Kocarev, Int. J. Bifurcation Chaos **2**, 407–413 (1997).

[3] R. Roy and K.S. Thornburg, Jr., Phys. Rev. Lett. **72**, 2009–2012 (1994); T. Sugawara *et al.*, Phys. Rev. Lett. **72**, 3502–3505 (1994).

[4] Q.L. Williams and R. Roy, Opt. Lett. **21**, 1478–1480 (1996); Q.L. Williams, J. Garcia-Ojalvo, and R. Roy, Phys. Rev. A **55**, 2376–2386 (1997); J. Garcia-Ojalvo and R. Roy, Phys. Lett. A **229**, 362–366 (1997).

[5] C.R. Mirasso, P. Colet, and P. Garcia-Fernandez, IEEE Photonics Technol. Lett. **8**, 299–301 (1996); P. Colet and R. Roy, Opt. Lett. **19**, 2056–2058 (1994).

[6] G.D. VanWiggeren and R. Roy, "Communication with Chaotic Lasers" (to be published).

[7] L.M. Pecora and T.L. Carroll, Phys. Rev. Lett. **64**, 821–824 (1990).

[8] K.M. Short, Int. J. Bifurcation Chaos **6**, 367–375 (1996); K.M. Short, Int. J. Bifurcation Chaos **4**, 959–977 (1994).

[9] K. Ikeda, Opt. Commun. **30**, 257–261 (1979); K. Ikeda and H. Daido, Phys. Rev. Lett. **45**, 709–712 (1980).

[10] H.D.I. Abarbanel, *The Analysis of Observed Chaotic Data* (Springer, NY, 1996).

[11] J.L. Kaplan and J.A. Yorke, Lect. Notes Math. **730**, 228 (1979).

[12] J.D. Farmer, Physica (Amsterdam) **4D**, 366 (1982).

[13] H.D.I. Abarbanel, N.F. Rul'kov, and M.M. Sushchik, Phys. Rev. E **53**, 4528–4535 (1996); N.F. Rulkov, M.M. Sushchik, L.S. Tsimring, and H.D.I. Abarbanel, Phys. Rev. E **51**, 980–994 (1995).

[14] P. Ashwin J. Buescu, and I. Stewart, Phys. Lett. A **193**, 126–139 (1994); P. Ashwin, J. Buescu, and I. Stewart, Nonlinearity **9**, 703–737 (1996); H.D.I. Abarbanel, N.F. Rulkov, and M.M. Sushchik, IEEE Trans. Circuits Syst. I, Fundam. Theory Appl. **44**, 867–873 (1997).

Analysis of glycolysis metabolites by capillary zone electrophoresis with indirect UV detection

Peidong Shen,[a] David Hauri,[a] John Ross,[a] and Peter J. Oefner[b]

[a]*Department of Chemistry, Stanford University, CA, U.S.A.*
[b]*Department of Biochemistry, Stanford University, CA, U.S.A.*

Correspondence: *Dr. John Ross, Department of Chemistry, Stanford University, Stanford, CA 94305-5080, U.S.A.*

Abstract

The glycolysis metabolites glucose 6-phosphate (G6-P), fructose 6-phosphate (F6-P), fructose 1,6-bisphosphate (F1,6-BP), fructose 2,6-bisphosphate (F2,6-BP), glyceraldehyde phosphate (GAP), dihydroxyacetone phosphate (DHAP), phosphoenolpyruvate (PEP), pyruvate, and lactate were analyzed by capillary zone electrophoresis (CZE) with indirect UV detection. The chromophores phthalic acid, sorbic acid, and 4-hydroxybenzoic acid were studied as background electrolytes. Both detection sensitivity and resolution were found to depend on the pH and the concentration of the carrier electrolyte. Optimum separation and detection of the phosphate compounds were accomplished upon reversal of electroendosmotic flow (EOF) with OFM™ Anion-BT (Waters Corp., Milford, MA) at a concentration of 4–6 m*M* 4-hydroxybenzoic acid, pH 11.6–12.0, with the detection wavelength set at 280 nm. The highly alkaline pH allowed the successful separation of the isomers F6-P and G6-P, as well as F1,6-BP and F2,6-BP, respectively. The effect of sample ionic strength on the detection limits of G6-P, F6-P, F1,6-BP, and F2,6-BP was also investigated: These limits ranged from 1 to 3 μ*M* in both low- and high-ionic-strength samples. However, high Mg^{2+} concentrations in the sample led to a progressive loss of resolution between F1,6-BP and F2,6-BP, unless the inlet reservoir was replenished with fresh electrolyte after every injection. Linearity of detection was observed over one to two orders of magnitude.

Glycolysis plays a key role in the generation of metabolic energy, providing a significant portion of the energy utilized by most organisms. The concentrations of glycolysis intermediary metabolites and regulators, such as G6-P, F6-P, F1,6-BP, F2,6-BP, GAP, DHAP, PEP, pyruvate, and lactate, have usually been determined by enzymatic assays.[1–6] The metabolites react either directly or indirectly with NADH (nicotinamide adenine dinucleotide—reduced form) or NAD^+ (nicotinamide adenine dinucleotide—oxidized form) in the presence of enzymes, with the absorbance change of NADH being a function of the concentration of the metabolite. These methods, however, cannot measure simultaneously all the metabolites present in a single tube. Therefore, their determination becomes a time-consuming task.

CZE with indirect UV detection has been successfully applied to the separation and quantification of many small inorganic and organic anions.[7–17] With reversed EOF, separation of these anions was achieved within minutes. Based thereon, the present study reports the simultaneous analysis of the glycolysis metabolites G6-P, F6-P, F1,6-BP, F2,6-BP, DHAP, GAP, PEP, pyruvate, and lactate, as well as inorganic phosphate. The chromophores phthalic acid, sorbic acid, and 4-hydroxybenzoic acid were evaluated as carrier electrolytes for indirect UV detection. Running conditions such as the pH and the concentration of the carrier electrolyte were optimized to achieve maximum resolution and sensitivity. Finally, the effects of high sample ionic strength and Mg^{2+} ion concentration on the analysis of the metabolites were investigated.

Experimental

Instrumentation

Experiments were performed either on an HP ^{3D}CE system (Hewlett-Packard Co., Wilmington, DE, U.S.A.) with the built-in photodiode-array detector set at wavelengths of 195, 254, and 280 nm, or on a P/ACE 5510 (Beckman Instruments, Fullerton, CA, U.S.A.) equipped with either a filter or a photodiode-array detector set at 254 and 280 nm, respectively. A 48-cm fused-silica capillary (40-cm effective length) with an internal diameter of 50 μm (320-μm o.d.) was used on both instruments in combination with diode-array de-

Indexing terms

Capillary zone electrophoresis, indirect UV detection, glycolysis, phosphate sugars, organic acids

Abbreviations

G6-P, glucose 6-phosphate; F6-P, fructose 6-phosphate; F1,6-BP, fructose 1,6-bisphosphate; F2,6-BP, fructose 2,6-bisphosphate; GAP, glyceraldehyde phosphate; DHAP, dihydroxyacetone phosphate; PEP, phosphoenolpyruvate; CZE, capillary zone electrophoresis; EOF, electroendosmotic flow; HEPES, 4-(2-hydroxyethyl)-1-piperazine-ethanesulfonic acid; DTT, dithiothreitol; ATP, adenosine triphosphate; ADP, adenosine diphosphate; AMP, adenosine monophosphate

tection; a 117-cm fused-silica capillary (110-cm effective length) with an internal diameter of 75 μm (320-μm o.d.) was used on the P/ACE 5510 equipped with the UV filter detector. Signals obtained on the HP ^{3D}CE system were collected and processed on an HP Vectra XM2 4/100i PC (Hewlett-Packard Co.) using ^{3D}CE ChemStation software. On the P/ACE 5510 system, signals were processed using System Gold software (Beckman Instruments). The capillary temperature was kept constant at 20 ± 0.1 °C. The applied voltage ranged from 13 to 20 kV, with the cathode being at the inlet end and the anode at the detector end of the capillary. Samples were injected by applying either a negative pressure of 0.75 psi for 5 sec on the HP ^{3D}CE system or a positive pressure of 0.5 psi for 5–50 sec on the P/ACE 5510.

A model 805 MP pH meter (Fisher Scientific, Pittsburgh, PA, U.S.A.) and a model 520A pH meter (ATI Orion Laboratory Products Group, Boston, MA, U.S.A.), both equipped with a combined electrode, were used to measure the pH of the electrolytes.

Chemicals

The EOF modifier Anion-BT was obtained from Waters. All other chemicals were purchased either from Sigma (St. Louis, MO, U.S.A.) or Mallinckrodt (Paris, KY, U.S.A.).

Running electrolyte solutions with final concentrations of 2–7 m*M* of 4-hydroxybenzoic acid, phthalic acid, and sorbic acid, respectively, were prepared in deionized water. The pH was adjusted with either 0.20 *M* or 1.0 *M* NaOH. Amounts of NaOH added were recorded and the pH of each solution was measured. OFM Anion-BT was added at a ratio of 1 to 40. Samples with low ionic strength were prepared by dissolving the metabolites in 18-MΩ deionized Millipore water to yield final concentrations of 5–400 μ*M*. Samples with high ionic strength were prepared by dissolving the metabolites in an enzyme assay buffer that contained 50 m*M* 4-(2-hydroxyethyl)-1-piperazine-ethanesulfonic acid (HEPES), pH 7.2; 50 m*M* KCl; 5.0 m*M* $MgCl_2$; 1.0 m*M* dithiothreitol (DTT); 1.0 m*M* $MgHPO_4$; 3.0 m*M* adenosine triphosphate (ATP); and 0.6 m*M* adenosine diphosphate (ADP). All sample solutions were prepared freshly before each experiment.

Procedures

All running electrolyte solutions were filtered through a 0.45-μm filter (Nalgene, Rochester, NY, U.S.A.) prior to use. New fused-silica capillaries were flushed successively with 1 *M* NaOH for 1 hr, 0.01 *M* NaOH for 30 min, and running electrolyte for 40 min. Each day prior to use, the capillary was rinsed with running buffer for 40 min at 40 °C. Between runs, the capillary was washed with running buffer for 2 min. In some instances, the running electrolyte was replenished before each run.

Results and discussion

Selection of the background chromophores

All the metabolites investigated in this study, with the exception of ATP, ADP, and adenosine monophosphate (AMP), lack UV absorbance; hence, an indirect detection method was chosen for their measurement, using a highly UV absorbing chromophoric ion as the background electrolyte. There are two major criteria in selecting an appropriate chromophoric ion. First, the mobility of the chromophoric ion should match the mobilities of the sample ions; otherwise, asymmetrical peaks result. Second, the chromophoric ion should have a high molar absorptivity, while sample ions should have low molar absorptivities at the chosen detection wavelength, so that there is a large decrease in absorbance when the chromophoric ion is displaced by a sample ion. Phthalate, 4-hydroxybenzoate, and sorbate were chosen for the present study as chromophoric ions. Sorbate with a molar absorption coefficient of 2.8×10^5 M^{-1} cm^{-1} at 254 nm matches the electrophoretic mobilities of F6-P and G6-P at pH 5–7. In this pH range, both F6-P and G6-P (pK_{a2} = 6.2) exhibit low electrophoretic mobilities because of a low charge-to-mass ratio. But neither G6-P and F6-P nor F1,6-BP and F2,6-BP could be separated at this pH. However, at high pH (pH >11), these two pairs of isomers could be resolved successfully. This is due to the difference in dissociation of the sugar hydroxyl groups at high pH (the pK_a of fructose is 12). Above pH 11, however, the electrophoretic mobility of sorbate no longer matches those of the sugar phosphates. On the other hand, 4-hydroxybenzoate (pK_{a2} = 9.2) becomes a moderately mobile divalent anion through ionization of the hydroxyl group. The mobilities of both 4-hydroxybenzoate and phthalate match the mobilities of the investigated phosphorylated compounds above pH 11. *Figure 1* shows the spectra of sorbate, phthalate, and 4-hydroxybenzoate over a wavelength range of 190–320 nm. At pH 7.0, the spectrum of 4-hydroxybenzoate contains two maxima: one at 195 nm and another one at 250 nm. At pH 11.5, the latter maximum shifts to 280 nm. This shift is due to the rearrangement of the electrons on the benzene ring of 4-hydroxybenzoate after ionization of the hydroxyl group. Phthalate and sorbate, on the other hand, have only one maximum each at 195 and 254 nm, respectively, which is not affected by changes in pH. *Table 1* shows the concentration detection limits (defined as 3× noise in μ*M*) of F2,6-BP, F1,6-BP, F6-P, and G6-P, using either 5 m*M* 4-hydroxybenzoate as running electrolyte at wavelengths 195, 254, and 280 nm, respectively, or 5 m*M* phthalate at wavelengths 195 and 254 nm, respectively. Ultimately, 4-hydroxybenzoate was chosen for all subsequent experiments as background electrolyte with the detection wavelength set at 280 nm, as it yielded the lowest detection limits for the analytes of interest.

Effect of 4-hydroxybenzoate concentration on detection sensitivity and resolution

The authors have chosen 4-hydroxybenzoate as the carrier electrolyte because it matches both the electrophoretic mobilities of the investigated metabolites

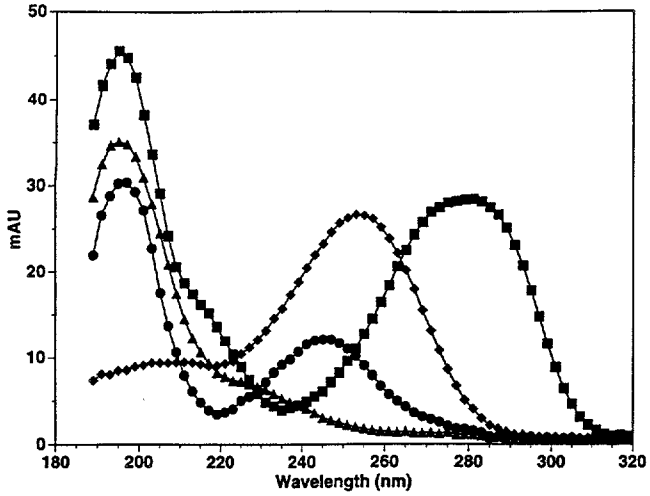

Figure 1 *Spectra of sorbate (diamond), phthalate (triangle), and 4-hydroxybenzoate at pH 7 (dot) and 11.5 (square), obtained by plotting CE signal (mAU) versus wavelength. Electrolyte: 20 mM phosphate, 0.5 mM OFM Anion-BT, pH 7 and 11.5; instrument: HP 3DCE with diode-array detector; capillary: fused-silica, L = 48 cm, l = 40 cm, 50 µm i.d., where L = total length and l = length to detector; voltage: –30 kV at pH 7, and –25 kV at pH 11.5; detection: photodiode-array, 190–600 nm; injection: 0.75 psi., 5 sec; sample concentration: 0.13 mM. The spectra of sorbate and phthalate were not affected by the pH change from 7 to 11.5.*

Table 1
DETECTION SENSITIVITIES FOR PHOSPHATE SUGARS AT VARIOUS WAVELENGTHS USING 4-HYDROXYBENZOATE AND PHTHALATE, RESPECTIVELY, AS BACKGROUND ELECTROLYTE[a]

	Lower detection limits in µM at a signal-to-noise ratio of 3				
	4-Hydroxybenzoate			Phthalate	
Phosphate sugars	195 nm	254 nm	280 nm	195 nm	254 nm
F2,6-BP	2.7	2.8	1.5	4.7	9.6
F1,6-BP	2.7	2.7	1.5	3.4	6.6
F6-P	3.6	4.0	2.3	5.9	9.5
G6-P	4.8	5.0	2.9	7.9	13.5

[a]Electrophoretic conditions identical to those described in Figure 8.

and has a high molar absorptivity. *Figure 2* shows a plot of peak areas of F1,6-BP, F2,6-BP, G6-P, and F6-P versus 4-hydroxybenzoate concentration. All the running buffers of different chromophore concentrations had been adjusted to pH 11.8–11.9. The peak areas of all four analytes increased up to 6 m*M* of 4-hydroxybenzoate. Thereafter, sensitivity decreased again. A maximum response at 6 m*M* of sorbate was also reported for the analysis of nonphosphorylated saccharides by CZE with indirect UV detection.[13] This has been attributed to the fact that with higher concentrations of background electrolyte, progressively less light reaches the photodiode, which diminishes the ability to measure a small change on top of a large background.[18]

Figure 3 shows that resolution of the sugar phosphates increased with increasing 4-hydroxybenzoate concentrations. Resolution is defined as

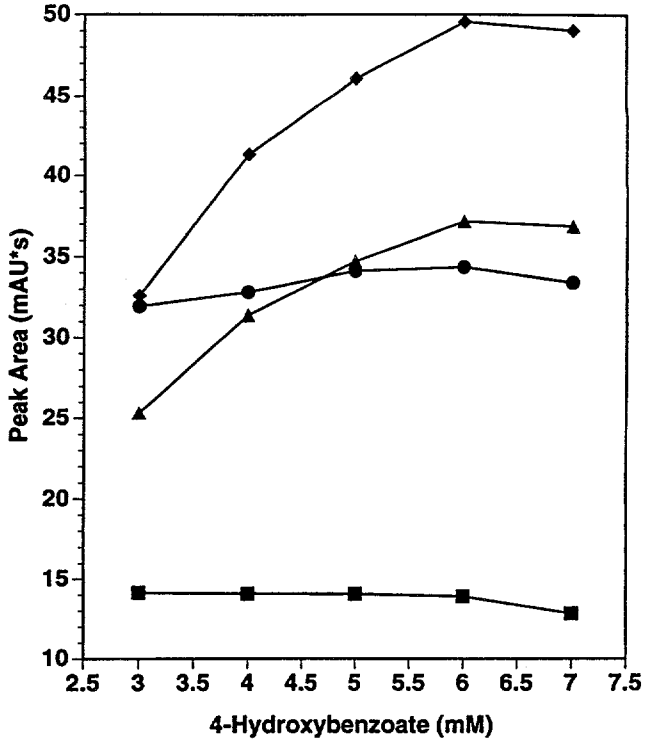

Figure 2 *Plots of peak area of F1,6-BP (dot), F2,6-BP (square), F6-P (triangle), and G6-P (diamond), respectively, as a function of the concentration of 4-hydroxybenzoate. Instrument: HP 3DCE; capillary: fused-silica, L = 48 cm, l = 40 cm, 50 µm i.d.; electrolyte: 3–7 mM 4-hydroxybenzoate, pH 11.9, 0.5 mM OFM Anion-BT; voltage: –15.9, –14.8, –14.0, –13.2, and –12.5 kV at 3.0, 4.0, 5.0, 6.0, and 7.0 mM 4-hydroxybenzoate, respectively; current: 15.6 µA; detection: photodiode-array, 280 nm; injection: 0.75 psi, 5 sec; sample: 53 µM of F2,6-BP, 105 µM of F1,6-BP, 115 µM of F6-P, and 153 µM of G6-P prepared in water.*

$$R = 2(t_2 - t_1)/(w_1 + w_2) \quad (1)$$

where t_2 and t_1 are the migration times of two adjacent peaks, and w_1/w_2 and w_2/w_1 are their respective baseline peak widths.

Effect of pH on detection sensitivity and resolution

The separation of F1,6-BP and F2,6-BP as well as G6-P and F6-P is pH dependent. When the sample contains inorganic phosphate, the separation of inorganic phosphate and the bisphosphate sugars is also pH dependent. *Figure 4* shows the separation of inorganic phosphate and the sugar phosphates at pH 10.3, 10.9, and 11.7, respectively. The higher pH ensures the complete separation of the two bisphosphate sugars from inorganic phosphate. In *Figure 5*, peak height of F1,6-BP, F2,6-BP, G6-P, and F6-P are plotted against the concentration of NaOH in a running buffer containing 5 m*M* 4-hydroxybenzoate. The resulting pH values of the buffer solutions ranged from 11.4 to 12.1, corresponding to 13–25 m*M* NaOH added. The compounds were prepared in an enzyme assay buffer of high ionic

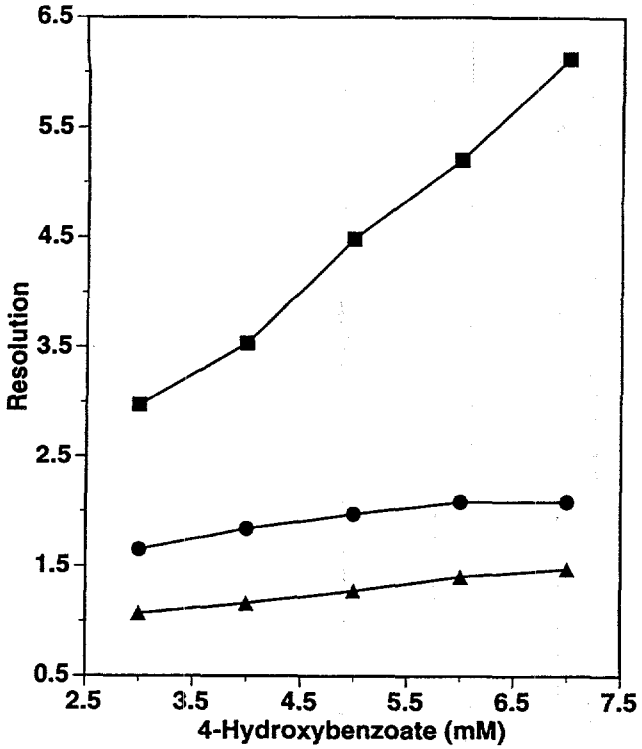

Figure 3 *Plots of resolution of inorganic phosphate and F2,6-BP (square), F2,6-BP and F1,6-BP (dot), as well as F6-P and G6-P (triangle), as a function of the concentration of 4-hydroxybenzoate. All conditions were as for Figure 2.*

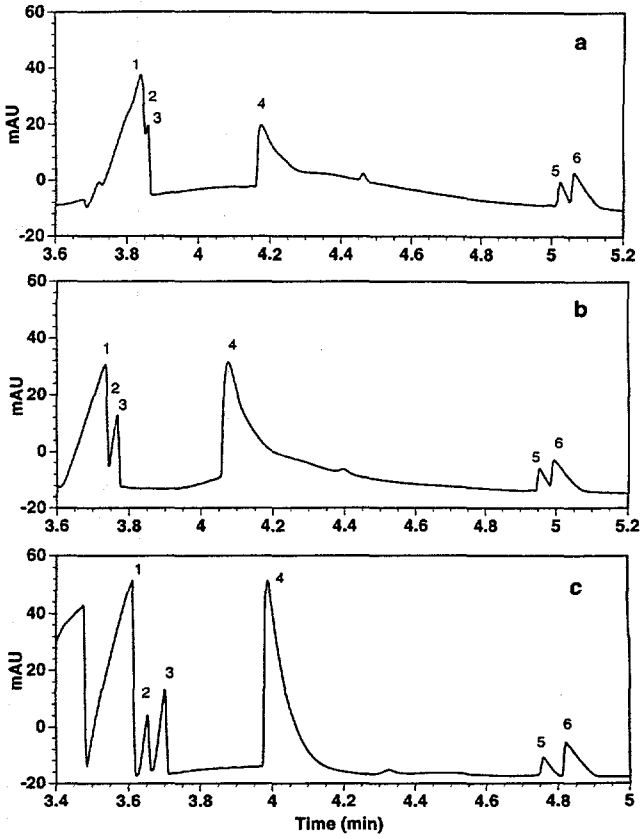

Figure 4 *Effect of pH on CZE of inorganic phosphate, F1,6-BP, F2,6-BP, F6-P, and G6-P. Instrument: HP ^{3D}CE; capillary: fused-silica, L = 48 cm, l = 40 cm, 50 µm i.d.; electrolyte: 5 mM 4-hydroxybenzoate, 0.5 mM OFM Anion-BT at a) pH 10.3, b) pH 10.9, and c) pH 11.7, respectively; voltage: –16 kV; detection: diode-array, 280 nm; injection: 0.75 psi, 5 sec. Peak identification: 1 = inorganic phosphate (1000 µM), 2 = F2,6-BP (80 µM), 3 = F1,6-BP (100 µM), 4 = ATP (1000 µM), 5 = F6-P (100 µM), and 6 = G6-P (120 µM). The sugar phosphates were prepared in an enzyme assay buffer containing 50 mM KCl, 20 mM HEPES, 1.0 mM K_2HPO_4, and 1.0 mM ATP pH adjusted to 7.8.*

strength. The peak height of F6-P decreased slightly with increasing pH, while no significant change in response occurred in the case of G6-P over the pH range studied. Significant increases in sensitivity, however, were observed for F1,6-BP and F2,6-BP up to 18 m*M* NaOH, pH 11.8 (Figure 5). A further increase in pH did not result in further improvements of sensitivity for the bisphosphate sugars. The decrease in sensitivity observed for F6-P with increasing pH may actually be a consequence of the degradation of this monophosphate sugar at higher pH. *Figure 6* shows the gradual degradation of F6-P occurring when prepared in a pH 12.0 solution, while it remained stable over a period of 500 min when prepared in a pH 11.0 solution. On the other hand, G6-P (Figure 6) as well as the bisphosphate sugars (data not shown) remained stable, even when dissolved in a pH 12.0 solution. Actually, F1,6-BP and F2,6-BP are known to be more stable in basic solution.[3] A previous study[13] on indirect UV detection of carbohydrates in CZE, using sorbic acid as running electrolyte, showed that detection sensitivity went through a maximum at an approximate pH of 12.1, higher concentrations of hydroxide ions exerted a dilution effect on the chromophore ion and hence resulted in reduced detection sensitivity.

The resolution of inorganic phosphate and F2,6-BP as well as F6-P and G6-P increased as the concentration of NaOH in the background electrolyte increased (*Figure 7*). The resolution between F1,6-BP and F2,6-BP increased up to 18 m*M* NaOH (pH=11.8), and decreased when the NaOH concentration reached 25 m*M*; at this point, the pH had passed both pK_a of F1,6-BP and F2,6-BP. The resolution has to be greater than 1 for a good quantitative analysis. Subsequently, the pH value of all running electrolytes was adjusted to 11.6–12.0. Overall, 5 m*M* 4-hydroxybenzoate, pH 11.6, was found to yield both an optimum sensitivity as well as resolution. *Figure 8* shows the optimized separation of 11 glycolysis metabolites prepared in water with 5 m*M* 4-hydroxybenzoate as running electrolyte at a detection wavelength of 280 nm.

Effect of sample ionic strength and Mg^{2+} ion content

Because glycolysis is an intracellular process, both biological samples and in vitro enzyme buffers usually contain large amounts of other metabolites as well as salts to maintain enzyme activity. For this reason, the

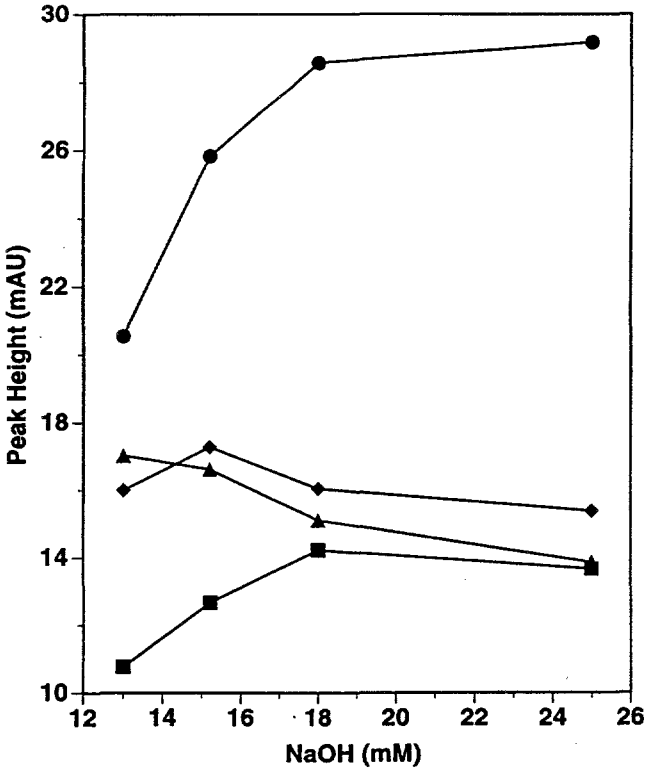

Figure 5 *Plots of peak height of F1,6-BP (dot), F2,6-BP (square), F6-P (triangle), and G6-P (diamond) versus concentration of NaOH in CZE buffer. Instrument: HP ^{3D}CE; capillary: fused-silica, L = 48 cm, l = 40 cm, 50 µm i.d.; electrolyte: 5 mM 4-hydroxybenzoate, 0.5 mM OFM Anion-BT, 11.5–25 mM NaOH, pH 11.4–12.1; voltage: –20, –15, –14, and –14 kV, respectively, at NaOH concentration of 13.0 mM (pH 11.4), 15.2 mM (pH 11.6), 18.0 mM (pH 11.8), and 25 mM (pH 12.1) of NaOH, respectively; current: 12.6, 12.6, 14.6, and 24.6 µA, respectively; detection: photodiode-array, 280 nm; injection: 0.75 psi, 5 sec; sample: 53 µM of F2,6-BP, 105 µM of F1,6-BP, 115 µM of F6-P, and 153 µM of G6-P prepared in the enzyme buffer containing 50 mM KCl, 50 mM HEPES, 5.0 mM $MgCl_2$, 1.0 mM DTT, 1.0 mM $MgHPO_4$, 3.0 mM ATP, and 1.0 mM ADP with pH adjusted to 7.2.*

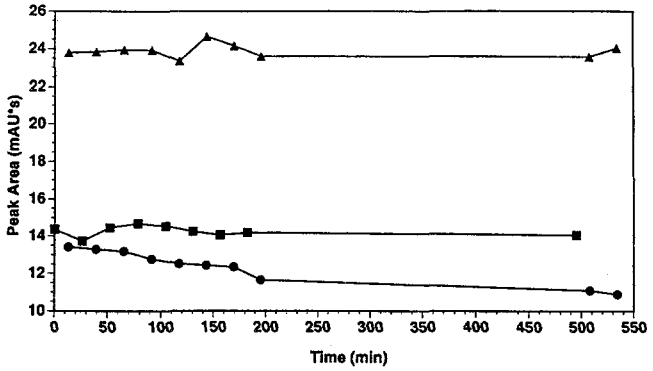

Figure 6 *Plots of peak area of F6-P and G6-P prepared in pH 11.0 and pH 12.0 CE buffer as a function of time. Square, dot, and triangle represent F6-P in pH 11.0, F6-P in pH 12.0, and G6-P in pH 12.0 buffer, respectively. Instrument: HP ^{3D}CE; capillary: fused-silica, L = 48 cm, l = 40 cm, 50 µm i.d.; electrolyte: 5 mM 4-hydroxybenzoate, 0.5 mM OFM Anion-BT, 18 mM NaOH, pH 11.8; voltage: –16 kV; current: 16.3 µA; detection: photodiode-array, 280 nm; injection: 0.75 psi, 5 sec; sample: 80 µM of F6-P and 120 µM of G6-P prepared in pH 11.0 and 12.0 CE buffer containing 5 mM 4-hydroxybenzoate and 0.5 mM OFM Anion-BT.*

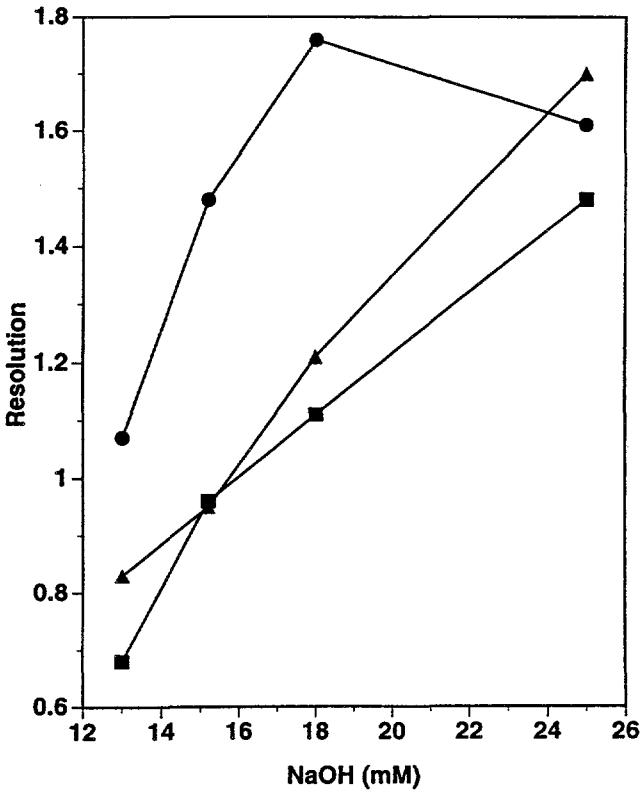

Figure 7 *Plots of resolution of inorganic phosphate and F2,6-BP (square), F2,6-BP and F1,6-BP (dot), as well as F6-P and G6-P (triangle), as a function of the concentration of NaOH. All conditions were as for Figure 5.*

authors studied the effect of high sample ionic strength on resolution and detection sensitivity. With the detection wavelength set at 280 nm, *Figure 9a* shows an electropherogram of low concentrations (50–100 µ*M*) of F2,6-BP, F1,6-BP, DHAP, F6-P, G6-P, pyruvate, and lactate, prepared in a high-ionic-strength enzyme assay buffer containing 50 m*M* HEPES, pH 7.2; 50 m*M* KCl; 5 m*M* $MgCl_2$; 1 m*M* $MgHPO_4$; 1 mM DTT; 3 m*M* ATP; and 0.6 m*M* ADP. This enzyme assay buffer is often used to study the enzymes involved in the glycolysis and gluconeogenesis pathway. Because of the high concentration of ATP in the buffer, its peak overlapped with DHAP. This rendered detection of DHAP difficult. With the detection wavelength set at 254 nm, however, the DHAP peak became clearly distinguishable from the negative ATP peak, as shown in Figure 9*b*. At this wavelength, ATP absorbs more light than 4-hydroxybenzoate. ADP was found to coelute with GAP. However, the concentration of GAP present in the sample can be calculated from that determined for DHAP, because a

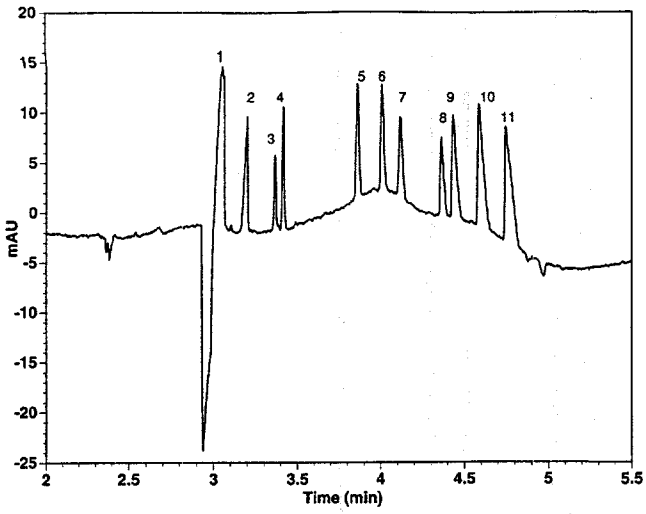

Figure 8 *CZE with indirect UV absorbance detection of 11 glycolysis metabolites. Instrument: HP 3DCE; capillary: fused-silica, L = 48 cm, l = 40 cm, 50 µm i.d.; electrolyte: 5 mM 4-hydroxybenzoate, 0.5 mM OFM Anion-BT, pH 11.6; voltage: –17 kV; current: 17.6 µA; detection: photodiode-array, 280 nm; injection: 0.75 psi, 5 sec. Peak identification: 1 = PEP (50 µM), 2 = inorganic phosphate (45 µM), 3 = F2,6-BP (30 µM), 4 = F1,6-BP (40 µM), 5 = DHAP (45 µM), 6 = GAP (45 µM), 7 = pyruvate (100 µM), 8 = F6-P (45 µM), 9 = G6-P (70 µM), 10 = lactate (220 µM), and 11 = AMP (190 µM).*

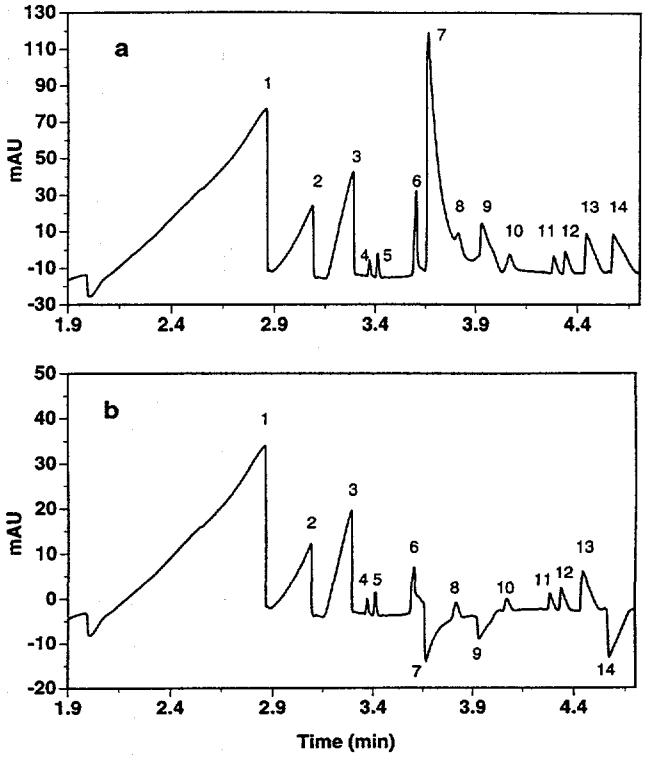

Figure 9 *Electropherograms recorded at a) 280 nm and b) 254 nm, respectively, of a mixture of F2,6-BP, F1,6-BP, DHAP, F6-P, and G6-P (50–100 µM each) prepared in a high-ionic-strength enzyme assay buffer containing 50 mM KCl, 50 mM HEPES, 5 mM $MgCl_2$, 1 mM DTT, 1 mM $MgHPO_4$, 3 mM ATP, and 0.6 mM ADP, adjusted to pH 7.1. Instrument: HP 3DCE; capillary: fused-silica, L = 48 cm, l = 40 cm, 50 µm i.d.; electrolyte: 5 mM 4-hydroxybenzoate, 0.5 mM OFM Anion-BT, 18 mM NaOH, pH 11.8; voltage: –17 kV; current: 17.6 µA; injection: 0.75 psi, 5 sec; detection: diode-array, a) 280 nm and b) 254 nm. Peak identification: 1 = chloride (50 mM), 2 = unknown, 3 = inorganic phosphate (1 mM), 4 = F2,6-BP (35 µM), 5 = F1,6-BP (40 µM), 6 = DTT (1 mM), 7 = ATP (3 mM), 8 = DHAP (45 µM), 9 = ADP (600 µM), 10 = pyruvate (110 µM), 11 = F6-P (45 µM), 12 = G6-P (70 µM), 13 = lactate (450 µM), and 14 = AMP (390 µM). In the upper trace, the ATP band overlaps with the DHAP band, which makes detection of DHAP at 280 nm difficult. With the detection wavelength set at 254 nm, the DHAP band becomes clearly distinguishable from the inverted ATP zone.*

fast equilibrium exists between DHAP and GAP in the presence of triosephosphate isomerase. The ratio of DHAP to GAP is 20:1. A high concentration of inorganic phosphate can affect its separation from F2,6-BP. The resolution between inorganic phosphate and F2,6-BP, prepared in deionized water at 50 µ*M* each, is 5.2. The value decreases to 1.1, when the same amount of F2,6-BP is prepared in the above-mentioned enzyme assay buffer containing 1 m*M* of inorganic phosphate. Resolution between F1,6-BP and F2,6-BP as well as F6-P and G6-P remained unchanged when the ionic strength of the sample was changed from low to high.

The enzyme assay buffer contains magnesium ions (6 m*M* in total). While F1,6-BP and F2,6-BP were baseline resolved initially, zones began to overlap with consecutive injections, as shown in *Figure 10a* and *b*. When the enzyme assay buffer contained no Mg^{2+}, separation between the bisphosphate sugars was not affected (Figure 10*c* and *d*). Overlapping of the F1,6-BP and F2,6-BP zones was also observed when samples were prepared in a 6.0 m*M* $MgCl_2$ solution only, as shown in Figure 10*e* and *f*. The replenishment of the running buffer before each injection effectively prevented overlapping of the zones of F1,6-BP and F2,6BP even when prepared in enzyme assay buffer containing 6.0 m*M* Mg^{2+} (*Figure 11a* and *b*) and in 6.0 m*M* $MgCl_2$ solution only (Figure 11*c* and *d*). The Mg^{2+} ions present in the sample solution also reduced the peak areas of the sugar phosphates, especially of the bisphosphate sugars. *Figure 12* shows the peak areas measured upon the 1st, 10th, and 23rd injection with and without buffer replenishment for F2,6-BP and G6-P prepared in deionized water, 6.0 m*M* $MgCl_2$, as well as in enzyme assay buffer containing either no Mg^{2+}, or 6.0 m*M* and 3.0 m*M* Mg^{2+}, respectively. For the samples injected with replenishment, the peak area reduction occurred only during the first two to three injections and the peak areas were quite reproducible thereafter. Magnesium ions are known to complex with phosphate groups, especially in compounds that have two or more phosphate residues, such as ATP, ADP, F1,6-BP, and F2,6-BP. It forms a strong complex if the two phosphate groups are spatially close to each other in geometry, i.e., the formation constants of Mg^{2+} and ATP and Mg^{2+} and ADP are 4×10^4 and 2×10^3, respectively. F2,6-BP forms a

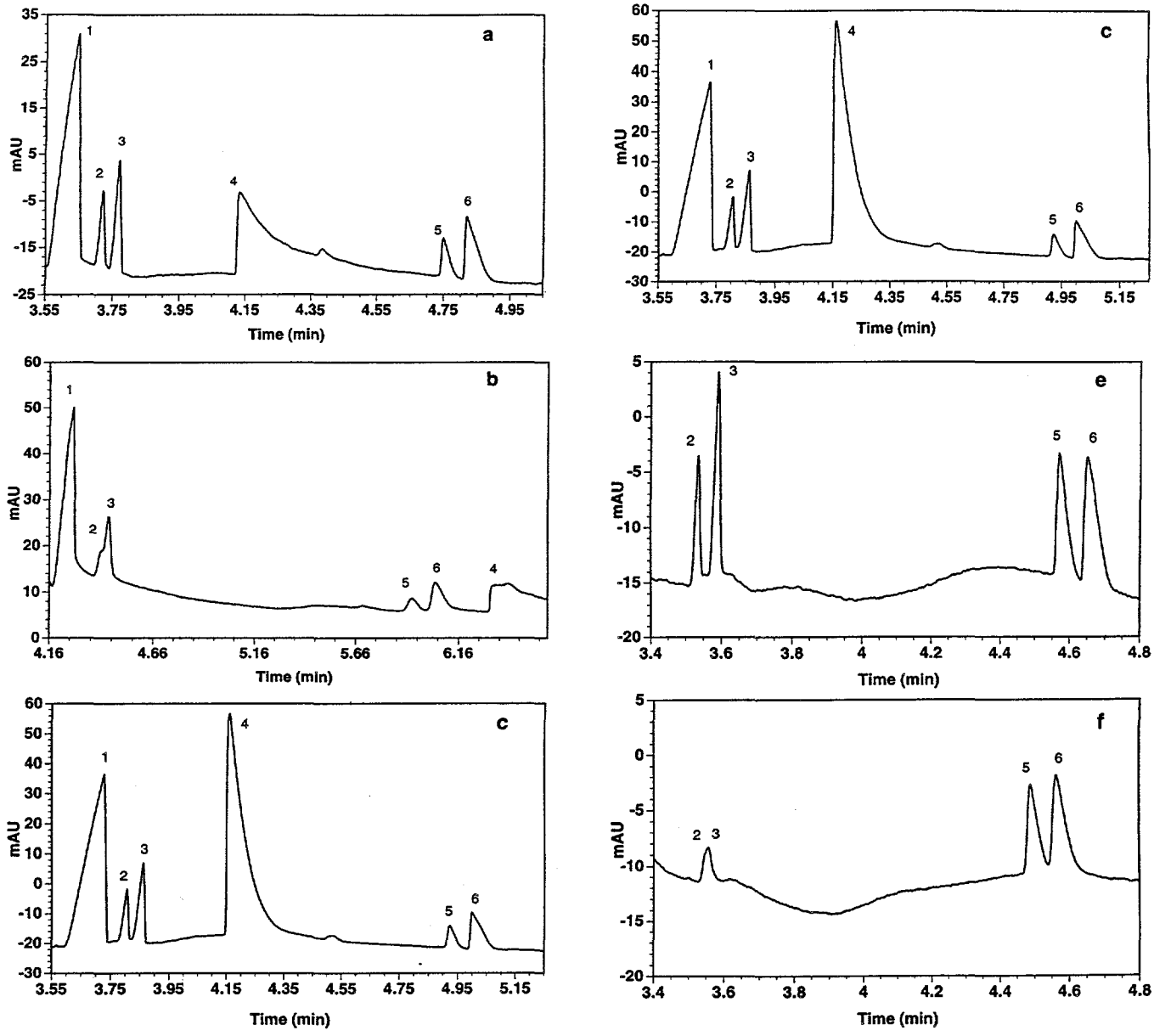

Figure 10 *Effects of Mg^{2+} on the CZE separation of F2,6-BP and F1,6-BP. The samples were prepared in the enzyme assay buffer containing 50 mM KCl, 20 mM HEPES, 1.0 mM K_2HPO_4, 1.0 mM ATP, pH 7.9, with 6.0 mM $MgCl_2$ (a and b), in the enzyme assay buffer without 6.0 mM $MgCl_2$ (c and d), and in 6.0 mM $MgCl_2$ only (e and f). First injection: a, c, and e; 23rd injection: b, d, and f. Instrument: HP ^{3D}CE; capillary: fused-silica, L = 48 cm, l = 40 cm, 50 µm i.d.; electrolyte: 5 mM 4-hydroxybenzoate, 0.5 mM OFM Anion-BT, 18 mM NaOH, pH 11.9; voltage: –16.0 kV; current: 16.3 µA; injection: 0.75 psi, 5 sec; detection: diode-array, 280 nm. Peak identification: 1 = inorganic phosphate (1000 µM), 2 = F2,6-BP (80 µM), 3 = F1,6-BP (100 µM), 4 = ATP (1000 µM), 5 = F6-P (100 µM), and 6 = G6-P (120 µM). A decrease in resolution of F2,6-BP and F1,6-BP is observed from first injection (a, c, and e) to 23rd injection (b, d, and f).*

stronger complex with Mg^{2+} than F1,6-BP because the ring structure dominates in F2,6-BP and the two phosphate groups are closer to each other than in F1,6-BP. Complexing with Mg^{2+} neutralizes the negative charges on the F2,6-BP molecule and causes a decrease in its electrophoretic mobility until it coelutes with F1,6-BP. A significant decrease in electrophoretic mobility is also evident in the case of ATP (Figure 10*b*). Neutralization of the negative charges on the sugar phosphate molecules reduces displacement of background chromophore, resulting in a reduction in peak area. With the cathode being located at the capillary inlet, cations such as Mg^{2+} accumulate in the inlet electrolyte reservoir with repeated injection of sample. The effect of the progressive accumulation of Mg^{2+} is observed even more rapidly in the case of the HP ^{3D}CE system because of the small volume (0.4 mL) of the inlet vial. Furthermore, the high pH (11.6–12.0) of the electrolyte may

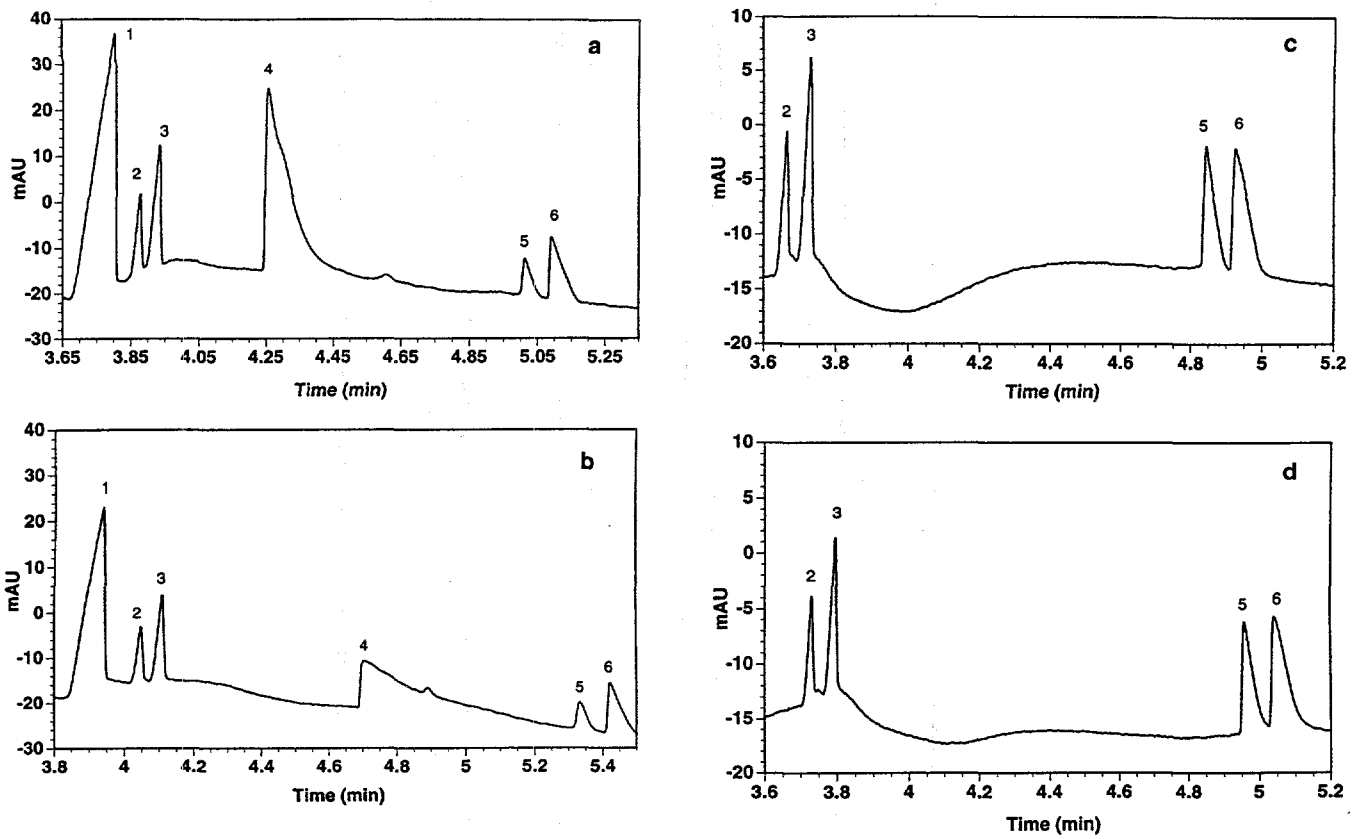

Figure 11 *Effects of replenishment of CE buffer on the CZE separation of F2,6-BP and F1,6-BP in the presence of 6.0 mM Mg^{2+}. The samples were prepared in the enzyme assay buffer containing 50 mM KCl, 20 mM HEPES, 1.0 mM K_2HPO_4, 1.0 mM ATP, pH 7.9, and 6.0 mM $MgCl_2$ (a and b) and in 6.0 mM $MgCl_2$ only (c and d). First injection: a and c; 23rd injection: b and d. Other conditions were as for Figure 10. No deterioration of separation efficiency is observed in the case of buffer replenishment after each run up to 23 injections.*

Table 2
LINEAR CORRELATION COEFFICIENTS OF THE CALIBRATION CURVES OF F1,6-BP, F2,6-BP, F6-P, G6-P, AND DHAP PREPARED IN BOTH LOW- AND HIGH-IONIC STRENGTH SOLUTIONS OVER A CONCENTRATION RANGE OF 6.25–200 µM

	Linear correlation coefficients of the calibration curves				
Ionic strength of the sample	F2,6-BP	F1,6-BP	DHAP	F6-P	G6-P
Low[a]	0.9999	0.9996	–	0.9999	0.997
High[b]	0.993	0.993	0.993	0.995	0.995

[a]HP ^{3D}CE with diode-array detector, L = 48 cm, l = 40 cm, 50 µm i.d., 5 m*M* 4-hydroxybenzoate, pH 11.6, 0.5 m*M* OFM Anion-BT, –15 kV, 5-sec injection at 0.75 psi.
[b]P/ACE 5510 with UV 254-nm filter detector, L = 117 cm, l = 110 cm, 75 µm i.d., 3 m*M* 4-hydroxybenzoate, pH 11.6, 0.5 m*M* OFM Anion-BT, –20 kV. 15-sec injection at 0.5 psi.

Table 3
DETECTION SENSITIVITIES FOR PHOSPHATE SUGARS AS A FUNCTION OF SAMPLE IONIC STRENGTH USING 4-HYDROXYBENZOATE AS BACKGROUND ELECTROLYTE[a]

	Lower detection limits in µM at a signal-to-noise ratio of 3			
Ionic strength	F2,6-BP	F1,6-BP	F6-P	G6-P
Low	1.5	1.5	2.3	2.9
High	1.3	1.3	1.7	2.0

[a]Electrophoretic conditions identical to those described in Figure 8.

also cause precipitation of Mg^{2+} to $Mg(OH)_2$ with K_{sp} (solubility product) = 10.7. Replenishment of the background electrolyte is an effective way to prevent the accumulation of Mg^{2+} in the buffer vials.

Quantitation and detection limits

Independent of the instrument used, excellent linearity was observed over a concentration range of 6.25–200 µ*M*. The linear correlation coefficients obtained for F2,6-BP, F1,6-BP, DHAP, F6-P, and G6-P, which were prepared both in deionized water as well as in high-ionic-strength enzyme buffer, are depicted in *Table 2*.

The detection limits for F1,6-BP, F2,6-BP, DHAP, F6-P, and G6-P, prepared both in deionized water (low

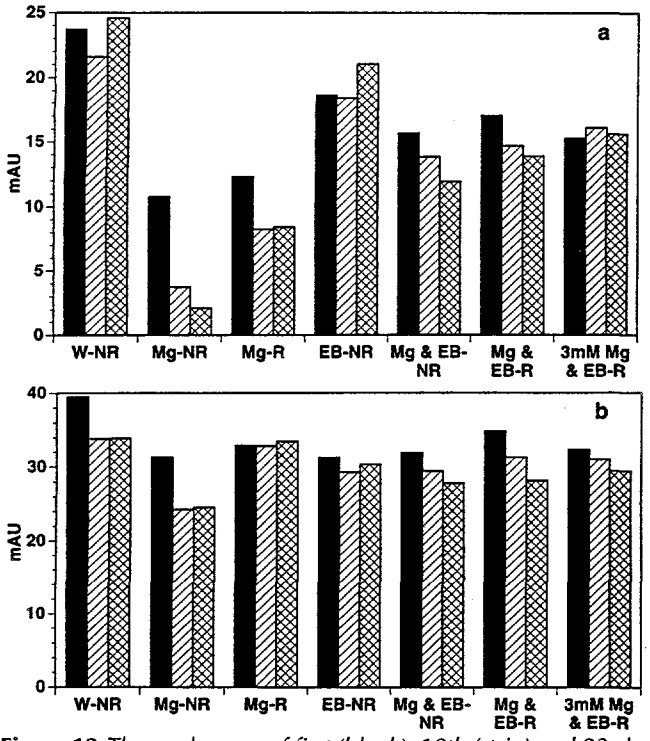

Figure 12 *The peak areas of first (black), 10th (strip) and 23rd (cross) injection with and without buffer replenishment for F2,6-BP (a) and G6-P (b). Samples were prepared in deionized water without replenishment (W-NR), in 6.0 mM $MgCl_2$ without replenishment (Mg-NR) and with replenishment (Mg-R), and in enzyme assay buffer without 6.0 mM Mg^{2+} and no replenishment (EB-NR), with 6.0 mM Mg^{2+} and no replenishment (Mg and EB-NR), with 6.0 mM Mg^{2+} and replenishment (Mg and EB-R), and with 3.0 mM Mg^{2+} and replenishment (3 mM Mg and EB-R). Other conditions were the same as for Figure 10.*

ionic strength) and enzyme assay buffer (high ionic strength) are given in *Table 3*. A lower detection limit was obtained when the sample molecules were prepared in a high-ionic-strength enzyme assay buffer. When the P/ACE 5510 was equipped with a photodiode-array detector, no difference in sensitivity was observed compared to the HP ^{3D}CE system. The Beckman system, however, was about 30% less sensitive when equipped with the filter UV detector, because less light reached the detector. The upper detection limit was mainly determined by the resolution attained for the two pairs of isomers, namely F1,6-BP and F2,6-BP, as well as F6-P and G6-P. The estimated upper detection limit is about 0.3 m*M*. This does not limit the applicability of the method since the physiological concentrations of these phosphate compounds are far less than 0.3 m*M*.

Conclusions

Using 5 m*M* 4-hydroxybenzoate, pH 11.8, as background electrolyte, CZE with indirect UV detection allowed the simultaneous analysis of G6-P, F6-P, F1,6-BP, F2,6-BP, DHAP, GAP, PEP, pyruvate, and lactate. The optimum detection wavelength under these alkaline conditions was 280 nm. The detection limits for G6-P, F6-P, F1,6-BP, and F2,6-BP ranged from 1 to 3 μ*M*. Linearity was observed over one to two orders of magnitude and was primarily limited by the resolution attained at high concentrations for G6-P and F6-P as well as F1,6-BP and F2,6-BP, respectively. The method may serve as a valuable technique in the routine measurement and monitoring of glycolysis metabolites.

Acknowledgment

This work was supported, in part, by the National Science Foundation and the Department of Energy/Basic Energy Science.

Manuscript received March 15, 1996

References

1. Michal G. D-Glucose 6-phosphate and D-fructose 6-phosphate. Methods of enzymatic analysis. Weinheim: Verlag Chemie, 1984, 6:191–8.
2. Michal G. D-Fructose 1,6-bisphosphate, dihydroxyacetone phosphate and D-glyceraldehyde 3-phosphate. Methods of Enzymatic Analysis. Weinheim: Verlag Chemie, 1984, 6:342–50.
3. Schaftingen E. D-Fructose 2,6-phosphate. Methods of enzymatic analysis. Weinheim: Verlag Chemie, 1984; 6:335–41.
4. Lamprecht W, Heinz F. D-Glycerate 2-phosphate and phosphoenolpyruvate. Methods of enzymatic analysis. Weinheim: Verlag Chemie, 1984, 6:555–61.
5. Lamprecht W, Heinz F. Pyruvate. Methods of enzymatic analysis. Weinheim: Verlag Chemie, 1984, 6:570–7.
6. Noll F. L-(+)-Lactate. Methods of enzymatic analysis. Weinheim: Verlag Chemie, 1984, 6:582–8.
7. Romano J, Jandik P, Jones WR, Jackson PE. Optimization of inorganic capillary electrophoresis for the analysis of anionic solutes in real sample. J Chromatogr 1991; 546:411–21.
8. Kenney BF. Determination of organic acids in food samples by capillary electrophoresis. J Chromatogr 1991; 546:423–30.
9. Jandik P, Jones WR. Optimization of detection sensitivity in the capillary electrophoresis of inorganic anions. J Chromatogr 1991; 546:431–43.
10. Jandik P, Jones WR. Controlled changes of selectivity in the separation of ions by capillary electrophoresis. J Chromatogr 1991; 546:445–58.
11. Jandik P, Jones WR. Various approaches to analysis of difficult sample matrices of anions using capillary ion electrophoresis. J Chromatogr 1992; 608:385–93.
12. Oefner PJ. Surface-charge reversed capillary zone electrophoresis of inorganic and organic anions. Electrophoresis 1995; 16:46–56.
13. Vorndran AE, Oefner PJ, Scherz H, Bonn GK. Indirect UV detection of carbohydrates in capillary zone electrophoresis. Chromatographia 1992; 33:163–8.
14. Shamsi SA, Danielson ND. Ribonucleotide electrolytes for capillary electrophoresis of polyphosphates and polyphosphonates with indirect photometric detection. Anal Chem 1995; 67:1845–52.
15. Dabek-Zlotorzynska E, Dlouhy JF. Capillary zone electrophoresis with indirect UV detection of organic anions using 2,6-naphthalenedicarboxylic acid. J Chromatogr A 1994; 685:145–53.
16. Henshall A, Harrold MP, Tso JMY. Separation of inositol phosphates by capillary electrophoresis. J Chromatogr 1992; 608:413–9.
17. Buchberger W, Cousins SM, Haddad PR. Optimization of indirect UV detection in capillary zone electrophoresis of low-molecular-mass anions. Trends Anal Chem 1994; 13:313–9.
18. Yeung ES. Indirect detection methods: looking for what is not there. Acc Chem Res 1989; 22:125–8.

PATTERN FORMATION IN RAYLEIGH-BÉNARD CONVECTION AT SMALL PRANDTL NUMBERS AND WITH ROTATION ABOUT A VERTICAL AXIS

Guenter Ahlers

Department of Physics and Center for Nonlinear Science
University of California, Santa Barbara, California 93106, USA

Abstract

We review results from and future prospects for experimental studies of Rayleigh-Bénard convection with rotation about a vertical axis. At dimensionless rotation rates $0 \leq \Omega \leq 20$ and for Prandtl numbers $\sigma \simeq 1$, Küppers-Lortz-unstable patterns offered a unique opportunity to study spatio-temporal chaos immediately above a supercritical bifurcation where weakly-nonlinear theories in the form of Ginzburg-Landau (GL) or Swift-Hohenberg (SH) equations can be expected to be valid. However, the dependence of the time and length scales of the chaotic state on $\epsilon \equiv \Delta T/\Delta T_c - 1$ was found to be different from the expected dependence based on the structure of GL equations. For $\Omega \gtrsim 70$ and $0.7 \lesssim \sigma \lesssim 5$ patterns were found to be cellular near onset with local four-fold coordination. They differ from the theoretically expected Küppers-Lortz-unstable state. Stable as well as intermittent defect-free rotating square lattices exist in this parameter range.

Smaller Prandtl numbers ($0.16 \lesssim \sigma \lesssim 0.7$) can only be reached in mixtures of gases. These fluids are expected to offer rich future opportunities for the study of a line of tricritical bifurcations, of supercritical Hopf bifurcations to standing waves, of a line of codimension-two points, and of a codimension-three point.

I. INTRODUCTION

Convection in a thin horizontal layer of a fluid heated from below (Rayleigh-Bénard convection or RBC) has become a paradigm for the study of pattern formation. [1] It evolves from the spatially-uniform pure-conduction state *via* a supercritical bifurcation when the temperature difference ΔT is increased beyond a critical value ΔT_c.

It reveals numerous interesting phenomena including spatio-temporal chaos (STC) as $\epsilon \equiv \Delta T/\Delta T_c - 1$ grows. [1] Many of these phenomena have been studied in detail recently by our groups at Los Alamos [2–8] and at Santa Barbara [9–15], as well as by others [16–20], using primarily compressed gases as the fluid, sensitive shadowgraph flow-visualization, image analysis, and quantitative heat-flux measurements [12]. However, as ΔT_c is approached from above and ϵ becomes small enough for the pattern-formation problem to become theoretically tractable by weakly-nonlinear methods, the system becomes relatively simple and its behavior can be described in potential (or variational) form. Then the steady-state pattern is time independent. In the absence of perturbing boundaries it consists of parallel rolls as shown in Fig. 1a [13] and as predicted theoretically [21] already 33 years ago.

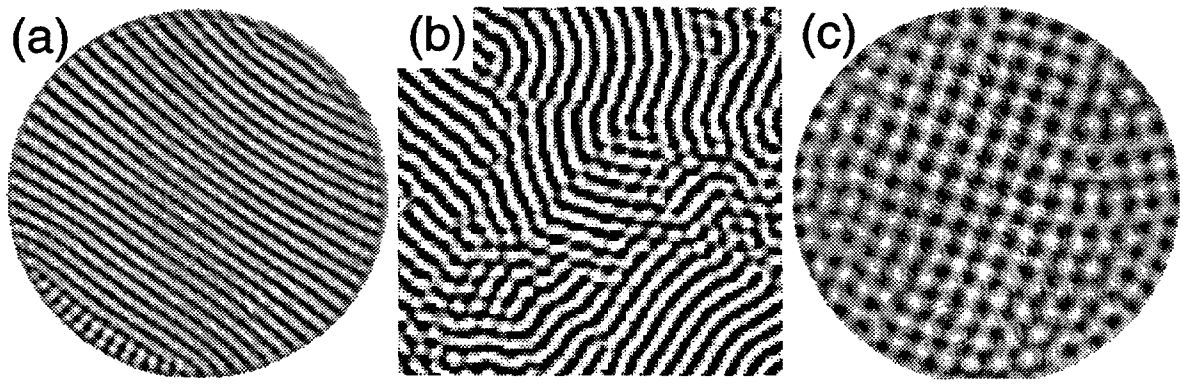

Fig. 1. Convection patterns for small ϵ. (a) is for $\Omega = 0$ and Ar gas with $\sigma = 0.69$ and $\epsilon = 0.07$ (from Ref. [13]). It shows the predicted [21] straight-roll pattern. (b) is for $\Omega = 15.4$ and CO_2 at a pressure of 32 bar with $\sigma = 1.0$ and $\epsilon = 0.05$ (from Ref. [22]). It shows a typical example of a pattern in the Küppers-Lortz-unstable range. (c) is for Argon at 40 bar with $\sigma = 0.7$, $\Omega = 145$, and $\epsilon = 0.04$ (from Ref. [23]); it shows no evidence of the Küppers-Lortz instability, and instead consists of a slowly-rotating square lattice.

The system becomes much more complex and interesting even near onset when it is rotated about a vertical axis with an angular velocity $\vec{\Omega}$. In that case the coriolis force proportional to $\vec{\Omega} \times \vec{v}$ acts on the fluid (here $\vec{v}$ is the fluid velocity field in the rotating frame) and renders the system non-variational. Thus time dependent states can occur arbitrarily close to onset. Since the bifurcation remains supercritical for $\Omega > 0$, the flow amplitudes still grow continuously from zero and the usual weakly-nonlinear theories, for instance in the form of GL or SH equations, should remain applicable. Thus one may expect interesting new effects to occur in a theoretically tractable parameter range.

Indeed it was predicted [24–26] that, for $\Omega > \Omega_c$, the primary bifurcation from the conduction state should be to parallel rolls which are *unstable*. Although Ω_c depends on the Prandtl number σ (the ratio of the kinematic viscosity ν to the thermal diffusivity κ), it has a value near 14 for the σ-values near unity which are characteristic of compressed

gases (Ω is made dimensionless by scaling time with the vertical viscous diffusion time d^2/ν where d is the cell thickness). The instability is to plane-wave perturbations which are advanced relative to the rolls at an angle Θ_{KL} in the direction of $\vec{\Omega}$. This phenomenon is known as the Küppers-Lortz instability. A snapshot [22] of the resulting nonlinear state of convection is shown in Fig. 1b. The pattern consists of domains of rolls which incessantly replace each other, primarily by irregular domain-wall motion. [2,22,27–30] The spatial and temporal behavior suggests the term "domain chaos" for this state. We discuss this state in the next Section.

Theoretically, the KL instability is expected to persist near onset up to large values of Ω. Thus it was a surprise that the patterns found in experiments near onset changed dramatically when Ω was increased. [23] For $\Omega \gtrsim 70$, there was no evidence of the characteristic domain chaos until ϵ was increased well above 0.1. At smaller ϵ, slowly-rotating, aesthetically appealing, square lattices were encountered. Since these experimental observations are very new, it remains to be seen whether a reasonable explanation can be offered. They will be discussed in Sect. III.

Finally, we look forward to as yet unrealized experimental opportunities which this system has to offer in the parameter range of Prandtl numbers well below unity. Pure fluids (with rare exceptions [31]) have $\sigma \gtrsim 0.7$. Recently it was shown [13,14] that smaller values of σ can be reached by mixing two gases, one with a large and the other with a small atomic or molecular weight. The most extreme example readily available is a mixture of H_2 and Xe. Prandtl numbers as small as 0.16 can be reached. In the range $\sigma \lesssim 0.6$, a number of interesting new phenomena are predicted to occur. [26,32] In the $\sigma - \Omega$ plane they include subcritical bifurcations below a line of tricritical bifurcations, [33] Hopf bifurcations to standing waves, a line of codimension-two points where the Hopf bifurcation meets the stationary bifurcation, and a codimension-three point where the codimension-two line and the tricritical line meet. The opportunities for research in this parameter range are outlined in Sect. IV.

II. KÜPPERS-LORTZ DOMAIN-CHAOS

For $\sigma \gtrsim 0.33$, the bifurcation to convection in the presence of rotation is expected to be supercritical both below and above Ω_c. Thus the KL instability offers a rare opportunity to study STC in a system where the average flow amplitude evolves continuously from zero and where thus weakly-nonlinear theories might be expected to be applicable. After receiving only limited attention for several decades [24–28,34,35], the opportunity to study STC has led to a recent increase in activity both theoretically and experimentally [12,22,36–42]. Indeed, as predicted theoretically, [24] the straight rolls at the onset of convection for dimensionless rotation rates $\Omega > \Omega_c$ are unstable to another set of rolls oriented at an angle Θ_s with respect to the original rolls along the direction of rotation. In the spatially extended system this leads to the co-existance of domains of rolls of more or less uniform orientation with other domains of a different orientation. A typical example is shown in Fig. 1b. Experiments by Heikes and Busse [27,28] in water using

shadowgraph visualization rather far from onset ($\epsilon \gtrsim 0.5$) established qualitatively the existence of the KL instability. The replacement of a given domain of rolls proceeded via domain-wall propagation. More recently our Los Alamos group investigated the KL instability with shadowgraph flow-visualization very close to onset and demonstrated that the bifurcation is indeed supercritical, and that the instability leads to a continuous domain switching through a mechanism of domain-wall propagation also at small ϵ. [2,22,29,30] This qualitative feature has been reproduced by Tu and Cross [38] in numerical solutions of appropriate coupled GL equations, as well as by Neufeld et al. [40] and Cross et al. [41] through numerical integration of a generalized SH equation.

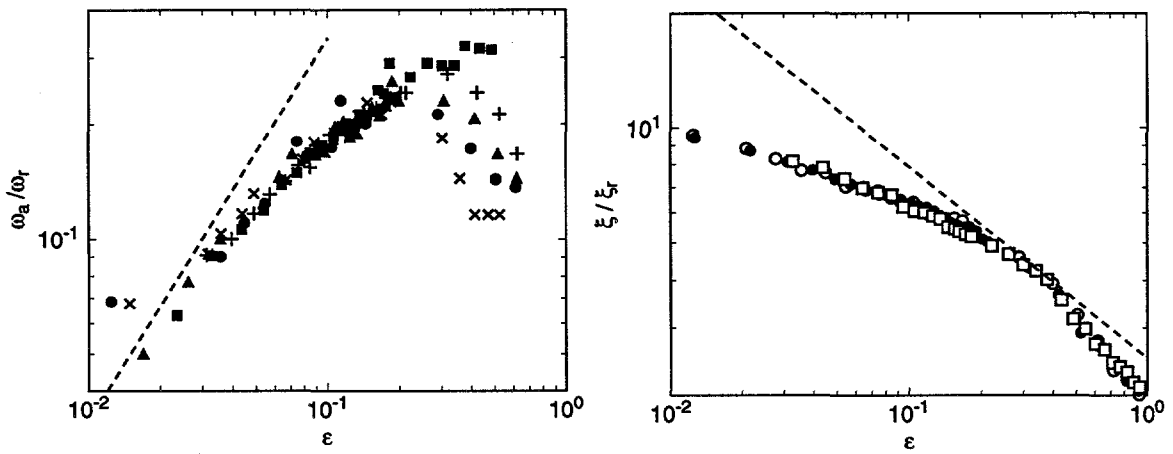

Fig. 2. The characteristic frequencies ω_a (left) and lengths ξ (right) of the KL state. The data were divided by Ω-dependent constants ω_r and ξ_r so as to collapse them onto single curves. The dashed lines are shown for reference and have the slopes 1 for ω_a and -1/2 for ξ which correspond to the theoretically expected exponents of the time and length scales near onset. The data sets cover approximately the range $14 \lesssim \Omega \lesssim 20$. See Refs. [22], [29], and [30] for details.

Of interest are the time and length scales of the KL instability near onset. The GL model assumes implicitly a characteristic time dependence which varies as ϵ^{-1} and a correlation length which varies as $\epsilon^{-1/2}$. We measured a correlation length given by the inverse width of the square of the modulus of the Fourier transform as well as a domain-switching frequency as revealed in Fourier space, and obtained the data in Fig. 2. [22,29] These results seem to be inconsistent with GL equations since they show that the time in the experiment scales approximately as $\epsilon^{-1/2}$ and that the two-point correlation length scales approximately as $\epsilon^{-1/4}$. These results also differ from numerical results based on a generalized SH equation [41] although the range of ϵ in the numerical work is rather limited. We regard the disagreement between experiment and theory as a major problem in our understanding of STC. [43]

III. SQUARE PATTERNS AT MODEST σ

Motivated by the unexpected scaling of length and time with ϵ for the KL state at $\Omega \lesssim 20$, our Santa Barbara group started a new investigation in which the range of Ω was significantly extended to larger values. To our surprise and contrary to theoretical predictions [26,32], we found [23] in preliminary work that for $\Omega \gtrsim 70$ the nature of the pattern near onset changed qualitatively although the bifurcation remained supercritical. We found square patterns like the one shown in Fig. 1c, instead of typical KL patterns like the one in Fig. 1b. The squares occurred both when we used Argon with $\sigma = 0.69$ and when the fluid was water with $\sigma \simeq 5$. The occurrence of squares in this system is completely unexpected and not predicted by theory; according to the theory the KL instability should continue to be found near onset also at these higher values of Ω. Thus our preliminary work has uncovered a major disagreement with theoretical predictions in a parameter range where one might have expected the theory to be reliable. We believe that this calls for a systematic experimental study over appropriate parameter ranges. We expect to explore the range $0 \lesssim \Omega \lesssim 400$ and $0.7 \lesssim \sigma \lesssim 5$ in the near future, and hope that this will shed light on the extent and origin of the difference between the physical system and the predictions.

IV. THE RANGE $0.16 < \sigma < 0.7$

When a RBC system is rotated about a vertical axis, the critical Rayleigh number $R_c(\Omega)$ increases as shown in Fig. 3a. $R_c(\Omega)$ is predicted to be independent of σ, and experiment [29] and theory [44] for it are in excellent agreement. For $\sigma > 0.33$ the bifurcation is expected to be supercritical and to lead to KL chaos unless Ω is quite large. As discussed above in Sect. III, our recent preliminary experiments have cast doubt upon this; for $\Omega \gtrsim 70$ we found square patterns which are clearly unrelated to the typical KL domains. For large Ω and $\sigma < 0.68$, the stationary bifurcation is predicted [32] to be preceded by a supercritical Hopf bifurcation; but for $\sigma > 0.33$ we do not expect to reach values of Ω sufficiently high to encounter this in the experiment.

The range $0.16 \lesssim \sigma \lesssim 0.33$ is truly remarkable because of the richness of the bifurcation phenomena which occur there when the system is rotated. For instance, for $\sigma = 0.26$ there is a range from $\Omega \simeq 16$ to 190 over which the bifurcation is predicted to be subcritical. This is shown by the dashed section of the curve in Fig. 3c. The subcritical range depends on σ. In Fig. 3b it covers the area below the dashed curve. Thus, the dashed curve is a *line* of tricritical bifurcations. [33] It has a maximum in the $\Omega - \sigma$ plane, terminating in a "tricritical endpoint". An analysis of the bifurcation phenomena which occur near it in terms of Landau equations may turn out to be interesting. One may expect path-renormalization [45] of the classical exponents in the vicinity of the maximum. We are not aware of equivalent phenomena in equilibrium phase transitions, although presumably they exist in as yet unexplored parameter ranges.

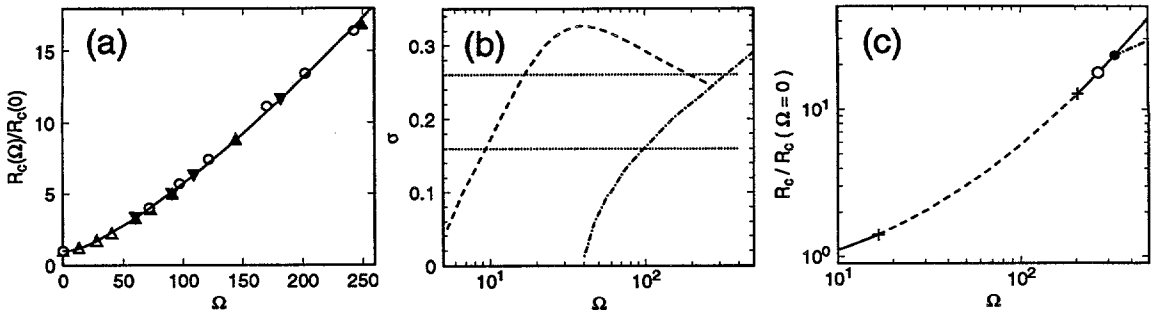

Fig. 3. The bifurcation diagram for RBC with rotation about a vertical axis. (a.) Experimental and theoretical results for $R_c(\Omega)$ obtained with water (open circles) and Ar at two different pressures (triangles) on linear scales. After Ref. [23]. This curve is expected to be independent of σ. (b.) The dashed curve gives the predicted tricritical line in the $\Omega - \sigma$ plane (the Ω axis is logarithmic). The dash-dotted line is the predicted codimension-two line where the Hopf bifurcation is expected to meet the stationary bifurcation [e.g. the solid circle for $\sigma = 0.26$ in Fig. (c)]. For $\sigma = 0.24$ the codimension-two line is expected to intersect the tricritical line, leading to the codimension-three point shown by the open circle in (c.). The upper dotted line in (b.) corresponds to the path represented in (c.). The lower dotted line in (b.) represents the lowest σ-value accessible to experiment using gas mixtures. (c.) The solid and dashed lines show the critical Rayleigh number as a function of Ω as in (a), but on logarithmic scales. The dashed line shows the range over which the bifurcation is predicted to be subcritical for $\sigma = 0.26$. The two plusses, indicating the limits of this range, are the tricritical points for this σ-value. The dash-dotted line at large Ω shows the predicted Hopf bifurcation for $\sigma = 0.26$.

At relatively large Ω, the stationary bifurcation (regardless of whether it is super- or sub-critical) is predicted to be preceded by a supercritical Hopf bifurcation which is expected to lead to *standing* waves of convection rolls. [32] Standing waves are relatively rare; usually a Hopf bifurcation in a spatially-extended system leads to traveling waves. An example is shown by the dash-dotted line near the right edge of Fig. 3b. As can be seen there, the Hopf bifurcation terminates at small Ω at a codimension-two point on the stationary bifurcation which, depending on σ, can be super- or sub-critical. The line of codimension-two points is shown in Fig. 3a as a dash-dotted line. One sees that the tricritical line and the codimension-two line meet at a codimension-three point, located at $\Omega \simeq 270$ and $\sigma \simeq 0.24$. We note that this is well within the parameter range accessible to our experiments. We are not aware of any experimentally-accessible examples of codimension-three points. This particular case should be accessible to analysis by weakly-nonlinear theories, and a theoretical description in terms of GL equations would be extremely interesting and could be compared with experimental measurements.

The σ-range of interest is readily accessible to us by using mixtures of a heavy and a light gas. [14] Values of σ *vs.* the mole fraction x of the heavy component for a typical pressure of 22 bar and at 25 °C are shown in Fig. 4. An important question in this

relation is whether the mixtures will behave in the same way as pure fluids with the same σ. We believe that to a good approximation this is the case because the Lewis numbers are of order one. This means that heat diffusion and mass diffusion occur on similar time scales. In that case, the concentration gradient will simply contribute to the buoyancy force in synchrony with the thermally-induced density gradient, and thus the critical Rayleigh number will be reduced. Scaling bifurcation lines by $R_c(\Psi)$ (Ψ is the separation ratio of the mixture) will mostly account for the mixture effect. To a limited extent we showed already that this is the case. [13,14] In more recent work we have begun to show that the bifurcation line $R_c(\Omega)/R_c(0)$ is independent of Ψ. Nonetheless we recognize that a theoretical investigation of this issue will be very important.

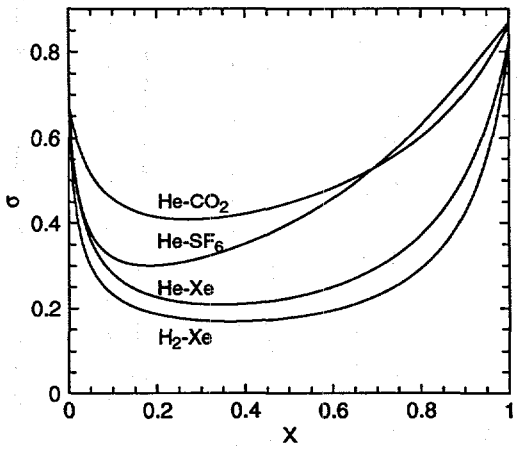

Fig. 4. The Prandtl number σ as a function of the mole fraction x of the heavy component for three gas mixtures at a pressure of 22 bar and at 25 °C. From Ref. [14].

Assuming that the mixtures behave approximately like pure fluids, we see that the codimension-three point can be reached using either H_2-Xe or He-Xe mixtures. The tricritical point can be reached also using He-SF_6.

V. ACKNOWLEDGMENT

The contents of this review is based on the work of many members of our groups, both at Santa Barbara and at Los Alamos. These include Kapil Bajaj, Robert Ecke, Yu-Chou Hu, Jun Liu, Ronnie Mainieri, Brian Naberhuis, and others. I am also much indebted to discussions with a number of scientists elsewhere, including particularly Fritz Busse, Mike Cross, and Werner Pesch. This work was supported by the Department of Energy through Grant DE-FG03-87ER13738.

REFERENCES

[1] For a recent review, see for instance, M. C. Cross and P.C. Hohenberg, Rev. Mod. Phys. **65**, 851 (1993).

[2] E. Bodenschatz, D. S. Cannell, J.R. de Bruyn, R. Ecke, Y. Hu, K. Lerman, and G. Ahlers, Physica D **61**, 77 (1992).

[3] Y. Hu, R. E. Ecke, and G. Ahlers, Phys. Rev. E **48**, 4399 (1993).

[4] L. Ning, Y. Hu, R. E. Ecke, and G. Ahlers, Phys. Rev. Lett. **71**, 2216 (1993).

[5] Y. Hu, R. E. Ecke, and G. Ahlers, Phys. Rev. Lett. **72**, 2191 (1994).

[6] Y. Hu, R. E. Ecke, and G. Ahlers, Phys. Rev. Lett. **74**, 391 (1995).

[7] Y. Hu, R. E. Ecke, and G. Ahlers, Phys. Rev. E **51**, 3263 (1995).

[8] R. E. Ecke, Y. Hu, R. Mainieri, and G. Ahlers, Science **269**, 1704 (1995).

[9] E. Bodenschatz, J. R. de Bruyn, G. Ahlers, and D. S. Cannell", Phys. Rev. Lett. **67**, 3078 (1991).

[10] S. W. Morris, E. Bodenschatz, D. S. Cannell, and G. Ahlers, Phys. Rev. Lett. **71**, 2026 (1993).

[11] S. W. Morris, E. Bodenschatz, D. S. Cannell, and G. Ahlers, Physica D **97**, 164 (1996)

[12] J. R. de Bruyn, E. Bodenschatz, S. W. Morris, S. Trainoff, Y. Hu, D. S. Cannell, and G. Ahlers, Rev. Sci. Instrum. **67**, 2043 (1996).

[13] J. Liu and G. Ahlers, Phys. Rev. Lett. **77**, 3126 (1996).

[14] J. Liu and G. Ahlers, Phys. Rev. E **55**, 6950 (1997).

[15] K.M.S. Bajaj, D.S. Cannell, and G. Ahlers, Phys. Rev. E **55**, R4869 (1997).

[16] V. Croquette, Contemp. Phys. **30**, 113 (1989); 153 (1989).

[17] M. Assenheimer and V. Steinberg, Phys. Rev. Lett. **70** 3888 (1993).

[18] M. Assenheimer and V. Steinberg, Nature **367**, 345 (1994).

[19] B.B. Plapp and E. Bodenschatz, Phys. Script. **T67**, 111 (1996).

[20] R.V. Cakmur, D.A. Egolf, B.B. Plapp, and E. Bodenschatz, Phys. Rev. Lett. **79**, 1853 (1997).

[21] A. Schlüter, D. Lortz, and F. Busse, J. Fluid Mech. **23**, 129 (1965).

[22] Y.-C. Hu, R. Ecke, and G. Ahlers, Phys. Rev. Lett. **74**, 5040 (1995).

[23] K.M.S. Bajaj, J. Liu, B. Naberhuis, and G. Ahlers, to be published.

[24] G. Küppers and D. Lortz, J. Fluid Mech. **35**, 609 (1969).

[25] G. Küppers, Phys. Lett. **32A**, 7 (1970).

[26] R. M. Clever and F. H. Busse, J. Fluid Mech. **94**, 609 (1979).

[27] F. H. Busse and K. E. Heikes, Science **208**, 173 (1980).

[28] K. E. Heikes and F. H. Busse, Ann. N.Y. Acad. Sci. **357**, 28 (1980).

[29] Y. Hu, R. E. Ecke, and G. Ahlers, Phys. Rev. E **55**, 6928 (1997)

[30] Y.-C. Hu, W. Pesch, G. Ahlers. and R. Ecke, submitted to Phys. Rev. E.

[31] An exception is liquid helium. As the superfluid-transition temperature 2.176 K is approached from above, σ vanishes. However, experiments are difficult because σ varies from a value of order one to zero over a narrow temperature range of a few mK and because of the problem of flow visualization which has only recently been achieved under the required cryogenic conditions (P. Lucas, A. Woodcraft, R.

Matley, and W. Wong, International Workshop on Ultra-High Reynolds-Number Flows, Brookhaven National Laboratory, June 18 to 20, 1996).
[32] T. Clune and E. Knobloch, Phys. Rev. E **47**, 2536 (1993).
[33] Early theoretical evidence for the existence of a subcritical and tricritical bifurcation is contained in the work of Clever and Busse (CB)(Ref. [26]). More recent calculations of the tricritical line by Clune and Knobloch (Ref. [32]) are inconsistent with the result of CB. Using programs developed by W. Pesch, we re-calculated the tricritical line and obtained the result shown in Fig. 3 which is more detailed than, but agrees with that of CB.
[34] K. Buhler and H. Oertel, J. Fluid Mech. **114**, 261 (1982).
[35] J. J. Niemela and R. J. Donnelly, Phys. Rev. Lett. **57**, 2524 (1986).
[36] F. Zhong, R. Ecke, and V. Steinberg, Physica D **51**, 596 (1991).
[37] F. Zhong and R. Ecke, Chaos **2**, 163 (1992).
[38] Y. Tu and M. Cross, Phys. Rev. Lett. **69**, 2515 (1992).
[39] M. Fantz, R. Friedrich, M. Bestehorn, and H. Haken, Physica D **61**, 147 (1992).
[40] M. Neufeld, R. Friedrich, and H. Haken, Z. Phys. B. **92**, 243 (1993).
[41] M. Cross, D. Meiron, and Y. Tu, Chaos **4**, 607 (1994).
[42] Y. Ponty, T. Passot, and P. Sulem, Phys. Rev. Lett. **73**, 71 (1997); Phys. Rev. E **56**, 4162 (1997).
[43] Recently it was shown in Ref. [30] that the data for ξ and ω_a can be fit with a powerlaw and the expected theoretical leading exponents if large correction terms are allowed in the analysis.
[44] S. Chandrasekhar, *Hydrodynamic and Hydromagnetic Stability* (Oxford University Press, Oxford, 1961).
[45] M.E. Fisher, Phys. Rev. **176**, 257 (1968).

Final List of Participants

Sixteenth Symposium

on

Energy Engineering Sciences

May 13-15, 1998

Argonne National Laboratory
Argonne, Illinois

Henry D. I. Abarbanel
Physics Department
University of California-San Diego
9500 Gilman Drive
La Jolla, CA 92093-0402
Phone: 619/534-5590
Fax: 619/534-7664

Guenter Ahlers
Department of Physics
University of California-Santa Barbara
Santa Barbara, CA 93106
Phone: 805/893-3795
Fax: 805/893-4170

Stephen A. Altobelli
New Mexico Resonance
2425 Ridgecrest Drive SE
Albuquerque, NM 87108
Phone: 505/262-7155 ext. 5025
Fax: 505/262-7043

Sanjoy Banerjee
Department of Chemical Engineering
University of California-Santa Barbara
Santa Barbara, CA 93106
Phone: 805/893-3456
Fax: 805/893-7739

Paul I. Barton
Department of Chemical Engineering
Massachusetts Institute of Technology
Room 66-464
Cambridge, MA 02139
Phone: 617/253-6526
Fax: 617/258-5042

Brent D. Butler
Physical & Chemical Properties Division
National Institute of Standards & Technology
325 Broadway
Boulder, CO 80303
Phone: 303/497-3952
Fax: 303/497-5224

P. Scott Carney
Department of Physics & Astronomy
University of Rochester
Wilson Boulevard
Rochester, NY 14627
Phone: 716/275-8544
Fax:

Daniel Frederick
Department of Engineering Science & Mechanics
Virginia Polytechnic Institute
Norris Hall
Blacksburg, VA 24060
Phone: 540/552-2148
Fax:

Eiichi Fukushima
New Mexico Resonance
2425 Ridgecrest Drive SE
Albuquerque, NM 87108
Phone: 505/262-7575 ext. 5025
Fax: 505/262-7043

Gregory Gbur
Department of Physics & Astronomy
University of Rochester
Baush & Lomb Building
Wilson Boulevard
Rochester, NY 14623
Phone: 716/275-8544
Fax:

Robert Goulard
Division of Basic Energy Sciences, ER-15
U.S. Department of Energy
19901 Germantown Road
Germantown, MD 20874
Phone: 301/903-5822
Fax: 301/903-0271

Joachim V. R. Heberlein
Department of Mechanical Engineering
University of Minnesota
111 Church Street SE
Minneapolis, MN 55455
Phone: 612/625-4538
Fax: 612/624-1398

Costas P. Grigoropoulos
Department of Mechanical Engineering
University of California-Berkeley
MC 1740
Berkeley, CA 94720
Phone: 510/642-2525
Fax: 510/642-6163

James J. Hickman
Chemistry Department
George Washington University
725 21st Street NW
Washington, DC 20052
Phone: 703/207-9672
Fax: 202/994-5873

Ignacio E. Grossmann
Department of Chemical Engineering
Carnegie Mellon University
Pittsburgh, PA 15213
Phone: 412/268-2230
Fax: 412/268-7139

Robert H. Kraichnan
Robert H. Kraichnan, Inc.
369 Montezuma, 108
Santa Fe, NM 87501
Phone: 505/986-3979
Fax: 505/989-4737

Howard J. M. Hanley
Physical & Chemical Properties Division
National Institute of Standards & Technology
325 Broadway
Boulder, CO 80303
Phone: 303/497-3320
Fax: 303/497-5044

Konstantin K. Likharev
Department of Physics & Astronomy
State University of New York-Stony Brook
Stony Brook, NY 11794-3800
Phone: 516/632-8159
Fax: 516/632-8774

Thomas J. Hanratty
Department of Chemical Engineering
University of Illinois-Urbana
600 South Mathews Avenue
Urbana, IL 61801
Phone: 217/333-1318
Fax: 217/333-5052

Joseph J. McCarthy
Department of Chemical Engineering
Northwestern University/University of Pittsburgh
2145 Sheridan Road
Evanston, IL 60208
Phone: 847/491-3555
Fax: 847/491-3728

John B. McLaughlin
Department of Chemical Engineering
Clarkson University
8 Clarkson Avenue
Potsdam, NY 13699-5705
Phone: 315/268-6663
Fax: 315/268-6654

Thomas G. Owano
Department of Mechanical Engineering
Stanford University
Duena Street, Bldg. 520
Stanford, CA 93405-3032
Phone: 650/723-1295
Fax: 650/723-1748

Curtis R. Menyuk
Dept. of Computer Science & Electrical Engineering
University of Maryland-Baltimore County
TRC 201A
Baltimore, MD 21250
Phone: 410/455-3501
Fax: 410/455-6500

Robert E. Price
Division of Engineering and Geosciences, ER-15
U.S. Department of Energy
Office of Basic Energy Sciences
19901 Germantown Road
Germantown, MD 20874
Phone: 301/903-3565
Fax: 301/903-0271

Issam Mudawar
School of Mechanical Engineering
Purdue University
1288 Mechanical Engineering
West Lafayette, IN 47907
Phone: 765/494-5705
Fax: 765/494-0539

Mikhail I. Rabinovich
Institute for Nonlinear Science
University of California-San Diego
9500 Gilman Drive
La Jolla, CA 92093-0402
Phone: 619/534-6753
Fax: 619/534-7664

Evgeny A. Novikov
Institute for Nonlinear Science
University of California-San Diego
La Jolla, CA 92093-0402
Phone: 619/822-2010
Fax: 619/534-7664

Willis H. Ray
Department of Chemical Engineering
University of Wisconsin
1415 Engineering Drive
Madison, WI 53706
Phone: 608/263-4732
Fax: 608/262-0832

Julio M. Ottino
Chemical Engineering Department
Northwestern University
2145 Sheridan Road
Evanston, IL 60208-3120
Phone: 847/491-3558
Fax: 847/491-3728

Linda E. Reichl
Physics Department
The University of Texas
Austin, TX 78712
Phone: 512/471-7253
Fax: 512/471-9621

John Ross
Department of Chemistry
Stanford University
Stanford, CA 94305
Phone: 650/723-9203
Fax: 650/723-4817

Charles R. Tolle
Department of Applied Materials & Technology
Idaho National Engineering & Environmental Laborat
P.O. Box 1625
Idaho Falls, ID 83415-2210
Phone: 208/526-1895
Fax: 208/526-0670

Nikolai F. Rulkov
Institute for Nonlinear Science
University of California-San Diego
9500 Gilman Drive
La Jolla, CA 92093
Phone: 619/534-6876
Fax: 619/534-7664

Sal Torquato
Dept. of Civil Engineering & Princeton Materials Instit
Princeton University
Princeton, NJ 08544
Phone: 609/258-3341
Fax: 609/258-2685

Gary S. Settles
Department of Mechanical Engineering
Pennsylvania State University
301D Reber Building
University Park, PA 16802
Phone: 814/863-1504
Fax: 814/865-0118

Lev S. Tsimring
Instutute for Nonlinear Science
University of California-San Diego
9500 Gilman Drive
La Jolla, CA 92093-0402
Phone: 619/534-0816
Fax: 619/534-7664

Daphne Stoner
Department of Biotechnologies
Idaho National Engineering & Environmental Laboratory
P.O. Box 1625
Idaho Falls, ID 83415-2203
Phone:
Fax:

Jorge Vinals
Supercomputer Computations Research Institute
Florida State University
400 Dirac Science Library
Tallahassee, FL 32306-4130
Phone: 850/644-1010
Fax: 850/644-0098

Stephen L. Teitel
Department of Physics & Astronomy
University of Rochester
600 Wilson Boulevard
Rochester, NY 14627
Phone: 716/275-4039
Fax: 716/275-8527

Graham B. Wallis
Thayer School of Engineering
Dartmouth College
8000 Cummings Hall
Hanover, NH 03755
Phone: 603/646-2789
Fax: 603/646-3856

Emil Wolf
Department of Physics & Astronomy
University of Rochester
Wilson Boulevard
Rochester, NY 14627
Phone: 716/275-4397
Fax: 716/473-0687